Title

Molecular-level Understanding of Electrode-Electrolyte Interface in Hydrogen Evolution Reaction

Author

Shah, Aamir Hassan

Publication Date

2024

Peer reviewed|Thesis/dissertation

UNIVERSITY OF CALIFORNIA

Los Angeles

Molecular-level Understanding of Electrode-Electrolyte Interface in Hydrogen Evolution Reaction

A dissertation submitted in partial satisfaction

of the requirements for the degree

Doctor of Philosophy in Chemistry

by

Aamir Hassan Shah

2024

ABSTRACT OF THE DISSERTATION

Molecular-level Understanding of Electrode-Electrolyte Interface in Hydrogen Evolution Reaction

by

Aamir Hassan Shah

Doctor of Philosophy in Chemistry

University of California, Los Angeles, 2024

Professor Xiangfeng Duan, Chair

The hydrogen evolution reaction (HER) is one of the most fundamental and critical reactions in renewable energy conversion. The recent advancement in various platinum (Pt) nanocatalyst designs has led to greatly improved HER activity. It is well recognized that the HER kinetics is drastically slower in alkaline media compared to acidic media, but the descriptors of the HER kinetics are still elusive. Specifically, in the presence of alkali metal cations and hydroxyl anions, the electrode–electrolyte (platinum–water) interface in an alkaline electrolyte is far more complex than that in an acidic electrolyte. The effects of different alkali metal cations (AM^+) and pH on these reactions are poorly understood due to a lack of suitable experimental methods. We are combining surface-sensitive electrical transport spectroscopy (ETS) with other electrochemistry techniques and computational studies to probe and understand the fundamental role of different AM^+ and pH on the reaction kinetics of HER. Our study provides fundamental insights into how and why AM^+ and pH influence the HER in alkaline media. We expect that this research will provide the molecular-level understanding that will shed new insights into electrolyte engineering as an alternative pathway to control electrochemical reaction kinetics.

The dissertation of Aamir Hassan Shah is approved.

Yu Huang

Chong Liu

Philippe Sautet

Xiangfeng Duan, Committee Chair

University of California, Los Angeles

2024

To my family and friends

Table of Contents

List of Figures

ACKNOWLEDGMENTS

I am grateful for the invaluable support and guidance I have received from the friends and research mentors within Professor Xiangfeng Duan and Yu Huang's research groups, especially Professor Duan, whose encouragement to explore diverse research avenues has been instrumental in shaping my academic journey. I am also thankful for the enriching collaborations, notably with Zisheng Zhang and Patricia Poths from Professor Anastassia's research group. Working alongside such thoughtful, kind, and humble individuals across various research domains has been a privilege, and I will forever cherish the experiences and knowledge gained during my time at UCLA.

I extend my heartfelt gratitude to Dr. Lin Lin and Professor Paul Weiss, whose influence played a pivotal role in my decision to join UCLA. Their unwavering support has been a cornerstone of my academic pursuits. Despite the geographical distance, the unwavering support from my family and friends has been a constant source of strength; a simple phone call has always been a reminder that I am not alone on this journey.

To all those who have touched my life in profound ways, I express my deepest appreciation. Your belief in me and your unwavering encouragement have fueled my aspirations. I am forever indebted to each one of you.

Chapter 1 is adapted with permission from:

A. H. Shah, C. Wan, Y. Huang*, and X. Duan*, Toward Molecular Level Understandings of Hydrogen Evolution Reaction on Platinum Surface, J. Phys. Chem. C. 2023, 127, 12841–12848 © 2023 American Chemical Society.

Chapter 2 is adapted with permission from:

A. H. Shah, Z. Zhang, Z. Huang, S. Wang, G. Zhong, C. Wan, A. N. Alexandrova*, Y. Huang* and X. Duan*, The Role of Alkali Metal Cations and Platinum-Surface Hydroxyl in the Alkaline

Hydrogen Evolution Reaction, Nat. Catal. 2022, 5, 923–933 © 2022 The Author(s), under exclusive license to Springer Nature Limited.

Chapter 4 is adapted with permission from:

A. H. Shah[#], Z. Zhang[#], C. Wan, S. Wang, A. Zhang, L. Wang, A. N. Alexandrova*, Y. Huang*, and X. Duan*, Platinum Surface Water Orientation Dictates Hydrogen Evolution Reaction Kinetics in Alkaline Media, J. Am. Chem. Soc. 2024, 146, 9623–9630 © 2024 American Chemical Society.

VITA

2019-2021 M.S. in Chemistry, University of California, Los Angeles

2012-2014 M.Phil in Physical Chemistry, Quaid-i-Azam University, Islamabad, Pakistan

2010-2012 M.Sc in Physical Chemistry, Quaid-i-Azam University, Islamabad, Pakistan

PUBLICATIONS

1. A. H. Shah, P. Poths, C. Wan, S. Wang, Y. Liu, J. Zhou, Y. Ling, A. N. Alexandrova*, Y. Huang*, and X. Duan*, In Revision, J. Am. Chem. Soc., (2024).

2. Z. Huang[#], T. Cheng[#], A. H. Shah[#], G. Zhong, C. Wan, P. Wang, M. Ding, J. Huang, Z. Wan, S. Wang, J. Cai, B. Peng, H. Liu, Y. Huang*, W. A. Goddard III* and X. Duan*, Nat. Catal., Accepted (2024).

3. A. H. Shah[#], Z. Zhang[#], C. Wan, S. Wang, A. Zhang, L. Wang, A. N. Alexandrova*, Y. Huang*, and X. Duan*, J. Am. Chem. Soc., 146, 9623–9630 (2024).

4. C. Wan, Z. Zhang, J. Dong, M. Xu, H. Pu, D. Baumann, Z. Lin, S. Wang, J. Huang, A. H. Shah, X. Pan, T. Hu, A. N. Alexandrova*, Y. Huang* and X. Duan*, Nat. Mater., 22, 1022-1029 (2023).

5. A. H. Shah, C. Wan, Y. Huang*, and X. Duan*, J. Phys. Chem. C., 127, 12841–12848 (2023).

6. Y. Liu, E. Zhu, J. Huang, A. Zhang, A. H. Shah, Q. Jia, M. Xu, E. Liu, Q. Sun, X. Duan, and Yu Huang*, Nano Lett., 23, 2758-2763 (2023).

7. A. H. Shah, Z. Zhang, Z. Huang, S. Wang, G. Zhong, C. Wan, A. N. Alexandrova*, Y. Huang* and X. Duan*, Nat. Catal., 5, 923–933 (2022).

8. G. Zhong[#], T. Cheng[#], A. H. Shah, C. Wan, Z. Huang, S. Wang, T. Leng, Y. Huang*, W. A. Goddard III*, and X. Duan*, Proc. Natl. Acad. Sci. USA., 119, e2208187119 (2022).

CHAPTER 1

Introduction

The electrocatalytic hydrogen evolution reaction (HER) is essential for water electrolysis that can directly convert renewable electricity (from solar cells or wind mills) into chemical energy in the form of molecular hydrogen. The electrochemical water-splitting reaction is comprised of two half-reactions: the cathodic hydrogen evolution reaction (HER) and anodic oxygen evolution reaction (OER). The acidic electrolysis features facile cathodic HER kinetics, although the anodic OER typically requires costly precious metal catalysts. On the other hand, the OER in the alkaline condition can be readily facilitated with non-precious metal oxide/hydroxide catalysts, while the HER kinetics in the alkaline condition are considerably slower. Platinum (Pt) represents the state-of-the-art electrocatalyst for the HER and hence intensive efforts have been invested in understanding the fundamental reaction mechanism and kinetics on Pt-based electrocatalytic systems for HER[1-2]. In general, the HER could involve three elementary steps depending on electrolyte pH and display intriguing pH-dependent kinetics. The first step is one electron reduction of proton from solution on Pt electrode to form Pt—H_{ad} (Volmer step, Equation 1-1 and 1-2):

$$H_3O^+ + e^- + Pt \leftrightarrow Pt—H_{ad} + H_2O \qquad \text{(acidic)} \qquad (1\text{-}1)$$

$$H_2O + e^- + Pt \leftrightarrow Pt—H_{ad} + OH^- \qquad \text{(alkaline)} \qquad (1\text{-}2)$$

In the second step, molecular hydrogen (H_2) can form either via recombination of two adsorbed hydrogens (Pt—H_{ad}) (Tafel step, Equation 1-3):

$$2\ Pt—H_{ad} \leftrightarrow H_2 + 2\ Pt \qquad (1\text{-}3)$$

or by a simultaneous proton reduction on electrode surface and its reaction with the surface bound H (Pt—H_{ad}) to form molecular hydrogen (Heyrovsky step, Equation 1-4 and 1-5):

$$Pt—H_{ad} + H_3O^+ + e^- \leftrightarrow H_2 + Pt + H_2O \qquad \text{(acidic)} \qquad (1\text{-}4)$$

$$Pt—H_{ad} + H_2O + e^- \leftrightarrow H_2 + Pt + OH^- \qquad \text{(alkaline)} \qquad (1\text{-}5)$$

It is commonly perceived that H_3O^+ is the primary proton donor for the Volmer or Heyrovsky step in acidic electrolytes, while H_2O molecules are proton sources in alkaline electrolytes, which is much more difficult to dissociate, thus leading to far more sluggish HER kinetics in alkaline electrolytes[3]. It is also generally recognized that the Tafel step is rate determining step in acidic media due to the facile Volmer step[4-9], whereas in neutral and alkaline media, the Volmer step (water dissociation) is often considered the rate determining step, but not without debate[10].

Beyond the elementary Volmer, Tafel and Heyrovsky steps, other important factors including the specific Pt surface sites and local chemical environment could also substantially modify the reaction kinetics. For example, Koper *et al.* argued that the rate determining step in alkaline media depends on the exact alkali metal cations and suggested the Heyrovsky step as the rate determining step in 0.1 M LiOH, while the Volmer step being the rate determining step in 0.1 M KOH (ref.[10]). Nonetheless, our recent experimental results suggest that although the cations could modify the HER activity, the reaction mechanism or rate determining step is independent of the nature of cations[11], and only depends on the local pH near Pt surface[12].

In general, the electrode-electrolyte (Pt-H_2O) interface in alkaline media is far more complex because of near surface presence of positively charged alkali metal cations and possible involvement of hydroxyls[8, 13-16], which could fundamentally modify local chemical environment (e.g., local pH, water orientation, surface water protonation status, binding of reaction

intermediates) and the HER kinetics. Furthermore, if additional buffers were included to tailor the bulk solution pH, the competitive adsorption or enrichment of buffer molecules near electrochemical interface could further complicate situation and lead to apparently inconsistent results among studies using different buffer molecules and ambiguous or sometimes conflicting conclusions. Overall, the exact evolution/switching of HER kinetics with the electrolyte pH and the underlying molecular mechanism remain a topic of considerable debate, with different schools of thought being under active consideration.

1.1. The current understanding and misunderstanding

It is well recognized that the binding energy of the reaction intermediates in a catalytic process determines how well a catalyst works. In general, following Sabatier principle, the optimal catalyst should bind with intermediate strongly enough so that the reagents would likely bind and react, but weakly enough so that the product could readily desorb and leave. It has been found that the HER rate on different metal surface is closely correlated with the work function or hydrogen binding energy (HBE) of the respective metal[17-20]. In particular, by correlating HER exchange current density in acidic media with computationally determined hydrogen chemisorption energies of different metals, Nørskov *et al.* have generated a volcano plot and found that Pt exhibits the highest HER activity for its nearly optimal HBE that ensures both efficient adsorption and desorption of H_{ad} in acidic electrolytes (Fig. 1.1 a,b)[2]. Similarly, Yan *et al.* also revealed a volcano-type relationship between the HER exchange current density and the HBE in alkaline electrolytes (Fig. 1.1 c)[21].

Although the HBE represents a good physical descriptor for HER, experimental determination of the HBE of different metal electrodes is nontrivial, particularly in presence of the complex electrolytes with multiple possible surface adsorbates. In this regard, Zeradjanin and

coworkers have suggested that change of the work function (ΔΦ) upon adsorption of hydrogen through a water layer (measured in humid hydrogen) as an experimental interfacial descriptor to interpret the electrocatalytic activity of HER on different metals. They found that HER activities exhibits a similar volcano relationship with the derived ΔΦ of different metals[22], highlighting the effectiveness of ΔΦ in approximating the trend of computationally derived HBE (Fig. 1.1 d).

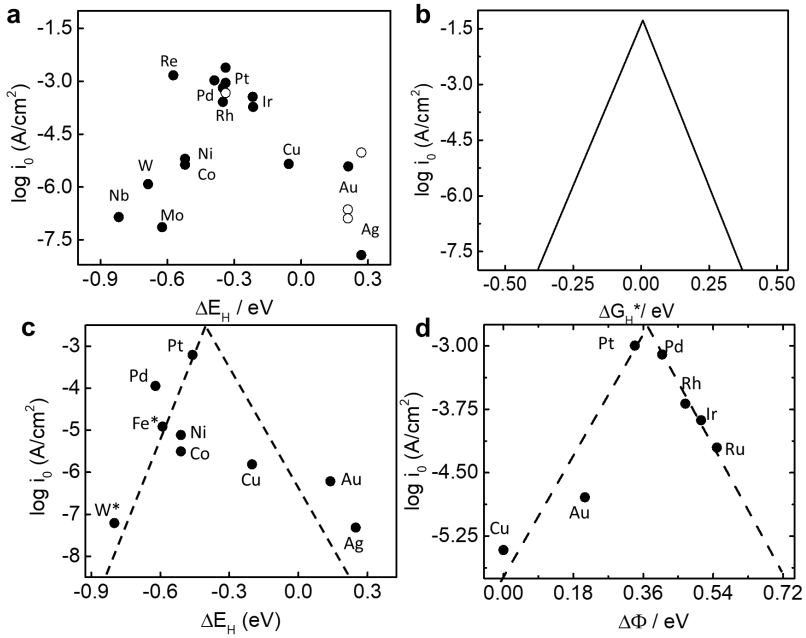

Figure 1.1: Correlation between exchange current densities and hydrogen binding energies (HBE) of different metals. (a) Experimentally measured exchange current (log (i_0) for HER over different metal surfaces as a function of calculated hydrogen chemisorption energy per atom in acidic media. The open and filled symbols are for single crystal and polycrystalline samples, respectively and (b) Calculated HER exchange current (log (i_0) obtained from the simple kinetic model plotted as a function of the free energy for hydrogen adsorption $\Delta G_{H^*} = \Delta E_H + 0.24$ eV (data replotted with permission from ref.[2] Copyright 2005 IOP Publishing, Ltd). (c) Exchange current densities, log(i_0), on monometallic surfaces as a function of the calculated HBE in alkaline media (Reprinted from ref.[21] with permission from the Royal Society of Chemistry). (d) Experimental "volcano"-plot where the HER exchange current in acidic medium is correlated to the experimentally determined change in the work function of the metal upon adsorption of hydrogen through the water layer (Reprinted from ref.[22] with permission from the Royal Society of Chemistry.).

Although the ΔΦ measured in humid hydrogen effectively captures the interplay between metal–hydrogen (M–H) and metal–water (M–H_2O) interaction and its critical role in HER process, it cannot capture the more complex electrode-electrolyte interactions in realistic electrolytes

containing many other cationic or anionic species. Additionally, it has also been suggested that HBE is an intrinsic property of the metal independent of the exact electrolytes. For example, Jerkiewicz *et al.* have experimentally shown that the bond energy between Pt and underpotential-deposited hydrogen (H_{upd}) at the electrified solid/liquid interface is close to the bond energy between Pt and chemisorbed hydrogen (H_{chem}) under gas-phase conditions, indicating a similar binding mechanism regardless of the external environment[23]. Likewise, Norskov *et al.* have computationally investigated the effect of molecular water on the hydrogen adsorption and found that adding a water overlayer changes the adsorption energy of hydrogen on Pt(111) by less than 0.02 eV^2, indicating that the water molecules on Pt(111) surface shows no significant effect on HBE.

To interpret the pH-dependent HER kinetics, Yan *et al.* suggested the concept of apparent HBE (HBE_{app}) in realistic electrolytes[24]. In this case, the HBE_{app} is represented by underpotential-deposited hydrogen (H_{upd}) peak potential value in cyclic voltammetry (CV) (Fig. 1.2a), which evaluates the competitive *H binding and water adsorption (Fig. 1.2 b)[24] . With this approach, they found a systematic increase of HBE_{app} with increasing electrolyte pH, which was used to explain the decreased HER activity in alkaline electrolytes in their studies[25]. Quantum mechanics molecular dynamics (QMMD) of the Pt(100)/H_2O interface revealed that the Pt surface in high pH (12.8) electrolyte is more negatively charged than that in low pH electrolyte, and thus the water on the Pt surface prefer a hydrogen down ($OH_2\downarrow$) instead of oxygen down ($H_2O\downarrow$) configuration, resulting in less hydrogen bond with the H_{ad} that could weaken the Pt-H bond strength and thus leading to higher HBE_{app} at higher pH[26].

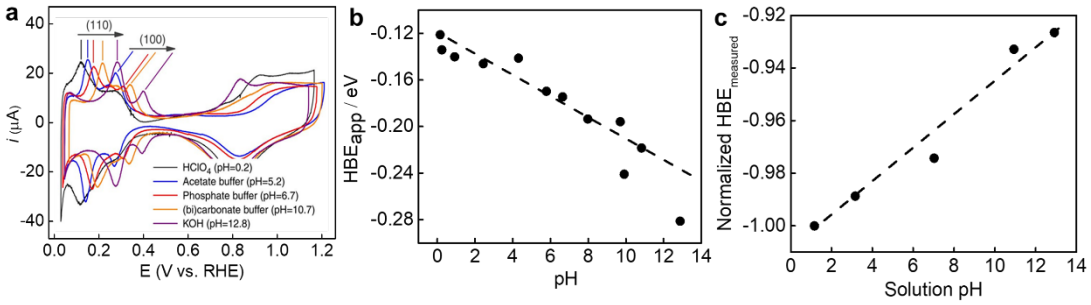

Figure 1.2: Correlation of HBE_{app} determined from the H_{upd} peak potential in CV with solution pH. (a) iR corrected CVs of Pt collected in selected Ar-saturated electrolytes at a sweep rate of 50 mV s^{-1} (Reprinted with permission from ref.[25] Copyright 2015 Springer Nature); (b) HBE_{app} on Pt(110) facet of polycrystalline Pt obtained from H_{upd} peak potential in CVs as a function of solution pH (data replotted with permission from ref.[25] Copyright 2015 Springer Nature) ; (c) pH dependent overpotential deposited hydrogen binding energy ($HBE_{measured}$) determined from surface-enhanced infrared absorption spectroscopy (Reprinted with permission from ref.[27] Copyright © 2020, American Chemical Society).

Although the current HBE or HBE_{app} theory has been successful in interpreting various experimental HER results, there is no lack of debates whether the HBE_{app} determined from H_{upd} peak position is accurate or sufficient descriptor for elucidating HER. In particular, a number of studies have reported a higher HER activity with increasing pH in the pH range from 11-13 (ref.[28,29]), which cannot be satisfactorily explained by the HBE_{app} theory discussed above. Koper *et al.* further suggested that the HBE descriptor can't explain the pH dependent catalytic behavior on Pt(111) that shows little H_{upd} peak potential shift with pH but a clear pH dependent HER kinetics[16]. Additionally, Koper *et al.* attributed the H_{upd} peak to the replacement of OH_{ad} by H_{ad} and suggested that the shift in H_{upd} peak potential with increasing pH is due to a decrease in OH_{ad} stability with increasing local cation concentration near catalytic surface[30-31].

It should be noted the HBE is dynamically dependent both on the intrinsic binding energy measured at low coverage and the lateral interaction between H_{ad} and other surface species, including H_{ad}, OH_{ad}, H_2O, or metal cations[32]. Therefore, the surface coverage of these different species could fundamentally alter the HBE_{app} via lateral attraction or repulsion. For example, the Pt (111) features a rather broad H_{upd} peak while the Pt(100) and Pt(110) show sharp H_{upd} peaks

with well-defined peak positions. The broader H_{upd} peak on Pt (111) may be ascribed to the stronger lateral repulsion effect between the H_{ad} on the Pt (111).[32] Analysis of the H_{upd} polarization curve on Pt(111) shows lateral repulsion energy is linear with the surface coverage, consistent with the Frumkin isotherm assumption[33]. Simulation of hydrogen adsorption energy Pt(111) surface at 1/9, 2/9, 4/9, and 9/9 monolayer coverage also shows a consistent trend with experimental observations[34]. Similarly, Pt (100) or (110) also exhibit coverage-dependent HBE, but with much smaller repulsion between the H_{ad} due to the lower surface density[33]. According to Markovic's calculation, the Pt(111) has only achieved 66% coverage even at 0.05 V vs. reversible hydrogen electrode (RHE), still far from the full coverage condition[13, 35]. Therefore, the HBE_{app} evaluated by the H_{upd} peak position at a potential (i.e. 0.05 – 0.4 V vs. RHE) with a relatively low H_{ad} coverage could differ substantially from the HBE in the HER region where there is a nearly full coverage of H_{ad}, and thus may not be a reliable descriptor for HER.

Indeed, it has been suggested that there are two types of hydrogen, the strongly adsorbed H_{upd} at the 4-fold hollow sites on Pt (100) and the 3-fold hollow sites on Pt (111), and the relatively weak overpotential deposition hydrogen (H_{opd}) at the atop sites of Pt atoms[36-37]. The H_{upd} usually starts at 0.4 V vs. RHE, while the H_{opd} typically starts below 0.1 V vs. RHE. Conway *et al.* pointed out that the H_{upd} binds too strongly on the Pt surface to be the intermediate for HER[37], while the weakly adsorbed H_{opd} matches the near zero adsorption free energy, making Pt the best catalyst material for HER (located near the peak of the Volcano plot)[37-38]. Indeed, theoretical studies by the Peterson group indicated that H_{upd} is almost inert compared to H_{opd}[39]. *In situ* Raman studies have revealed that a new Pt-H band at 2092 cm^{-1} emerges at H_{opd} potential regime (but not present in H_{upd} regime), indicating the nature of the surface hydrogen are remarkably different in the H_{upd} and H_{opd} regions[40]. By using surface-enhanced infrared absorption spectroscopy, Shao *et al.* probed and suggested the HBE for H_{opd} weakens with increasing pH from 1.1 to 12.9, opposite to the

increasing trend determined from H_{upd} (Fig. 1.2 c)[27]. The surface-enhanced infrared spectroscopy also suggested that the H_{opd} is the primary intermediates involved in the Tafel step for HER[41]. We note that there is also the opposite opinion that H_{opd} is unlikely to contribute to the HER mechanism due to its positive adsorption energies[42]. Although there is increasing indications that the H_{upd} is unlikely the key reaction intermediates and the H_{opd} is more likely the active intermediates for HER, particularly considering that the H_{upd} occurs at a very different potential regime from HER potential window, there is still no consensus regarding the exact role of the H_{upd} and the H_{opd} in HER due to the lack of direct experimental evidence. Additional studies are necessary to fully resolve this matter.

Alternatively, it has also been suggested that the interfacial water structure could greatly affect the HER kinetics. Rossmeisl *et al.* suggested that the pH-dependent change of interfacial water dipole and water structure may fundamentally affect interfacial proton transfer and lead to more sluggish HER kinetics in alkaline media[15]. Likewise, Jia *et al.* also highlighted the roles of interfacial water in shuffling the HER intermediates through the interface and their role in HER kinetics[43]. In a more systematic study, Koper et al. found that there is a pH-dependent evolution of potential of zero free charge (pzfc) on Pt (111) surface, and suggested that the pzfc at different pH could greatly affect the water structure in the electrical double layer, which in turn modulates proton and OH^- transport and thus the HER kinetics[16]. Specifically, the pzfc is closer to the HER/HOR region in acidic media (~ 0.34 V vs. RHE)[16], featuring a relatively weak electrical field and small interfacial water reorganization energy to move a proton through electrical double layer, which is favorable for HER process. While in alkaline media, the pzfc is far from the HER region (~ 1 V vs. RHE), and thus there is a strong electric field that leads to a larger interfacial water reorganization energy for the OH^- to transfers through the double layer[16]. Nonetheless**,** although the interfacial water is expected to play a significant role in HER kinetics, the pzfc theory can

neither explain the higher HER activity in more basic pH (i.e., from pH 11-13) compared to neutral media (pH 7-10) as observed in a number of studies[28,29] and our own systematic investigations.

1.2. Towards molecular level interpretation

Despite the apparent consistencies in certain studies, neither the HBE (particularly that determined from H_{upd}) nor the pzfc theory can offer a fully satisfactory interpretation of the pH-dependent HER kinetics. In fact, it is inappropriate to use a sole macroscopic descriptor (e.g., HBE or pzfc) to provide a unified picture regarding the HER kinetics across the entire pH 0-14 range, as the HER in these vastly different conditions could undergo entirely different molecular pathways with different rate determining steps. Moreover, the local chemical environment, source of H_{ad}, involvement of different cations and adsorbed hydroxyl (OH_{ad}) are drastically different in different pH media, some of which may fundamentally modify the reaction pathways and kinetics. Thus, it is necessary to develop a molecular picture of the charge/atom transfer and molecular transformation pathway to properly and fully understand the pH-dependent HER kinetics.

Markovic *et al.* and Chan *et al.* attributed the more sluggish HER activity in alkaline media than that in acid to a change of proton source from H_3O^+ in acid to H_2O in alkaline and the higher energy barrier for H_2O dissociation[9, 44], although the exact switching point has been ambiguous. Our recent experimental and theoretical studies in acidic and neutral electrolytes revealed that the switch of proton source occurred at around pH 4 instead of the acid/base boundary, which is attributed to a change of Pt surface H_2O protonation status and associated with the Pt-surface hydronium pKa (4.3)[12]. When the pH is below the pKa (~4), the Pt-surface water are mostly protonated, H_3O^+ is the proton source and the Pt-H_{ad} formation (Volmer step) is rather facile, thus the H_{ad} recombination to form molecular H_2 (Tafel step) is the rate-determining step, resulting in a Tafel slope of 30 mV/dec. When the pH is above the pKa, the Pt-surface water is mostly

deprotonated, H_2O represents the primary proton source. In this case, the water dissociation barrier surpasses the H_{ad} recombination barrier to make the Volmer step the rate-determining step, as evidenced by a clear switch of the Tafel slope from 30 mV/dec to 120 mV/dec[13, 45].

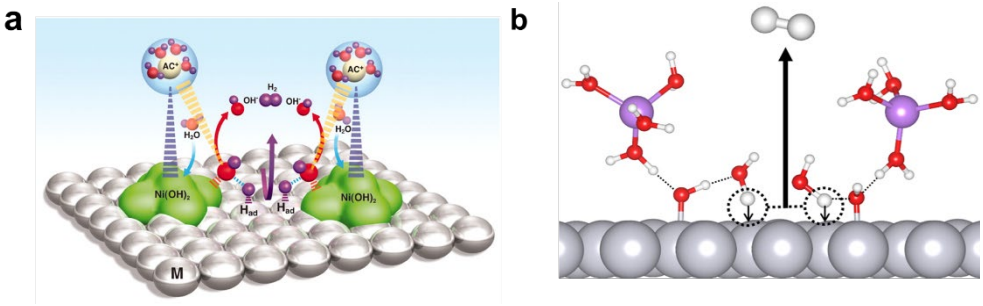

Figure 1.3: Schematic representation of water dissociation facilitated by oxophilic metals and or Pt-OH_{ad} in alkaline electrolytes. (a) Transition metal hydroxide [e.g., $Ni(OH)_2$] on Pt surface promotes water dissociation and Pt-H_{ad} formation, followed by subsequent recombination of two H_{ad} atoms to form H_2 (magenta arrow) and OH^- desorption from the domains (red arrows) and adsorption of another water molecule on the same site (blue arrows) (Reprinted with permission from ref. [44] Copyright © 2011, The American Association for the Advancement of Science) (b) Schematics showing the Pt-surface OH_{ad} may function as electronically favored proton-acceptors and geometrically favored proton-donors to interfacial water molecules, which facilities water dissociation and promotes alkaline Volmer step (Reprinted with permission from ref.[11] Copyright © 2022, The Author(s), under exclusive license to Springer Nature Limited).

Moreover, it is noted that, beyond pH or the exact proton source for H_{ad}, there are other factors that affect the HER activity. For example, Markovic *et al.* had previously found that the HER kinetics in alkaline media can be improved by presence of oxophilic groups that could facilitate H_2O dissociation (Fig. 1.3a)[44]. Later, the same group reported a monotonic relationship between HER activity and oxophilic group's affinity to OH_{ad} with $Ni(OH)_2$/Pt(111) being the most active and $Mn(OH)_2$/Pt(111) being the least active[8], and proposed a bifunctional mechanism—where the edges of $M(OH)_2$ clusters function as the water dissociation catalyst to promote the H_2O dissociation and the nearby Pt sites function as the optimum binding sites for H_{ad} that recombine and form molecular hydrogen (Fig. 1.3a). They further suggested that there should be an optimal balance between facilitating water dissociation and preventing 'poisoning' by OH_{ad} (water dissociation product)[8]. Jia and coworkers experimentally verified the bifunctional mechanism and

robustly demonstrated that the presence of hydroxyl groups on surface Ru sites in the HER potential region plays a key role in promoting the rate-determining Volmer step[43, 46]. Likewise, Koper *et al.* also show that the rate of alkaline HER exhibits a volcano-type relationship with the hydroxide binding strength[47]. The conclusion was further supported by Tian's work using *in-situ* Raman to probe the Ru-OH on PtRu and Ni-OH on PtNi surface in the HER potential window[48-49].

Although substantial studies are supporting the bifunctional mechanism[46, 50-52], there are no lack of alternative interpretations[43, 53-56]. For example, Schwämmlein *et al.* suggested that the participation of oxophilic active sites in a bifunctional mechanism is of minor importance with respect to the HER activity compared to its influence on the electronic structure of Pt[53], and similarly Zhuang *et al.* argued that the oxophilic metals promote HER kinetics by electronically weakening the Pt—H_{ad} binding energy[56]. Moreover, bifunctional mechanism only explains the HER activity change by introducing another oxophilic metal, and is viable only in alkaline media. Together, although it is recognized the oxophilic metals on Pt surface could substantially modify HER kinetics, there is no general consensus on the exact role of the oxophilic metals, facilitating the water dissociation, altering the HBE of the Pt or both?

Beside the pH, the exact electrolyte cations could also play a role in modifying the HER activity. For example, it has been shown that the HER activity at pH 13 follows the trend of LiOH>NaOH> KOH>RbOH>CsOH[57,58]. Different interpretation have been suggested to interpret such activity trend. Bandarenka and colleagues suggested that the interaction between the alkali metal cations with the reaction intermediates on the electrode surface could alter the HER activity[57]; Koper and co-workers recently suggested that different AM^+-Pt interactions lead to a change in the rate-determining step from the Heyrovsky step in Li^+-containing electrolytes to the Volmer step in K^+-containing electrolytes with suppressed HER activity[10]; Huang *et al*. suggested

that the larger cations (e.g., $Cs^{+)}$ accumulate at electrode surface, increase the static dielectric constants at the interface[58], which in turn causes a greater reorganization energy and a higher entropic barrier for water dissociation[58]; Resasco *et al.* also proposed that the larger cations (e.g., Cs^{+}) accumulate on near the electrode surface could block the transport of interfacial hydroxide ions (product of water dissociation) to the bulk, which adversely impacts the HER activity[59].

A number of mechanistic understandings have been suggested to interpret the pH-dependent or electrolyte-dependent HER kinetics. The progresses to date are largely guided by over simplified approaches with a single macroscopic descriptor. On the other hand, the exact nature of electrode-electrolyte environment and molecular reaction pathway in different electrolyte could be substantially different, depending on the surface water protonation status, water orientation, as well as other unavoidable cations, anions, buffer molecules that may fundamentally alter the local chemical environment near the electrode-electrolyte interface. In particular, the HER in acid, neutral and alkaline media follows different reaction pathways with different rate determining steps (Fig. 1.4). Thus, a single descriptor can hardly give a fully satisfactory interpretation the evolution of the HER kinetics in different pH environment. For example, in acidic electrolyte (pH 1-4), the source of H_{ad} is H_3O^+ with the Tafel step being rate determining step and hence HBE as a key descriptor. Whereas, above surface hydronium pKa ($4 < pH < 10$), the water molecules are proton source and hence the water dissociation (i.e., Volmer step) becomes the rate determining step. Therefore, introducing oxophilic metal atoms can help in facilitating water dissociation and thus enhance the HER activity[8, 44, 50]. In the alkaline media ($pH > 10$), the Heyrovsky step becomes the rate determining step and hence the HER activity increases at higher pH since a higher OH^- concentration may lead to higher OH_{ad} on Pt surface, which act as proton donors and acceptors to near surface water and promote water dissociation[11]. Furthermore, it is also suggested that even within the alkaline media, the HER can have multiple descriptors[47, 60-61].

Thus, the attempt to use a single macroscopic descriptor to explain the electrocatalytic reaction in these very different situations can be misleading.

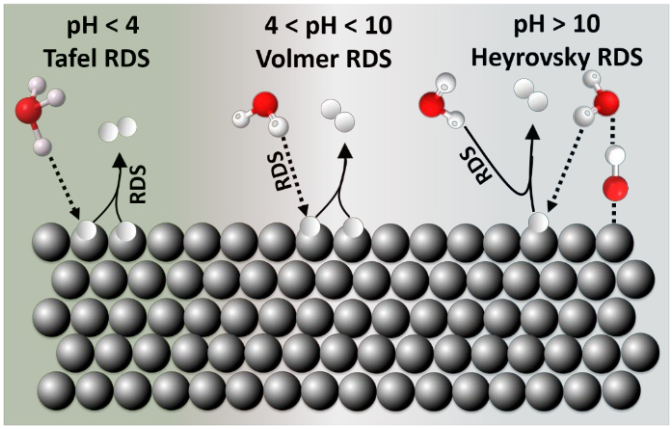

Figure 1.4: Schematic illustration of various rate determining steps (RDS) of HER in different pH regions. Tafel step as RDS in acidic media (pH < 4), Volmer step as RDS in neutral and near neutral regions (4 < pH < 10) and Heyrovsky step as RDS in alkaline media.

In **Chapter 2**, we have shown that the AM^+ play an indirect role in modifying HER kinetics: with the smaller cations (e.g., Li^+) favor a higher hydroxyl (OH_{ad}) coverage on electrode surface in the HER potential window that acts as both electronically favored proton-acceptors and geometrically favored proton-donors to promote water dissociation in alkaline media, thus boosting the HER activity (Fig. 1.3b)[11]. In **Chapter 3**, we combined on-surface electrical transport spectroscopy (ETS) and near-surface electrochemical impedance spectroscopy (EIS) with ab initio molecular dynamics simulations (AIMD) to probe and understand the fundamental role of weakly hydrated alkali metal cations (Rb^+ and Cs^+ vs. K^+ as a reference) in HER kinetics. Besides, the role of electrolyte cations, we note that the explanation of the different HER activity on Pt surface in acid, neutral and alkaline media is still a topic of considerable debate. To resolve the apparent inconsistencies among different interpretations, it was essential to develop a molecular level picture of the exact reaction pathways so that we can properly evaluate the relevance and importance of different descriptors and understand the fundamental origin of different HER kinetics in different electrolytes. For fundamental investigations, it is beneficial to keep the

electrode-electrolyte interface as simple as possible. For example, by using "native" electrolyte (i.e. without adding any buffer) of pH 1 to 7, we have recently quantitatively determined Pt-surface hydronium pK_a (4.3) using an exclusively surface-specific electrical transport spectroscopy, which agrees well with the theory prediction by quantum mechanics and reactive dynamics, and gives a precise interpretation of the pH-dependent switch of HER kinetics (fundamentally originated from a switch of proton source from hydroniums to neutral water at a pH around pK_a value)[12]. On the other hand, at the higher pH beyond 7, the neutral water molecules remain to be the proton source throughout the pH range 7-14, while the HER activities show notable enhancement with increasing pH[28,29]. In **Chapter 4**, we combined cyclic voltammetry (CV) and electrical transport spectroscopy (ETS) approaches to probe the Pt surface at different pH values and develop molecular-level insights into the pH-dependent HER kinetics in alkaline media. The change in HER Tafel slope from ~110 mV/decade in pH 7–10 to ~53 mV/decade in pH 11–13 suggests considerably enhanced kinetics at higher pH. The ETS studies reveal a similar pH-dependent switch in the ETS conductance signal at around pH 10, suggesting a notable change of surface adsorbates. Fixed-potential calculations and chemical bonding analysis suggest that this switch is attributed to a change in interfacial water orientation, shifting from primarily an O-down configuration below pH 10 to a H-down configuration above pH 10. This reorientation weakens the O–H bond in the interfacial water molecules and modifies the reaction pathway, leading to considerably accelerated HER kinetics at higher pH. Our integrated studies provide an unprecedented molecular-level understanding of the nontrivial pH-dependent HER kinetics in alkaline media. Throughout this work, we have combined experimental electrical transport spectroscopy (ETS), voltammetric and electrochemical impedance spectroscopy (EIS) with theoretical studies to simultaneously probe the on-surface and near surface species during active HER.

References

1. Gasteiger, H.; Yan, S., Dependence of PEM fuel cell performance on catalyst loading. *J. Power Sources* **2004,** *127* (1-2), 162-171.

2. Nørskov, J. K.; Bligaard, T.; Logadottir, A.; Kitchin, J.; Chen, J. G.; Pandelov, S.; Stimming, U., Trends in the exchange current for hydrogen evolution. *J. Electrochem. Soc.* **2005,** *152* (3), J23.

3. Sheng, W.; Gasteiger, H. A.; Shao-Horn, Y., Hydrogen oxidation and evolution reaction kinetics on platinum: acid vs alkaline electrolytes. *J. Electrochem. Soc.* **2010,** *157* (11), B1529.

4. Schuldiner, S., Hydrogen overvoltage on bright platinum: II. pH and salt effects in acid, neutral, and alkaline solutions. *J. Electrochem. Soc.* **1954,** *101* (8), 426.

5. Conway, B.; Bai, L., Determination of adsorption of OPD H species in the cathodic hydrogen evolution reaction at Pt in relation to electrocatalysis. *J. Electroanal. Chem. Interfacial Electrochem.* **1986,** *198* (1), 149-175.

6. Seto, K.; Iannelli, A.; Love, B.; Lipkowski, J., The influence of surface crystallography on the rate of hydrogen evolution at Pt electrodes. *J. Electroanal. Chem. Interfacial Electrochem.* **1987,** *226* (1-2), 351-360.

7. Zheng, J.; Yan, Y.; Xu, B., Correcting the hydrogen diffusion limitation in rotating disk electrode measurements of hydrogen evolution reaction kinetics. *J. Electrochem. Soc.* **2015,** *162* (14), F1470.

8. Subbaraman, R.; Tripkovic, D.; Chang, K.-C.; Strmcnik, D.; Paulikas, A. P.; Hirunsit, P.; Chan, M.; Greeley, J.; Stamenkovic, V.; Markovic, N. M., Trends in activity for the water electrolyser reactions on 3d M(Ni,Co,Fe,Mn) hydr(oxy)oxide catalysts. *Nat. Mater.* **2012,** *11* (6), 550-557.

9. Lamoureux, P. S.; Singh, A. R.; Chan, K., pH Effects on Hydrogen Evolution and Oxidation over Pt(111): Insights from First-Principles. *ACS Catal.* **2019,** *9* (7), 6194-6201.

10. Monteiro, M. C. O.; Goyal, A.; Moerland, P.; Koper, M. T. M., Understanding Cation Trends for Hydrogen Evolution on Platinum and Gold Electrodes in Alkaline Media. *ACS Catal.* **2021,** *11* (23), 14328-14335.

11. Shah, A. H.; Zhang, Z.; Huang, Z.; Wang, S.; Zhong, G.; Wan, C.; Alexandrova, A. N.; Huang, Y.; Duan, X., The role of alkali metal cations and platinum-surface hydroxyl in the alkaline hydrogen evolution reaction. *Nat. Catal.* **2022,** *5* (10), 923-933.

Zhong, G.; Cheng, T.; Shah, A. H.; Wan, C.; Huang, Z.; Wang, S.; Leng, T.; Huang, Y.; Goddard, W. A.; Duan, X., Determining the hydronium pKα at platinum surfaces and the effect on pH-dependent hydrogen evolution reaction kinetics. *Proc. Natl. Acad. Sci.* **2022,** *119* (39), e2208187119.

13. Marković, N. M.; Grgur, B. N.; Ross, P. N., Temperature-Dependent Hydrogen Electrochemistry on Platinum Low-Index Single-Crystal Surfaces in Acid Solutions. *J. Phys. Chem. B.* **1997,** *101* (27), 5405-5413.

14. Durst, J.; Siebel, A.; Simon, C.; Hasché, F.; Herranz, J.; Gasteiger, H. A., New insights into the electrochemical hydrogen oxidation and evolution reaction mechanism. *Energy Environ. Sci.* **2014,** *7* (7), 2255-2260.

15. Rossmeisl, J.; Chan, K.; Skúlason, E.; Björketun, M. E.; Tripkovic, V., On the pH dependence of electrochemical proton transfer barriers. *Catal. Today* **2016,** *262*, 36-40.

16. Ledezma-Yanez, I.; Wallace, W. D. Z.; Sebastián-Pascual, P.; Climent, V.; Feliu, J. M.; Koper, M. T. M., Interfacial water reorganization as a pH-dependent descriptor of the hydrogen evolution rate on platinum electrodes. *Nat. Energy* **2017,** *2* (4), 17031.

17. Parsons, R., The kinetics of electrode reactions and the electrode material. *Surf. Sci.* **1964,** *2*, 418-435.

18. Conway, B.; Bockris, J. O. M., Electrolytic hydrogen evolution kinetics and its relation to the electronic and adsorptive properties of the metal. *J. Chem. Phys.* **1957,** *26* (3), 532-541.

19. Butler, J. A. V., Hydrogen overvoltage and the reversible hydrogen electrode. *Proc. R. Soc. A: Math. Phys. Eng. Sci.* **1936,** *157* (891), 423-433.

20. Bockris, J. O. M.; Parsons, R.; Rosenberg, H., The kinetics of hydrogen evolution on liquid and solid mercury in methanolic solution. *Trans. Faraday Soc.* **1951,** *47* (0), 766-772.

21. Sheng, W.; Myint, M.; Chen, J. G.; Yan, Y., Correlating the hydrogen evolution reaction activity in alkaline electrolytes with the hydrogen binding energy on monometallic surfaces. Energy Environ. Sci. 2013, 6 (5), 1509-1512.

22. Zeradjanin, A. R.; Vimalanandan, A.; Polymeros, G.; Topalov, A. A.; Mayrhofer, K. J. J.; Rohwerder, M., Balanced work function as a driver for facile hydrogen evolution reaction – comprehension and experimental assessment of interfacial catalytic descriptor. *Phys. Chem. Chem. Phys.* **2017,** *19* (26), 17019-17027.

23. Zolfaghari, A.; Chayer, M.; Jerkiewicz, G., Energetics of the underpotential deposition of hydrogen on platinum electrodes: I. Absence of coadsorbed species. *J. Electrochem. Soc.* **1997,** *144* (9), 3034.

24. Zheng, J.; Nash, J.; Xu, B.; Yan, Y., Perspective—Towards Establishing Apparent Hydrogen Binding Energy as the Descriptor for Hydrogen Oxidation/Evolution Reactions. *J. Electrochem. Soc.* **2018,** *165* (2), H27-H29.

25. Sheng, W.; Zhuang, Z.; Gao, M.; Zheng, J.; Chen, J. G.; Yan, Y., Correlating hydrogen oxidation and evolution activity on platinum at different pH with measured hydrogen binding energy. *Nat. Commun.* **2015,** *6* (1), 5848.

26. Cheng, T.; Wang, L.; Merinov, B. V.; Goddard, W. A., Explanation of Dramatic pH-Dependence of Hydrogen Binding on Noble Metal Electrode: Greatly Weakened Water Adsorption at High pH. *J. Am. Chem. Soc.* **2018,** *140* (25), 7787-7790.

27. Zhu, S.; Qin, X.; Yao, Y.; Shao, M., pH-Dependent Hydrogen and Water Binding Energies on Platinum Surfaces as Directly Probed through Surface-Enhanced Infrared Absorption Spectroscopy. *J. Am. Chem. Soc.* **2020,** *142* (19), 8748-8754.

28. Wang, X.; Xu, C.; Jaroniec, M.; Zheng, Y.; Qiao, S.-Z., Anomalous hydrogen evolution behavior in high-pH environment induced by locally generated hydronium ions. *Nat. Commun.* **2019,** *10* (1), 4876.

29. Goyal, A.; Koper, M. T. M., The Interrelated Effect of Cations and Electrolyte pH on the Hydrogen Evolution Reaction on Gold Electrodes in Alkaline Media. *Angew. Chem. Int. Ed.* **2021,** *60* (24), 13452-13462.

30. Chen, X.; McCrum, I. T.; Schwarz, K. A.; Janik, M. J.; Koper, M. T. M., Co-adsorption of Cations as the Cause of the Apparent pH Dependence of Hydrogen Adsorption on a Stepped Platinum Single-Crystal Electrode. *Angew. Chem. Int. Ed.* **2017,** *56* (47), 15025-15029.

31. Janik, M. J.; McCrum, I. T.; Koper, M. T. M., On the presence of surface bound hydroxyl species on polycrystalline Pt electrodes in the "hydrogen potential region" (0–0.4 V-RHE). *J. Catal.* **2018,** *367*, 332-337.

32. Bard, A. J.; Faulkner, L. R.; White, H. S., *Electrochemical methods: fundamentals and applications*. John Wiley & Sons: 2022.

33. Lasia, A., Modeling of hydrogen upd isotherms. *J. Electroanal. Chem.* **2004,** *562* (1), 23-31.

34. Yu, C.; Wang, F.; Zhang, Y.; Zhao, L.; Teng, B.; Fan, M.; Liu, X., H2 Thermal Desorption Spectra on Pt(111): A Density Functional Theory and Kinetic Monte Carlo Simulation Study. *Catalysts* **2018,** *8* (10), 450.

35. Strmcnik, D.; Tripkovic, D.; van der Vliet, D.; Stamenkovic, V.; Marković, N. M., Adsorption of hydrogen on Pt(111) and Pt(100) surfaces and its role in the HOR. *Electrochem. Commun.* **2008,** *10* (10), 1602-1605.

36. Conway, B. E.; Tilak, B. V., Interfacial processes involving electrocatalytic evolution and oxidation of H_2, and the role of chemisorbed H. *Electrochim. Acta* **2002,** *47* (22), 3571-3594.

37. Barber, J.; Morin, S.; Conway, B. E., Specificity of the kinetics of H2 evolution to the structure of single-crystal Pt surfaces, and the relation between opd and upd H. *J. Electroanal. Chem.* **1998,** *446* (1), 125-138.

38. Conway, B. E.; Bai, L., Determination of adsorption of OPD H species in the cathodic hydrogen evolution reaction at Pt in relation to electrocatalysis. *J. Electroanal. Chem. Interfacial Electrochem.* **1986,** *198* (1), 149-175.

39. Lindgren, P.; Kastlunger, G.; Peterson, A. A., A Challenge to the G ∼ 0 Interpretation of Hydrogen Evolution. *ACS Catal.* **2020,** *10* (1), 121-128.

40. Ren, B.; Xu, X.; Li, X. Q.; Cai, W. B.; Tian, Z. Q., Extending surface Raman spectroscopic studies to transition metals for practical applications: II. Hydrogen adsorption at platinum electrodes. *Surf. Sci.* **1999,** *427-428*, 157-161.

41. Kunimatsu, K.; Uchida, H.; Osawa, M.; Watanabe, M., In situ infrared spectroscopic and electrochemical study of hydrogen electro-oxidation on Pt electrode in sulfuric acid. *J. Electroanal. Chem.* **2006,** *587* (2), 299-307.

42. Tang, M. T.; Liu, X.; Ji, Y.; Norskov, J. K.; Chan, K., Modeling Hydrogen Evolution Reaction Kinetics through Explicit Water–Metal Interfaces. *J. Phys. Chem. C* **2020,** *124* (51), 28083-28092.

43. Liu, E.; Jiao, L.; Li, J.; Stracensky, T.; Sun, Q.; Mukerjee, S.; Jia, Q., Interfacial water shuffling the intermediates of hydrogen oxidation and evolution reactions in aqueous media. *Energy Environ. Sci.* **2020,** *13* (9), 3064-3074.

44. Subbaraman, R.; Tripkovic, D.; Strmcnik, D.; Chang, K.-C.; Uchimura, M.; Paulikas, A. P.; Stamenkovic, V.; Markovic, N. M., Enhancing Hydrogen Evolution Activity in Water Splitting by Tailoring Li^+-$Ni(OH)_2$-Pt Interfaces. *Science* **2011,** *334* (6060), 1256-1260.

45. Schmidt, T. J.; Ross, P. N.; Markovic, N. M., Temperature dependent surface electrochemistry on Pt single crystals in alkaline electrolytes: Part 2. The hydrogen evolution/oxidation reaction. *J. Electroanal. Chem.* **2002,** *524-525*, 252-260.

446. Liu, E.; Li, J.; Jiao, L.; Doan, H. T. T.; Liu, Z.; Zhao, Z.; Huang, Y.; Abraham, K. M.; Mukerjee, S.; Jia, Q., Unifying the Hydrogen Evolution and Oxidation Reactions Kinetics in Base by Identifying the Catalytic Roles of Hydroxyl-Water-Cation Adducts. *J. Am. Chem. Soc.* **2019,** *141* (7), 3232-3239.

47. McCrum, I. T.; Koper, M., The role of adsorbed hydroxide in hydrogen evolution reaction kinetics on modified platinum. *Nat. Energy* **2020,** *5* (11), 891-899.

48. Lin, X.-M.; Wang, X.-T.; Deng, Y.-L.; Chen, X.; Chen, H.-N.; Radjenovic, P. M.; Zhang, X.-G.; Wang, Y.-H.; Dong, J.-C.; Tian, Z.-Q.; Li, J.-F., In Situ Probe of the Hydrogen Oxidation Reaction Intermediates on PtRu a Bimetallic Catalyst Surface by Core–Shell Nanoparticle-Enhanced Raman Spectroscopy. *Nano Lett.* **2022,** *22* (13), 5544-5552.

49. Wang, Y.-H.; Wang, X.-T.; Ze, H.; Zhang, X.-G.; Radjenovic, P. M.; Zhang, Y.-J.; Dong, J.-C.; Tian, Z.-Q.; Li, J.-F., Spectroscopic Verification of Adsorbed Hydroxy Intermediates in the

Bifunctional Mechanism of the Hydrogen Oxidation Reaction. *Angew. Chem. Int. Ed.* **2021,** *60* (11), 5708-5711.

50. Li, J.; Ghoshal, S.; Bates, M. K.; Miller, T. E.; Davies, V.; Stavitski, E.; Attenkofer, K.; Mukerjee, S.; Ma, Z.-F.; Jia, Q., Experimental Proof of the Bifunctional Mechanism for the Hydrogen Oxidation in Alkaline Media. *Angew. Chem. Int. Ed.* **2017,** *56* (49), 15594-15598.

51. Cong, Y.; McCrum, I. T.; Gao, X.; Lv, Y.; Miao, S.; Shao, Z.; Yi, B.; Yu, H.; Janik, M. J.; Song, Y., Uniform Pd0.33Ir0.67 nanoparticles supported on nitrogen-doped carbon with remarkable activity toward the alkaline hydrogen oxidation reaction. *J. Mater. Chem. A* **2019,** *7* (7), 3161-3169.

52. Qiu, Y.; Xin, L.; Li, Y.; McCrum, I. T.; Guo, F.; Ma, T.; Ren, Y.; Liu, Q.; Zhou, L.; Gu, S.; Janik, M. J.; Li, W., BCC-Phased PdCu Alloy as a Highly Active Electrocatalyst for Hydrogen Oxidation in Alkaline Electrolytes. *J. Am. Chem. Soc.* **2018,** *140* (48), 16580-16588.

53. Schwämmlein, J. N.; Stühmeier, B. M.; Wagenbauer, K.; Dietz, H.; Tileli, V.; Gasteiger, H. A.; El-Sayed, H. A., Origin of superior HOR/HER activity of bimetallic Pt-Ru catalysts in alkaline media identified via Ru@ Pt core-shell nanoparticles. *J. Electrochem. Soc.* **2018,** *165* (5), H229.

54. Intikhab, S.; Snyder, J. D.; Tang, M. H., Adsorbed Hydroxide Does Not Participate in the Volmer Step of Alkaline Hydrogen Electrocatalysis. *ACS Catal.* **2017,** *7* (12), 8314-8319.

55. Rebollar, L.; Intikhab, S.; Snyder, J. D.; Tang, M. H., Determining the viability of hydroxide-mediated bifunctional HER/HOR mechanisms through single-crystal voltammetry and microkinetic modeling. *J. Electrochem. Soc.* **2018,** *165* (15), J3209.

56. Wang, Y.; Wang, G.; Li, G.; Huang, B.; Pan, J.; Liu, Q.; Han, J.; Xiao, L.; Lu, J.; Zhuang, L., Pt–Ru catalyzed hydrogen oxidation in alkaline media: oxophilic effect or electronic effect? *Energy Environ. Sci.* **2015,** *8* (1), 177-181.

57. Xue, S.; Garlyyev, B.; Watzele, S.; Liang, Y.; Fichtner, J.; Pohl, M. D.; Bandarenka, A. S., Influence of Alkali Metal Cations on the Hydrogen Evolution Reaction Activity of Pt, Ir, Au, and Ag Electrodes in Alkaline Electrolytes. *ChemElectroChem* **2018,** *5* (17), 2326-2329.

58. Huang, B.; Rao, R. R.; You, S.; Hpone Myint, K.; Song, Y.; Wang, Y.; Ding, W.; Giordano, L.; Zhang, Y.; Wang, T.; Muy, S.; Katayama, Y.; Grossman, J. C.; Willard, A. P.; Xu, K.; Jiang, Y.; Shao-Horn, Y., Cation- and pH-Dependent Hydrogen Evolution and Oxidation Reaction Kinetics. *JACS Au* **2021,** *1* (10), 1674-1687.

59. Bender, J. T.; Petersen, A. S.; Østergaard, F. C.; Wood, M. A.; Heffernan, S. M. J.; Milliron, D. J.; Rossmeisl, J.; Resasco, J., Understanding Cation Effects on the Hydrogen Evolution Reaction. *ACS Energy Lett.* **2023,** *8* (1), 657-665.

60. Strmcnik, D.; Uchimura, M.; Wang, C.; Subbaraman, R.; Danilovic, N.; Van Der Vliet, D.; Paulikas, A. P.; Stamenkovic, V. R.; Markovic, N. M., Improving the hydrogen oxidation reaction rate by promotion of hydroxyl adsorption. *Nat. Chem.* **2013,** *5* (4), 300-306.

61. Li, P.; Jiang, Y.; Hu, Y.; Men, Y.; Liu, Y.; Cai, W.; Chen, S., Hydrogen bond network connectivity in the electric double layer dominates the kinetic pH effect in hydrogen electrocatalysis on Pt. *Nat. Catal.* **2022,** *5* (10), 900-911.

CHAPTER 2

The role of alkali metal cations and platinum-surface hydroxyl in the alkaline hydrogen evolution reaction

2.1. Introduction and background

The HER is one of the most fundamental and critical reactions in renewable energy conversion and storage devices including electrolysers that convert and store intermittent renewable electricity in chemical form by producing hydrogen. On the other hand, the hydrogen oxidation reaction (HOR) plays a critical role in fuel-cell technologies that convert stored chemical energy into electricity. The HER/HOR mechanism and kinetics are drastically different in acidic and alkaline media[1, 2]. Platinum (Pt) is a state-of-the-art electrocatalyst for these reactions, and thus significant efforts have been devoted to understanding the reaction mechanism and kinetics of Pt-based electrocatalytic systems[3-5]. Hitherto, various hypotheses have been proposed to identify and understand the reaction descriptors that account for the effect of pH on the HER on Pt electrode surfaces. It has been well recognized that the HER rate and mechanism are related to the strength of the hydrogen binding energy (HBE) of the metal. For example, on the basis of a density functional theory (DFT) database of hydrogen chemisorption energies, Norskov et al. introduced the so-called volcano plot and confirmed that Pt represents an optimum HER catalyst, particularly in acidic environments[4].Although the HBE of a pure metal surface can in principle serve as an effective physical descriptor for the HER, the experimental determination of the relevant physical parameters is often complicated by the presence of the electrolyte and different surface adsorbates,

particularly in alkaline electrolytes where the adsorbates are more complex. For example, Yan and colleagues studied the HER in different pH-buffered electrolytes and suggested that a monotonic decrease in the HER activities by increasing the pH can be correlated with continuously strengthened electrochemical HBE values[6]. On the other hand, Koper and co-workers suggested that a positive shift in the peak for hydrogen underpotential deposition (H_{upd}) in cyclic voltammetry (CV) is not because of HBE changes but originates from destabilization of the OH_{ad} species on Pt(100) and Pt(110) sites by the presence of alkali metal cations near the interface[7, 8]. Moreover, Koper and colleagues have also shown that the HBE descriptor cannot fully explain the pH-dependent catalytic behavior on Pt(111), which shows significant pH-dependent HER kinetics but only a small dependence of the H_{upd} peak potential shift on the pH[9]. Thus, despite the undeniable success of the HBE in acidic media, it is not an unambiguous descriptor for HER/HOR kinetics in alkaline media, largely due to the more complex electrolyte environment and the elusive role of different surface adsorbates that may modify the interfacial molecular structures and reaction pathways. Markovic and others ascribed the slower HER kinetics in alkaline media to the high energy barrier for H_2O dissociation compared with H_3O^+ in acidic media[10-12], and suggested that the HER kinetics in alkaline media can be improved by the presence of oxophilic groups that can stabilize OH_{ad}, which in turn facilitates H_2O dissociation[13]. Later, the same group observed a monotonic relationship between the HER activity and the OH_{ad} affinity of the oxophilic groups, and concluded that the HER activity follows the Bronsted–Evans–Polanyi principle to promote the HER kinetics; from this, they proposed a bifunctional mechanism in which the edges of oxophilic metal clusters ($M(OH)_2$) promote H_2O dissociation and the production of adsorbed hydrogen atoms (Had) on nearby Pt surfaces that then recombine into molecular hydrogen[14]. This bifunctional mechanism has been supported by a number of studies[15-18]. For example, Jia and co-

workers experimentally verified the bifunctional mechanism through combined electrochemical and operando spectroscopic data[15], and robustly demonstrated that the presence of hydroxyl groups on surface Ru sites in the HOR potential region plays a key role in promoting the rate-determining Volmer step[15]. Moreover, McCrum and Koper recently investigated the further role of OH_{ad} on the HER activity in alkaline media, and demonstrated that the HER activity exhibits a volcano-type relationship with the hydroxyl binding strength, supporting the Bronsted–Evans–Polyani relationship[19]. In addition to the HBE and the bifunctional mechanism, Koper and co-workers suggested that the potential of zero free charge may play an important role[9]. In this picture, the HER/HOR region in acidic media is closer to the potential of zero free charge (~0.34 V_{RHE} (the voltage versus the reversible hydrogen electrode)), and the reorganization energy for interfacial water to move a proton through the electrical double layer (EDL) is smaller; by contrast, the HER/HOR region in alkaline media is far from the potential of zero free charge (~1.0 V_{RHE}, that is, closer to the OH_{ad} region) and the strong electric field in the HER/HOR region leads to a larger interfacial water reorganization energy that could limit the transfer of OH^- through the double layer[9].

Apart from the differences in these distinct theories and different levels of success in various aspects, none of them consider the effect of alkali metal cations (AM^+) on the HER kinetics, which can hardly be ignored in alkaline electrolytes. For example, Markovic and co-workers observed that the HER activity on a $Ni(OH)_2$–Pt surface was promoted in the presence of Li^+ cations, which they attributed to water dissociation[13]. Bandarenka and colleagues reported a similar promotion of the HER activity on a Pt electrode by AM^+ (ref.[20]), and suggested that the cations may alter the HBE, thus altering the HER activity[20]. Jia and collaborators attributed the enhancement in HER activity to the presence of OH_{ad}–$(H_2O)_x$–AM^+ in the double-layer region, which facilitates the

removal/transport of OH_{ad} into the bulk, forming OH^{-}–$(H_2O)_x$–AM^{+} as per the hard–soft acid–base theory, thereby promoting the HER[16]. Koper and co-workers recently suggested a change in the rate-determining step from the Heyrovsky to the Volmer step in Li^{+}- and K^{+}-containing electrolytes, respectively[21]. Overall, although an enhancement of the HER activity on a Pt electrode in the presence of Li^{+} when compared with other larger AM^{+} has been consistently observed, a full understanding of this phenomenon has been a topic of considerable debate. Therefore, to more completely understand the descriptor that dictates the HER activity in alkaline media, it is essential to investigate how the different cations alter the local (on-surface or near-surface) chemical environment at the electrode–electrolyte interface.

Here we address this issue by systematically studying the influence of cations on the HER on a Pt surface in alkaline media. We observed that the HER activity in alkaline media is clearly dependent on the exact AM^{+} ($Li^{+} > Na^{+} > K^{+}$), which is consistent with previous studies[20, 22]. We further use a unique electrical transport spectroscopy (ETS) approach to probe the Pt-surface adsorbates directly at variable potentials, and electrochemical impedance spectroscopy (EIS) to study the near-surface environment in the EDL and the charge-transfer resistance (R_{ct}) at the electrode–electrolyte interface. On the basis of these comprehensive on-surface and near-surface signals, we conduct DFT calculations with explicit solvation, including static calculations, grand canonical DFT calculations, ab initio molecular dynamics (AIMD) simulations and micro-solvation molecular-cluster calculations to develop molecular-level insights into the surface-adsorption properties, solvation structure and the Pt–water interface dynamics in the presence of cations and surface OH_{ad} species. Together, we experimentally and theoretically resolve the elusive role of AM^{+} and demonstrate that AM^{+} play an indirect role in modifying the adsorption strength and coverage of the hydroxyl species ($-OH_{ad}@Li^{+} > -OH_{ad}@Na^{+} > -OH_{ad}@K^{+}$) under the H_{upd}/HER

potential regime, where the higher OH_{ad} coverage with smaller AM^+ promotes the HER activity. Specifically, our integrated studies reveal that Li^+ cations destabilize OH_{ad} on the Pt surface least (compared with Na^+ and K^+) and help to retain more OH_{ad} that in turn act as both proton acceptors and donors to the nearby water molecules and thus facilitate the Volmer-step kinetics and the HER activity in alkaline media (similar to the bifunctional mechanism), as also confirmed via the greatly reduced charge-transfer resistance observed in EIS studies. Our direct experimental and theoretical evidences provide critical fundamental insights into how and why AM^+ influence the HER kinetics in alkaline media. This could enable an important vision for the design of future electrolysers with both improved energy efficiency and reduced cost.

2.2. Materials and methods

2.2.1. Chemicals

Lithium hydroxide (LiOH; >98%), sodium hydroxide (NaOH; 98%), potassium hydroxide (KOH; 87.4%) and perchloric acid (70%, PPT grade) were all purchased from Thermo Fisher Scientific. All aqueous solutions were prepared using deionized water (18.2 MΩ cm) obtained from an ultrapure purification system (Aqua Solutions).

2.2.2. Electrochemical measurements

All of the electrochemical measurements were performed using a typical three-electrode setup. A Pt rotating disc was used as the working electrode, and Pt wire and Ag/AgCl were used as the counter and reference electrodes, respectively. All of the potentials reported are versus the RHE, calibrated in the same electrolyte by measuring the potential of the HOR/HER currents at zero corresponding to 0 V_{RHE}.

2.2.3. Impedance measurements

The impedance spectra were measured using frequencies from 10^5 to 1 Hz with an amplitude of 10 mV_{rms} at different applied voltages. Cyclic voltammograms were conducted between each potential point in the EIS measurement to avoid any influence from surface passivation. Equivalent circuits were fitted to the data using AfterMath software version 1.6.10513.

2.2.4. Synthesis of PtNWs

The PtNWs for the ETS measurements were synthesized following a previously reported protocol [23]. Briefly, $Pt(acac)_2$ (ac = acetylacetonate) (20 mg), $Ni(acac)_2$ (30 mg), $W(CO)_6$ (1.6 mg), glucose (135 mg) and 60 mg of polyvinylpyrrolidone (MW 40,000) were dissolved in 1-octadecene (2 ml) and oleylamine (3 ml). After sonicating for 15 min, the solution was sealed with argon. The mixture was then heated to 140 °C for 4 h. The product was centrifuged with ethanol for 15 min, followed by cyclohexane for 20 min. Finally, the product was centrifuged in a mixture of cyclohexane (5 ml) and ethanol (15 ml) for 20 min. The final product was dispersed in ethanol for device preparation.

2.2.5. Preparation of PtNW films

A free-standing PtNW film was assembled on-chip from the as-prepared PtNW suspension using a co-solvent evaporation method[24]. Briefly, the PtNW suspension in ethanol (400 µl, 0.4 mg ml^{-1}) was added dropwise into a beaker (about 9 cm in diameter) filled with deionized water. The thin film of PtNWs from the top of the water surface was then transferred onto the device.

2.2.6. Fabrication of the PtNW electrochemical device

The device fabrication followed an approach similar to that previously reported by our group[24]. Typically, a poly(methyl methacrylate) (PMMA; A8, MicroChem) film was prepared via spin

coating onto the surface of the substrate (p^{++} silicon wafer with 300 nm thermal oxide) with pre-patterned Au electrodes (Ti/Au, 50/50 nm). E-beam lithography was then used to open windows on the PMMA, which created the desired patterns on the substrate. After removal of the PMMA template, PtNWs were deposited on the device substrate with the desired patterns. To rule out the influence of the electrolyte and to avoid electrochemical reactions on the Au electrodes, another layer of PMMA (~500 nm thick, electrochemically inert) was then deposited on the PtNW device via spin coating. A smaller window that only exposed PtNWs was opened using e-beam lithography. The device was finally used for in-device electrochemistry and in situ ETS measurements.

2.2.7. In-device CV and in situ ETS

A two-channel source/measure unit (SMU; Agilent B2902a) was used for the measurements. The first SMU channel was used as a potentiostat to control the potential of the source electrode compared with the reference electrode (V_G), while collecting the current (I_G) through the counter electrode at a scan rate of 50 mV s^{-1}. An SR830 lock-ln amplifier (Stanford Research Systems) was used to supply a small sinusoidal current (10 μA) between the source and drain electrodes and for collecting the corresponding source–drain voltage (V_{SD}). The source–drain voltage was then used to measure the conductance.

2.2.8. Slab model setup and DFT methods

The Pt–water interface is modelled using a Pt(111) slab and an explicit water slab on top of it. The Pt slab is a three-layer 4 × 4 supercell of Pt(111) termination with an area of 1.10 nm^2. The explicit water slab is 6 Å thick, and contains 22 water molecules (estimated from the water density of 1.0 g cm^{-3} at room temperature). The bottom two layers of the Pt slab are constrained as the bulk

region, and everything else is allowed to relax as the interface region. A vacuum slab of 10 Å thickness was added in the *Z* direction to avoid spurious interactions between periodic images.

The solvation configuration for the production run was sampled through the random placement of water molecules in the water-slab region followed by local optimization at the DFT level, with a sampling size of 50 configurations, using our open-source Python package GOCIA (https://github.com/zishengz/gocia). The cation is introduced by replacing a water molecule and then re-optimizing the geometry. The surface OH_{ad} is introduced by placing an OH species onto the Pt surface and then re-optimizing the geometry. Although our calculations use Pt(111) as the model system, we expect a similar conclusion to hold true for other surfaces, and it is noted that the stepped surfaces have even more favourable OH_{ad} compared with the Pt(111) terrace[19].

The geometry optimizations were performed using the Perdew–Burke–Ernzerhof functional [25] and projector augmented-wave pseudopotentials[26] with the Vienna ab initio simulation package program (version 5.4.1)[27-30]. D3 correction was used to better account for the dispersion interactions[31]. The convergence criteria for geometry (self-consistent field) are set to 10^{-5} eV for energy and 0.02 eV $Å^{-1}$ for forces. Due to the relatively large system and sampling size, only the Γ k-point is sampled in the reciprocal space of the Brillouin zone throughout, and the cutoff energy for the kinetic energy of the plane waves was 400 eV. The Bader charges are calculated from the charge density output using Bader Charge Analysis code[32].

2.2.9. Grand canonical DFT calculations

Under a constant applied potential, the electrode surface is effectively a grand canonical ensemble where the number of electrons is varied to adapt to the change in the work function of the surface (caused by adsorbates or near-surface species). The potential-dependent electronic free energy of the surface ($G(U)$) can be approximated using the surface-charging method[33]:

$$G(U) = E(U) - q(U) \cdot FU \approx E(U_0) - \frac{1}{2}C(U - U_0)^2 \qquad (2\text{-}1)$$

Here, $E(U)$ is the electronic energy of the surface under a potential U, which is calculated by referencing the Fermi level of the system against the vacuum level; $q(U)$ is the surface charge difference referenced against the neutral system, and F is the Faraday constant; U_0 is the potential of zero charge in the vacuum scale, and C is the effective capacitance of the electrochemical interface. By varying the number of electrons in the system, the $E(U)$ of the system at the corresponding U and $q(U)$ can be obtained, and thereby a parabolic relationship between $G(U)$ and U can be fitted by sampling a series of q values. The U (in the vacuum scale) can be converted to the RHE scale by referencing it against the experimental U_{SHE} (standard hydrogen electrode, 4.44 V)[34] and adding a pH correction of 0.0592 × pH.

2.2.10. AIMD simulations

The AIMD simulations are performed on the optimized structures using the same DFT setting as for the geometry optimization using the VASP program (version 5.4.1). The simulations were performed in the *NVT* (canonical) ensemble at 300 K using the Nosé–Hoover thermostat. The time step was set to 1 fs, and the 100 ps trajectory after the equilibration of the system was collected for analysis. Multiple independent simulations starting with different cation height values were performed, and we observed little dependence of the obtained equilibrium on the initial conditions. The RDF analysis was performed using the VMD program (version 1.9.4a48)[35].

2.2.11. Calculation of adsorption energies

The adsorption energy of OH on the surface to form OH_{ad} is calculated using

$$E_{\mathrm{ads}}^{\mathrm{OH}} = E(* \mathrm{OH_{ad}}) - E(*) - E(\mathrm{OH}) \qquad (2\text{-}2)$$

Here, the energy E is from the static calculation on a single configuration; the symbol, $*$ denotes the Pt–water interface, and OH denotes an isolated OH species (via implicit solvation calculation or experimentally determined solvation free energy. we calculate OH binding energy from three protocols: (i) Static calculation with constant charge, which gives binding energy; (ii) Static calculation with grand canonical treatment for electrons (constant potential), which gives potential-dependent binding free energy; and (iii) potential energy averaged over a 100-ps AIMD trajectory, which is binding enthalpy.

The desorbed state of the OH^- (solvated in bulk solution) is not explicitly included in the calculation, since the simulation box does not have a sufficiently thick explicit water layer to converge to bulk solution behavior. The free energy of the desorbed state of OH^- is expected to be the same for all three cationic cases. Since we focus more on the cationic trends ($\Delta\Delta G$) instead of the absolute binding energies (ΔG), the choice of solvation free energy calculations scheme would not affect the main conclusions of this work, but merely translate the binding energies by a same value. In the main text, we used the solvation free energy from a polarizable implicit solvation model (with the linearized Poisson-Boltzmann equation). Alternative references for calculating binding energies can be used, which will cause a shift of the binding energies in all cases by the same amount, but the cationic trends will not be affected. For example, we have recalculated adsorption energies using experimentally determined solvation free energy of hydroxide in water (-106.4 ± 0.5 kcal/mol) reported in ref [36], which is expected to underestimate the adsorption energy, as the adsorbed state is not as fully solvated as the starting ion. In Fig. 2.1, the binding energies are shifted to a more positive value, but the cationic trend persists.

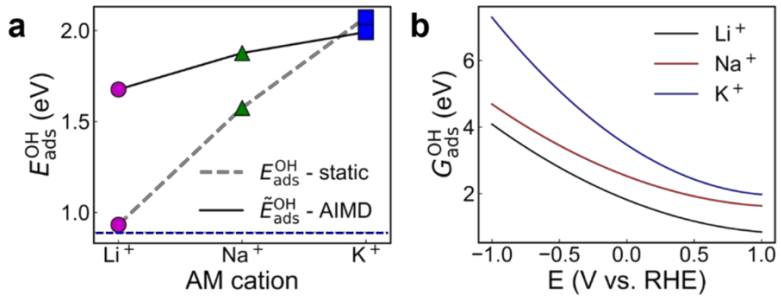

Figure 2.1: Adsorption energy of adsorbed hydroxyls (OH_{ad}) on Pt surface. (a) Adsorption energy of OH in presence of Li^+, Na^+, and K^+ ions, from static calculation and from AIMD simulation. The dotted horizontal line marks the adsorption energy in absence of any cation. (b) The potential-dependent G_{ad}^{OH} in presence of Li^+, Na^+, and K^+ ions in the potential window of 1.0 V to -1.0 V vs. RHE.

The static DFT energy E can be replaced by the trajectory-averaged potential energy $\tilde{E}$ from the AIMD simulation to yield the trajectory-averaged adsorption enthalpy:

$$\tilde{E}_{ads}^{OH} = \tilde{E}(* OH_{ad}) - \tilde{E}(*) - E(OH) \qquad (2\text{-}3)$$

We can also replace E with the potential-dependent free energy $G(U)$ to yield the potential-dependent free energy of adsorption:

$$G_{ads}^{OH}(U) = G(U; * OH_{ad}) - G(U; *) - E(OH) \qquad (2\text{-}4)$$

2.2.12. Micro-solvation model setup and DFT methods

The isolated forms of the hydrated cations are $Li(H_2O)_4^+$, $Na(H_2O)_5^+$ and $K(H_2O)_6^+$, which are the typical hydration structures taken from ref.[37]. The outer-shell solvation configuration around the water and hydrated cations is sampled as a micro-solvation molecular cluster via the random placement of water molecules within a spherical region of 7 Å radius (around the species to be solvated) followed by local optimization at the DFT level, with a sample size of 50 configurations, using the Genmer module in the Molclus program[38].

The geometry optimizations were performed using the B3LYP functional[39, 40] and def-TZVP basis sets[41] using the Gaussian 16 program [42](Revision C.01). D3 correction[31] with Becke–Johnson damping[43] was used to better account for the dispersion interactions. Hirshfeld population analysis

and Mayer bond order analysis were performed using the Multiwfn program[44] on the converged wavefunctions from DFT calculations.

2.3. Results and discussion

2.3.1. Cation-dependent HER activity and surface adsorbates

Using CV and linear sweep voltammetry (LSV) we first examined the influence of cations on the Pt disc electrode with a conventional three-electrode system in alkaline electrolytes at pH 13 with different AM^+ (Li^+, Na^+ and K^+). The cyclic voltammograms in the HER/HOR regime show that the H_{upd} peak exhibits a clear dependence on the specific AM^+ (Fig. 2.2a). The peak potential is more positive in 0.1 M KOH, followed by NaOH and LiOH (inset in Fig.2.2a). A consistent and even more prominent trend has previously been observed on single-crystal Pt surfaces by Koper and co-workers[7, 45] in which the H_{upd} peak was attributed not only to H adsorption but also to the replacement of OH_{ad} by H_{ad} (ref.[45]). Thus, our work is in agreement with the previous reports that the negative peak shift with smaller AM^+ is an indication that Li^+ cations better stabilize (or lesser destabilize) OH_{ad} in the lower potential regime compared with Na^+ and K^+ cations. Linear sweep voltammograms demonstrate that the highest HER activity was observed in the case of Li^+ followed by Na^+ and K^+ cations (Fig. 2.2b), which is also consistent with previous studies[16, 46].

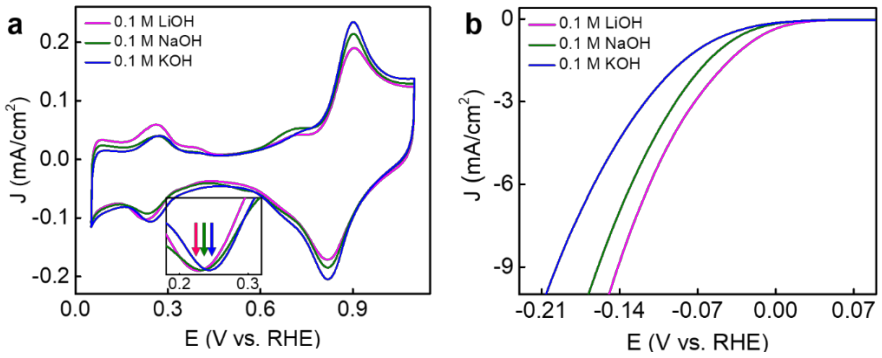

Figure 2.2: Voltammetric studies in alkali electrolyte with different alkali metal cations. (a) Cyclic voltammograms on a stationary polycrystalline Pt disc electrode at a scan rate of 100 mV s^{-1} (the inset

shows an expanded view of the normalized H_{upd} peak) and (b) HER polarization curves (iR-corrected; i, current; R, resistance) collected at room temperature on a polycrystalline Pt disc electrode in N_2-saturated 0.1 M MOH (M = Li, Na and K) at a scan rate of 5 mV s^{-1} with a rotation speed of 1,600 revolutions per min.

To understand the impact of these different AM^+ on the surface adsorbates in the H_{upd}/HER regime, we next carried out ETS studies to probe the adsorbed species directly on the Pt surface. The ETS approach uses ultrafine Pt nanowires (PtNWs) as a model catalyst[24, 47], and involves the concurrent measurement of the PtNW conductance during electrochemical studies at different electrochemical potentials (Fig. 2.3a) (see Methods and ref.[24] for the detailed working principle). The PtNWs (~2 nm in diameter) used in ETS studies show qualitatively similar CV and LSV results (Fig. 2.3) with a consistent trend of AM^+ dependence to other types of Pt catalyst (for example, the Pt disc electrode).

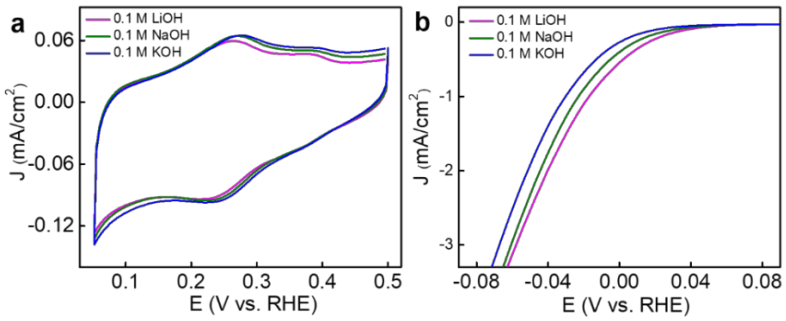

Figure 2.3: Voltammetric studies in different alkali metal cations. (a) CV and (b) LSV of Pt NWs collected at room temperature in N_2-saturated 0.1 M MOH (M= Li^+, Na^+ and K^+).

Using the ETS approach, when the diameter (d) of the ultrafine PtNWs is smaller than the electron mean free path ($\lambda \approx 5$ nm)[48], their resistance is particularly dependent on the surface adsorbates due to surface-adsorbate-induced scattering of the conduction electrons, producing a resistance change according to equation (2-1)[24]:

$$\rho = \rho_0 \left(\left(\frac{1-p}{1+p} \right) \times \frac{\lambda}{d} \right) \quad (d \ll \lambda) \qquad (2\text{-}1)$$

where ρ and ρ_0 are the resistivity of the one-dimensional PtNWs and the bulk metal, respectively, λ is the mean free path of the electron and p is a specularity parameter, which has a value ranging from 0 (for highly diffusive scattering) to 1 (completely specular scattering) (Fig. 2.3b)[48]. The different surface adsorbate modifies the specularity value (p) and thus the resistance of the nanowires. It should be noted such surface scattering is wholly sensitive to the surface adsorbates and is not sensitive to the electrostatic or electrochemical potential. For example, previous studies have shown that a constant conductance at different electrochemical potentials is obtained when there is a stable surface-adsorbate layer (for example, CO or I^-) that does not change with potential[24, 47], confirming the insensitivity of the metallic PtNWs to the varying electrochemical potential. Thus, the ETS approach offers a unique signal-transduction pathway to probe the surface adsorbates exclusively, with little interference from the electrochemical potential or the bulk electrolyte environment, which is difficult to achieve with other analytical approaches that are often convoluted with the near-surface (for example, EDL) or bulk electrolyte background. In addition, compared with interfacial-charge-transfer-based CV studies that cannot usually resolve the surface adsorbates during the active catalytic process (for example, in HER potential regime) due to the dominance of the much larger catalytic current over the surface-adsorbate charge transfer, ETS is wholly sensitive to the surface adsorbates and is insensitive to the catalytic current. Thus, the ETS approach can enable probing of the surface adsorbates of active catalytic surfaces in action, which is essential for deciphering catalytic molecular pathways.

We first closely compared the ETS measurements with the corresponding the CV curve when the potential was gradually changed from 1.10 to −0.05 V_{RHE} (Fig. 2.4c) and four distinct regions were consistently shown: (1) the $O/OH_{ad/des}$ region (1.10–0.52 V_{RHE}); (2) the EDL region (in which OH_{ad} is replaced by H_2O) (0.52–0.35 V_{RHE}); (3) the H_{upd} regime (0.35–0.08 V_{RHE}); and (4) the HER

regime (from 0.08 to −0.05 V_{RHE}). The lowest conductance observed in the high-potential regime is attributed to the larger scattering from the strongly bonded OH_{ad} on the Pt surface, which significantly reduces the conductance of the PtNWs. Scanning the potential toward the lower potential regime results in a monotonic increase in conductance due to the gradual replacement of OH_{ad} by H_2O. The conductance increase slowed in the double-layer regime where the Pt surface is nearly completely reduced and most of the OH_{ad} are replaced by H_2O. Further sweeping of the potential to the more negative regime results in H_{upd} on the electrode surface (replacement of surface-adsorbed H_2O and residual OH_{ad} by H_{upd}), which further reduces the scattering and increases the conductance. The conductance eventually saturates at a nearly stable value below 0.15 V_{RHE} (beyond the H_{upd} peak in the CV curve) due to the high coverage of adsorbed hydrogen. The ETS conductance measurement retains the nearly saturated conductance well into the HER regime (0.08 to −0.05 V_{RHE}), suggesting a largely similar surface-adsorption status in the HER regime.

We further compared the ETS data obtained for the three different cations (Li^+, Na^+ and K^+). It was found the ETS data show essentially the same conductance in the high-potential regime (1.10–1.00 V_{RHE}), suggesting a similar hydroxyl adsorption state at such potentials. As we scan the potential towards the lower potential regime, a notable conductance increase is observed in all cases, following a largely similar trend. However, it is interesting to note that the conductance increase is less pronounced with a smaller slope in the case of Li^+ cations compared with that of Na^+ and K^+ (Fig. 2.4d).

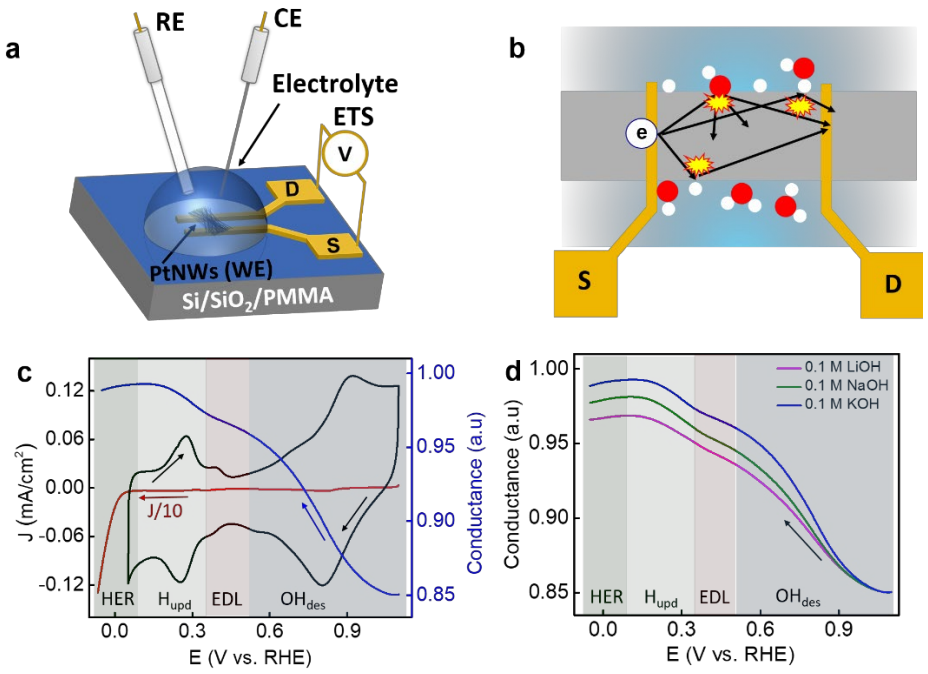

Figure 2.4: Schematic illustration and working principle of the ETS measurements. (a) On-chip PtNW device for ETS measurements, where RE, CE and PtNWs (WE) are the reference, counter and working electrodes, respectively, and S and D represent the source and drain terminals, respectively. (b) Electron-scattering mechanism of various adsorbate molecules (red and white color represents O and H atoms respectively) on the PtNWs. (c) Typical cyclic voltammogram (black), negative sweeping branch to the HER region (red) and ETS spectrum (blue). The red curve is divided by ten due to the much larger HER current in the HER potential window. The hydroxyl desorption (OH_{des}), EDL, H_{upd} and HER regions are highlighted with different background colors. (d) Normalized ETS conductance signal versus potential of the PtNW device in 0.1 M MOH (M = Li, Na and K) electrolyte solutions with different AM^{+}.

Considering that the conductance increase primarily results from the replacement of OH_{ad} by H_2O and then by H_{upd}, the smaller increase in conductance in the presence of Li^{+} cations suggests that fewer OH_{ad} are being desorbed or replaced by H_2O or H_{ad} compared with that of the other larger cations (Na^{+} and K^{+}). We note that the difference among these three cations persist throughout the entire potential regime down to −0.05 V_{RHE}, suggesting that different amounts of OH_{ad} remained on the Pt in the H_{upd}/HER potential window.

2.3.2. Theoretical insight into the role of cations on surface adsorbates

Although it has commonly been perceived that OH_{ad} may not be stable in the H_{upd}/HER potential regime, there are occasional suggestions that some level of OH_{ad} may persist at this potential range[7, 8], which is consistent with our ETS studies. To understand these experimental findings, we performed theoretical studies to investigate the extent of OH_{ad} in the presence of different cations. To gain insight into how and why different cations influence the surface-adsorption properties, DFT calculations were performed on the Pt(111)–water interface, which is modelled by the Pt(111) slab covered with an explicit water layer (Fig. 2.5) and the DFT-optimized geometries are shown in Fig. 2.6.

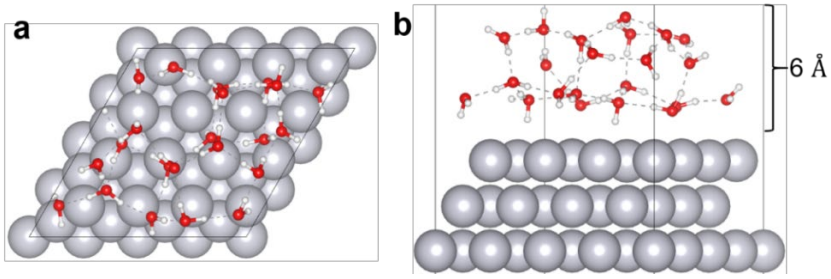

Figure 2.5: Explicit solvation slab model for the Pt(111)/water interface. (a) Top view and (b) side view of the Pt(111)/water interface model. A water slab of 6 Å thickness is added above a 3-layer 4x4 Pt(111) slab.

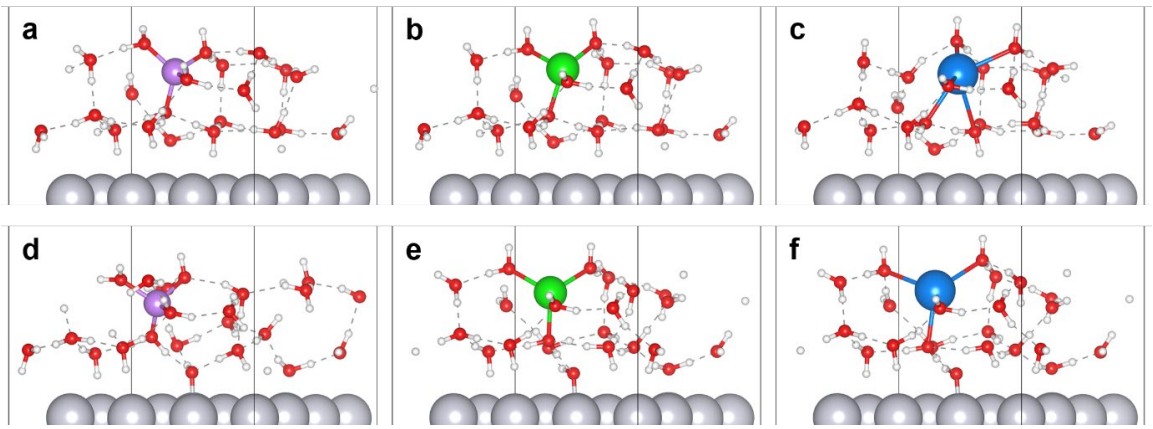

Figure 2.6: DFT-optimized geometries of Pt(111)/water and Pt(111)-OH_{ad}/water with cations. Side views of the optimized geometry of Pt(111)/water interface with (a) Li^+, (b) Na^+, (c) K^+, and Pt(111)-OHad/water interface with (d) Li^+, (e) Na^+, (f) K^+.

The adsorption energy of OH_{ad} (E_{ad}^{OH}) on Pt(111) is calculated to be −3.46 eV, −2.81 eV and −2.32 eV in the presence of Li^+, Na^+ and K^+, respectively (Fig. 2.7a) (see below for estimation of the statistical fluctuations from solvent dynamics). Compared with the case of a pure water environment (−3.50 eV), the presence of cations destabilizes the OH_{ad}, and the extent of such destabilization follows the trend of $K^+ > Na^+ > Li^+$. Grand canonical DFT calculations (Fig. 2.7b) confirm that this trend persists for the potential-dependent adsorption free energy of OH (G_{ad}^{OH}) throughout the entire electrochemical window (−1.0 to 1.0 V_{RHE}), and that OH_{ad} is favorable even under a more negative potential.

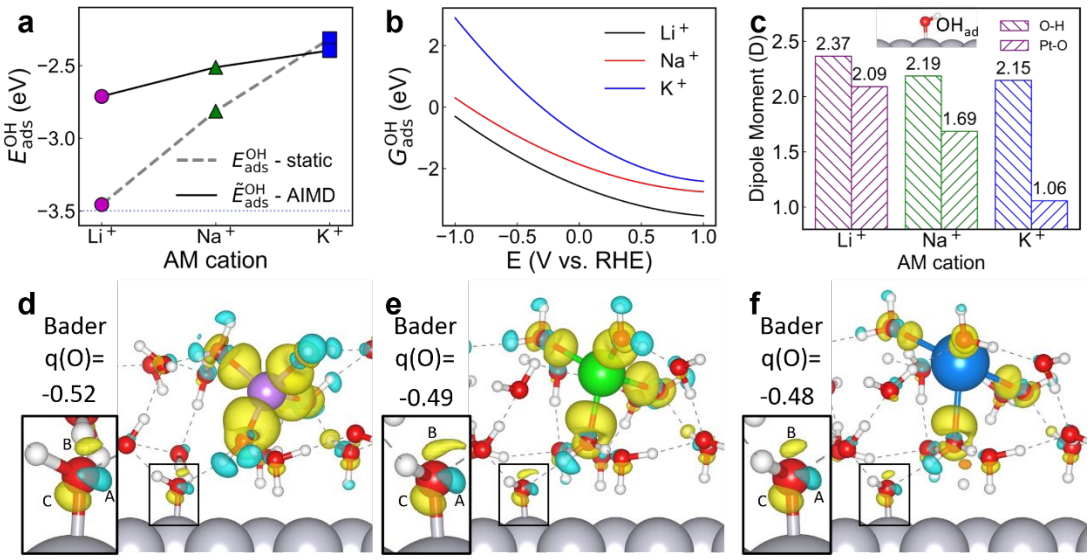

Figure 2.7: Effect of cations on adsorption of OH_{ad} at the Pt(111)-water interface. (a) Adsorption energy of OH (E_{ad}^{OH}) in the presence of Li^+, Na^+ and K^+ from static calculations and AIMD simulations (the statistical spread is omitted here for clarity). The dotted horizontal line marks the adsorption energy in the absence of any cation. (b) The potential-dependent (G_{ad}^{OH}) in the presence of Li^+, Na^+ and K^+ in the potential window of 1.0 V_{RHE} to −1.0 V_{RHE}. (c) Bar plot showing the dipole moment of OH_{ad} based on Bader charges. (d–f) Electron density difference maps of the Pt(111)–OH_{ad}–water interface after introducing Li^+ (d), Na^+ (e) and K^+ (f) plotted at the isovalue of 0.0025 electrons $Å^{-3}$. Yellow and cyan isosurfaces represent spatial regions experiencing an increase or decrease in electron density, respectively. The insets are expanded views of the OHad regions, with the key isosurfaces and Bader charges on O (q(O), in |e|) labelled.

Our DFT calculations show that the adsorption strength of OH_{ad} follows the order of $Li^+ > Na^+ > K^+$, which is consistent with the experimental observations in ETS studies (Fig. 2.4d). To

understand the origin of such a difference in adsorption strength, we further calculated the electron density difference ($\Delta\rho_e$) at the Pt(111)–water interface after introducing different cations. Overall, the interaction between the cation and the OH_{ad} is mostly electrostatic (decays via an inverse square law) and its effect on the electronic structure of the Pt surface is mild. The yellow isosurfaces between the cation and the nearby water molecules show the redistribution of the electron density on water to form the cation–water bonds, where a larger lobe indicates a higher extent of such redistribution (Fig.2.7d-f). The more pronounced electron density redistribution in the presence of Li^+ can be attributed to the stronger local electric field from its higher charge density (that is, the same net charge but with a much smaller ionic radius) compared with Na^+ and K^+. The electric field exerted by the cation also causes redistribution of the electron density in the OH_{ad}, reducing the electron density of the lone pair closest to the cation (region A in each inset) while increasing for the farther lone pair (region B in each inset). It is interesting to note that the region corresponding to the Pt–O bond (region C in each inset) also experiences an increase in electron density, which is due to charge compensation from bulk Pt to the polarized OH_{ad}.

To quantify further such polarization and charge redistribution for OH_{ad}, we performed Bader charge analysis on the interface (Fig. 2.8), and the net charge on O in OH_{ad} is calculated to be $-0.52\ |e|$, $-0.49\ |e|$ and $-0.48\ |e|$ in the presence of Li^+, Na^+ and K^+, respectively. Based on these Bader charges, the dipole moment of the O–H_{ad} (Pt–O) bonds are calculated to be 2.37 D (2.09 D), 2.19 D (1.69 D) and 2.15 D (1.06 D) for Li^+, Na^+ and K^+, respectively (Fig. 2.7c). Hence, it is clear that the extent of charge redistribution and polarization for OH_{ad} both follow the trend of $Li^+ > Na^+ > K^+$, which is probably caused by the stronger electric field of Li^+, analogous to polarization of the first hydration sphere.

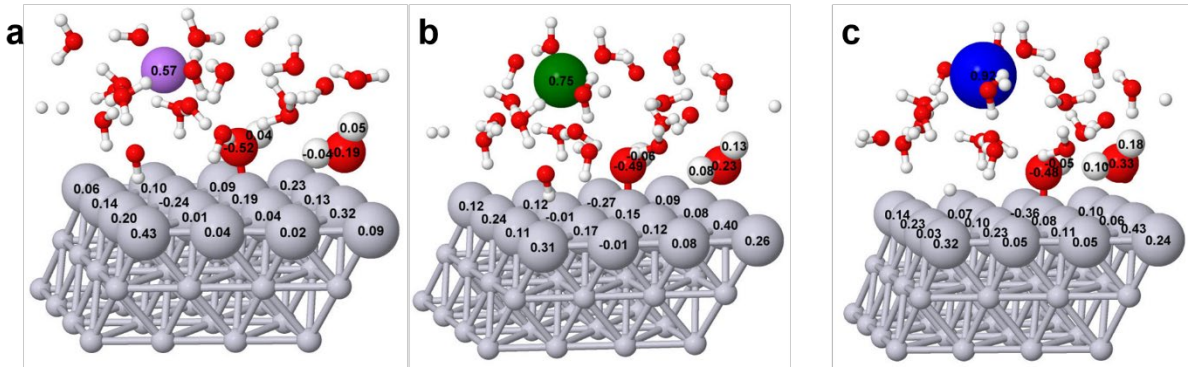

Figure 2.8: Bader charges of the key atoms in Pt(111)-OH_{ad}/water with cations. The geometry of Pt(111)-OH_{ad}/water interface with (a) Li^+, (b) Na^+, (c) K^+, with calculated Bader charge values labeled on each atom. Chemically irrelevant atoms are hidden for clarity.

Since the hydration sphere and water configuration at the Pt–water interface are not static, we further performed AIMD simulations at the Pt(111)–water interface with near-surface hydrated cations in the canonical ensemble at 300 K to account for the dynamics and to better sample the configurational space. A 100 ps trajectory is obtained for each system after pre-equilibration, with a variance of potential energy within 0.15 eV, marking proper equilibration of the system (Fig. 2.9).

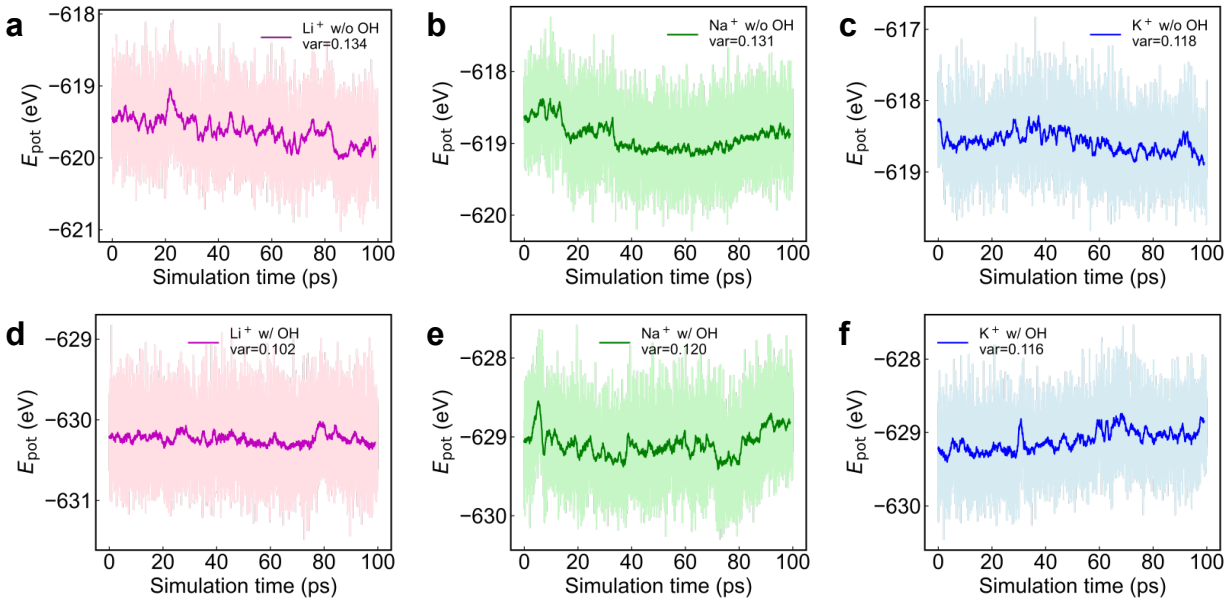

Figure 2.9: Potential energy during the 100-ps AIMD simulations after pre-equilibration. The plot of potential energy versus simulation time of (a-c) Pt(111)/water interface and (d-f) Pt(111)-OH_{ad}/water

interface, with near-surface hydrated cations in the AIMD simulation. The moving average (over 1 ps) is plotted as darker curves, and the variance of potential energy is labeled in each panel.

To test our model, we have performed additional AIMD simulations for Li^+ with a thicker layer of water (~10 Å) or with a larger supercell (6x6, 16.87 Å x 14.61 Å, a size that is considered sufficient for studying interfacial behavior of water[49]. The resulting Li-O RDF and integrated CN from the larger supercell (Fig. 2.10) show that the first and second hydration shell stay about the same after adding more water or enlarging the cell. The peaks of the "thicker water slab" simulation is slightly broader than the other two conditions, which can be attributed to a better convergence to bulky solution behavior on the far end, but with little difference in the coordination number. Hence, we conclude that the originally adopted model in our study can yield meaningful solvation dynamics of near-surface cations.

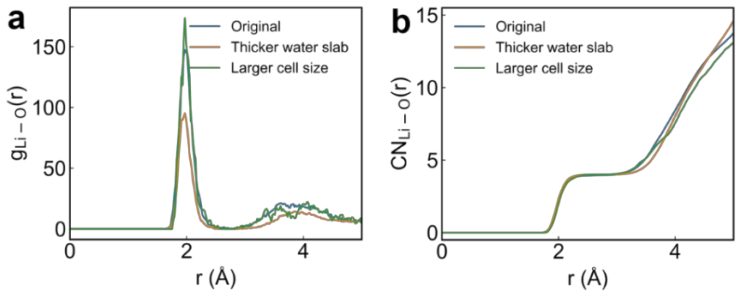

Figure 2.10: Justification of the simulation box size and the water layer thickness. (a) Radial distribution function and (b) integrated coordination numbers of Li-O from equilibrated AIMD simulations using the original model in this work, vs. those with a thicker water slab (~10 Angstroms) or a larger cell size (6x6).

The cation–oxygen radial distribution function (RDF; $g_{cation-O}(r)$) data (Fig. 2.11) obtained from the AIMD trajectory simulations are consistent with the results of large-scale molecular mechanics simulations[50] and test simulations with a larger cell size or thicker water layer, demonstrating the correct hydration structure of the cations.

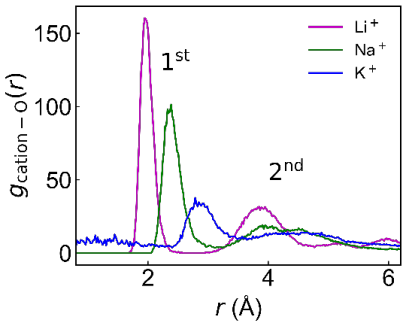

Figure 2.11: Radial distribution function of cation-O. The radial distribution function $g_{\mathrm{cation-O}}(r)$ between O and H atoms in the Pt(111)/water interface in presence of Li^+, Na^+ and K^+ ions, calculated from a 100-ps AIMD trajectory. Earlier peak position suggests shorter cation-O bond length, and sharper peak suggest rigid (or incompressibility) of the hydration sphere.

The adsorption enthalpy (approximated by the molecular dynamics average of potential energy) of OH ($\widetilde{\mathrm{E}}_{\mathrm{ad}}^{\mathrm{OH}}$) is calculated to be −2.71 eV, −2.51 eV and −2.40 eV in the presence of Li^+, Na^+ and K^+, respectively (Fig. 2.7a), which is largely consistent with the trend of $\mathrm{E}_{\mathrm{ad}}^{\mathrm{OH}}$ and potential-dependent $\mathrm{G}_{\mathrm{ad}}^{\mathrm{OH}}$ calculated for static models (Fig. 2.7a,b), further confirming more the favorable OH_{ad} in the presence of Li^+.

The reduction of the adsorption energy (Fig. 2.7a) with increasing AM^+ size (from Li^+ to Na^+ to K^+) is contributed by the interface dynamics. We note it has been a debated topic as to whether the cations adsorb directly or simply accumulate in the outer-Helmholtz plane in the double layer[51-53]. Hence, we further studied the cation dynamics and the hydration structure. The representative snapshots of each system at equilibrium and at the position closest to the surface (Fig. 2.12) show that the cation stays in the double layer most of the time, oscillating between the first and second water layers.

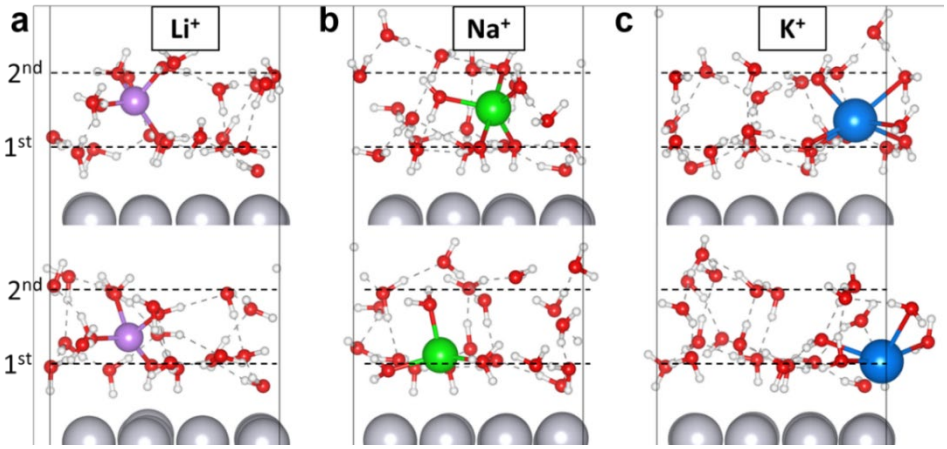

Figure 2.12: AIMD snapshots of the Pt(111)/water interface. The representative snapshots of the Pt(111)/water interface in presence of (a) Li^+, (b) Na^+, and (c) K^+ ions from equilibrated AIMD trajectory. The typical equilibrium configurations are shown on the top row, while the configurations with shortest cation-surface distances are shown on the bottom row. The height of the first and the second water layers are marked by dashed lines.

During the 100 ps AIMD simulations, Li^+ maintains a coordination number (CN) of 4 and oscillates in the upper half between the first and second water layers. The CN fluctuates between 4 and 5 for Na^+ and oscillates in the lower half between the first and second water layers. By contrast, K^+ does not have a specific CN and frequently penetrates the first water layer but never stays specifically adsorbed on the Pt surface. The cation CN values (4 for Li^+, ~4–5 for Na^+ and ~4–6 for K^+) obtained in our simulations are consistent with ref.[54], and the position of the cations is consistent with ref. [53]. The average distance between the cation and the Pt(111) surface for Li^+, Na^+ and K^+ is, respectively, 4.44 Å, 4.42 Å and 3.95 Å without surface OH and 5.38 Å, 4.43 Å and 3.88 Å with surface OH, which is due to the different rigidness of their hydration spheres as also characterized by the sharpness of the RDF peak (Fig. 2.11). Notably, only Li^+ is observed to have a well-defined second hydration sphere, and only K^+ experiences instantaneous penetration of water inside its first hydration shell (Fig. 2.11). The variation in the cation–surface distance partially smears the difference in OH adsorption for different cations, while leaving the overall trend qualitatively unchanged. The distinct interfacial dynamics are attributed to the different

charge density of the cations, the cation–water interaction strength and the mass of the cations (heavier cations are less dragged by the friction of their water environment). It is noted that the observation that the cations do not stay dehydrated and form bonds with the Pt surface contradicts the hypothesis previously proposed in refs.[7, 52, 55, 56], the discrepancy of which is probably the result of undercoordination of the cations through insufficient explicit solvation, which leads to an overestimation of the cation–surface binding strength. We also note that previous studies indicated that large cations (for example, Cs^+) may show a stronger interaction and direct adsorption on the electrode surface due to their less tightly bound solvation shell[46]. Indeed, our preliminary ETS studies also suggested that larger cations (Rb^+ or Cs^+) may directly adsorb on the electrode surface and are expected to influence the HER activity in a very different way. Therefore, we investigated the effect of Rb^+ and Cs^+ ions separately.

2.3.3. Cation modulation of the local chemical environment and HER kinetics

The aforementioned experimental ETS results and theoretical calculations confirm that the AM^+ do not specifically adsorb on the electrode surface but instead accumulate in the outer-Helmholtz plane. To probe the distribution of cations in the outer-Helmholtz plane of the EDL, we performed EIS analyses in different cation electrolytes and determined the double-layer capacitance (C_{dl}) at different applied potentials (Fig. 2.13a). In the simplified equation, the C_{dl} is directly related to the relative permittivity (ε) of the solvent at a constant electrolyte concentration (C), as well as the vacuum permittivity (ε_0), as shown below[57]:

$$C_{dl} = \varepsilon\varepsilon_o\sqrt{C} \qquad (2\text{-}2)$$

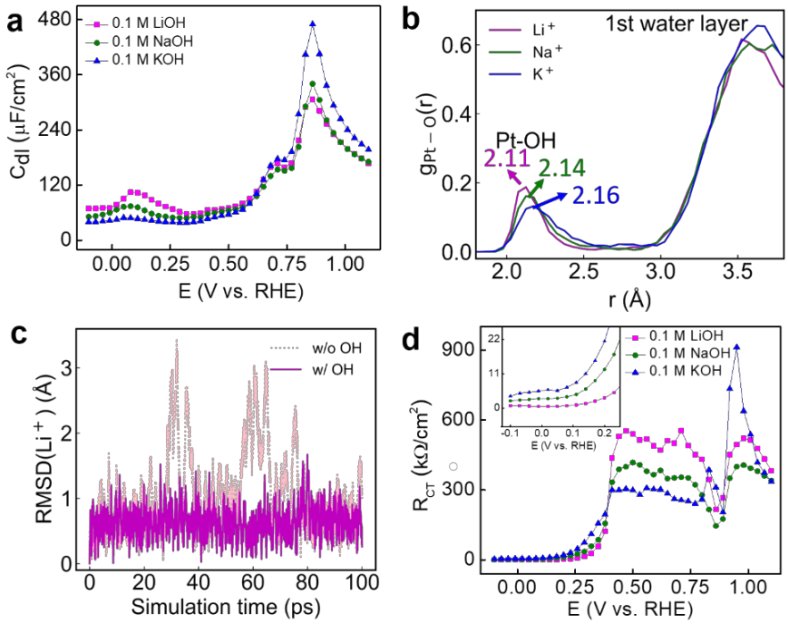

Figure 2.13: EIS and DFT investigation of role of OH_{ad}. (a) Double layer capacitance (C_{dl}) on the Pt disc electrode at different applied potentials in 0.1 M MOH solutions (M= Li, Na and K) (b) The RDF $g_{Pt-O}(r)$ between Pt and O atoms in the Pt(111)-OH_{ad}-water interface in presence of Li^+, Na^+, and K^+ ions calculated from AIMD trajectory. (c) The r.m.s.d. of the position of Li^+, with and without OH_{ad} on the Pt surface, during the 100 ps AIMD simulation. (d) Charge transfer resistance (R_{ct}) on Pt disc electrode at different applied potentials in 0.1 M MOH solutions (M= Li, Na and K).

The EIS studies reveal a larger C_{dl} in the high-potential regime (1.1–0.6 V_{RHE}) for K^+ than for Na^+ and Li^+, which can be attributed to the lower hydration energy, the shorter cation–surface distance and the less rigid hydration sphere (and hence a smaller effective hydration-sphere radius) of K^+ compared with Na^+ and Li^+ (ref.[58]). However, an opposite trend was observed when the potential entered the H_{upd}/HER regime, with a larger C_{dl} shown in the case of Li^+. This reversal in C_{dl} is attributed to the change in the local cation concentration induced by the change in surface species. With the interaction between the hydrated cation and surface OH_{ad} shown in our DFT calculations, we hypothesize that the local cation concentration may be highly dependent on the coverage and polarity of the surface OH_{ad}, and may be substantially different from the bulk concentration.

To explore further how the surface OH_{ad} and near-surface cations influence the dynamic properties of each other, we analyzed the AIMD trajectories of the Pt(111)–water and Pt(111)–OH_{ad}–water

interfaces with near-surface hydrated cations. The first peak in the RDF of Pt–O (Fig. 2.13b) corresponds to the Pt–OH bond, and is the leftmost and the sharpest in the presence of Li^+, followed by Na^+ and K^+, suggesting that the strongest Pt–OH bond is with Li^+, which is consistent with the experimental and theoretical results discussed in the previous sections. The second peak corresponds to the first water layer, which it is about the same distance for the three cations, showing the consistent distribution of near-surface water that is independent of the identity of the hydrated cation.

Interestingly, the polarized OH_{ad} in turn could stabilize the hydrated cation to stay in its surroundings. The root mean squared deviation (r.m.s.d.) of the Li^+ position from the Pt surface shows a considerably larger fluctuation in the absence of OH_{ad} (Fig. 2.13c), suggesting the large and frequent oscillation and the drifting of Li^+ away from its equilibrium position (zero reference). After introducing OH_{ad}, the r.m.s.d. flattens and seldom goes beyond 1.5 Å from the equilibrium position, suggesting the anchoring of Li^+ cations to the Pt surface by OH_{ad}. A similar anchoring effect is also observed for Na^+ and K^+ ions, although to a lesser extent due to the weaker cation–OH interactions (Fig. 2.14).

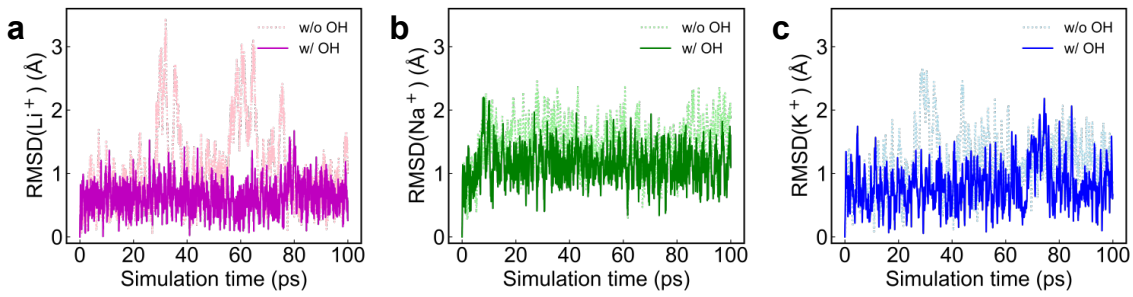

Figure 2.14: RMSD showing the oscillation of cation away from the equilibrium position. The root mean square deviation of the position of (a) Li^+ (b) Na^+ and (c) K^+, with and without OH_{ad} on the Pt surface, during the 100 ps AIMD simulation.

We note that such anchoring differs from the specific adsorption since the cation and OH_{ad} are separated by the first hydration shell (~4 Å apart) without forming any direct cation–OH bond or

OH_{ad}-induced dehydration. Our simulation showed that the AM^+ is not directly bonded to the OH_{ad}, but separated by a water molecule in the first hydration shell. In addition, the AM^+ does not forms direct bond with the Pt surface either. Note that the hydration/dehydration dynamics of the three investigated cations are also different: the hydration shell of Li^+ and Na^+ stays intact throughout, whereas K^+ oscillates between the hydrated state and a partially dehydrated state. The degree of hydration is not affected by the presence of OH_{ad}, which stays beyond the first hydration sphere. This can be illustrated by the evolution of cation-OH distance during the AIMD simulation (Fig. 2.15). The distance equilibrates at around 4 Å, which is well beyond the first hydration shell and suggest no direct bond between cation and OH_{ad}. Hence, the picture proposed by this work differs from that suggested previously by Koper and Janik and provides additional insights into hydration dynamics, although the apparent trend is similar[7, 8].

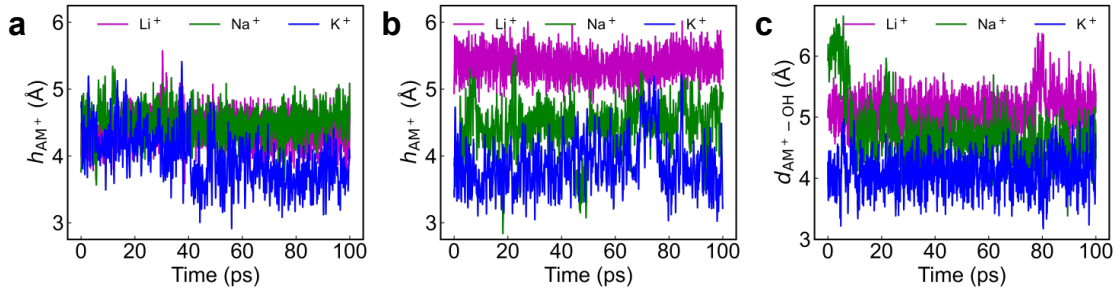

Figure 2.15: Evolution of height and distance of AM cations. Height of AM cations relative to the Pt surface (a) in absence and (b) presence of OH_{ad}. (c) The distance between AM cations and OH_{ad}. All results are obtained from a 100-ps AIMD simulation after pre-equilibration.

Since the OH_{ad} has the highest surface coverage and polarity in the presence of Li^+, followed by Na^+ and K^+, this means more anchors and a stronger anchoring effect, leading to a higher local concentration of cations ($Li^+ > Na^+ > K^+$) near the Pt surface.

To conclude, the crossover of C_{dl} in the EIS results near 0.60 V_{RHE} is induced by the change in the surface coverage of OH_{ad}: (1) at a higher potential (>0.60 V_{RHE}) where there are abundant surface OH_{ad} species, the capacitance ($K^+ > Na^+ > Li^+$) is more determined by the inverse of the cation–

surface distance and the hydration-sphere size; and (2) at a lower potential (<0.60 V_{RHE}) when there is only a limited number of OH_{ad} species, the capacitance ($Li^+ > Na^+ > K^+$) is more dictated by the local cation concentration, which is in turn related to the coverage of remaining OH_{ad} due to its anchoring effect.

The charge-transfer resistance was also determined from the EIS data. The electrode–electrolyte interface was largely capacitive over the entire potential range except for the HER region (Fig. 2.13d). The charge-transfer resistance in the oxidation region (~1 V) is not meaningful as it is largely capacitive with a minimal charge-transfer process. However, in the hydroxyl-desorption potential regime (~0.9–0.4 V_{RHE}), the charge-transfer resistance is larger for Li^+ ions when compared with Na^+ and K^+ ions, suggesting the more difficult desorption of OH_{ad} and replacement by H_2O molecules in the presence of Li^+ ions, which is consistent with our ETS results. By contrast, in the H_{upd} and HER regimes (<0.4 V_{RHE}), the charge-transfer resistance is the lowest for Li^+ ions, followed by Na^+ and K^+ ions, which consistent with the improved Volmer-step kinetics for H_{upd} and HER for Li^+ ions followed by Na^+ and K^+ ions (Fig. 2.2b).

To further understand the HER activity trend, we focused on the behavior of water molecules in the AIMD because water is the major proton source in the alkaline HER. With the alkaline Volmer step (involving water dissociation) being the rate-determining step[13], the O–H bond strength in near-surface water could work as a metric to explain the HER activity. To this end, we examined the RDF of O–H of water with different surrounding species (Fig. 2.16a). Compared with water in the regular bulk water environment, the water O–H bond length in the first hydration shell of the cation experiences a downshift in the peak position and a slight sharpening of the peak, suggesting the strengthening of the O–H bond of water in the hydration shell of the cation. On the other hand, the O–H peak of a water molecule next to both O and H of OH_{ad} show a longer tail on the stretching

side (~1.05–1.1 Å), indicating that OH_{ad} can function as both a proton acceptor and donor to weaken the O–H bond in nearby water, hence leading to a lower barrier for water dissociation.

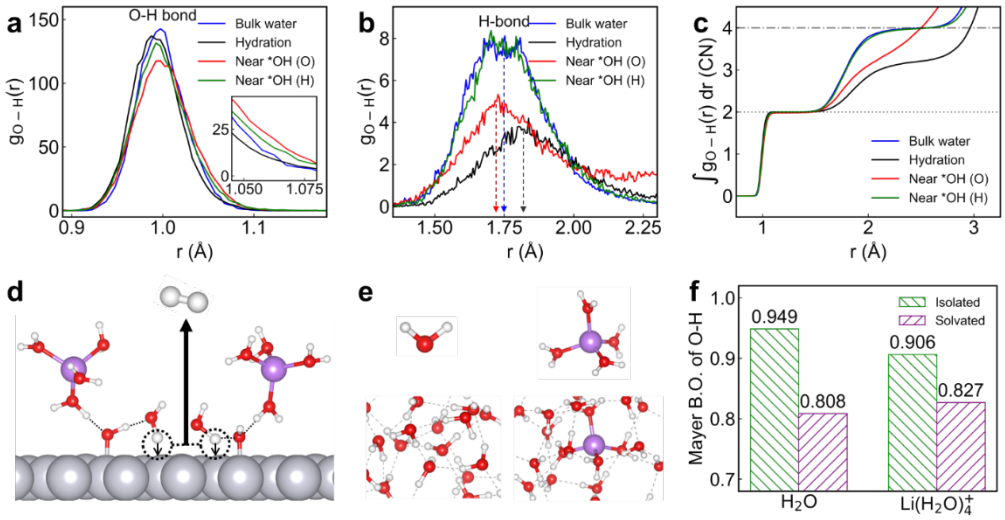

Figure 2.16: AIMD and micro-solvation simulations of cation and OH_{ad}. (a,b) The RDF $g_{O-H}(r)$ between O and H atoms in the Pt(111)-OH_{ad}-water interface in presence of Li^+ in the covalent O-H region (a) and the non-covalent O…H hydrogen bond region (b). The decomposed curves belong to water molecules in the hydration sphere of Li^+, in the bulk water, or near the surface OH_{ad} as its hydrogen bond donor or acceptor. Inset in (a) shows zoomed-in view of the tail region corresponding to O-H stretching. (c) Integrated $g_{O-H}(r)$ showing the coordination number (CN) of O by H at different r(O-H) distances, with dotted and dash-dot lines marking CN=2 and CN=4, respectively. (d) Schematics showing the promotion of alkaline Volmer step by surface OH_{ad} at the Pt(111)-water interface. (e) Optimized geometry of H_2O and $Li(H_2O)_4^+$ in isolated state (top row) or in solvated state (bottom row). (f) Bar chart of the Mayer bond order of O-H in H_2O and $Li(H_2O)_4^+$ in isolated state or in solvated state.

The variation in water reactivity near different species can also be partly explained via the different hydrogen-bond strengths with their environment, which is characterized by the hydrogen-bond peak in the O···H RDF. The earlier and sharper peaks in the $r \approx 1.5$–2.0 Å region (Fig. 2.16b) suggest stronger and more directional hydrogen-bond interactions on the water molecules by its environment. Compared with the bulk water case (peak position at ~1.76 Å), the water in the first hydration shell of the cation has a broader shape and later peak position (~1.80 Å) due to the blockage/restraint of hydrogen-bond formation through the steric arrangement of the cation and the hydration shell. It is interesting to note the water molecules near the O in OH_{ad} show a shorter

hydrogen-bond peak (~1.73 Å), indicating a considerably strengthened hydrogen bond, which fundamentally originates from the highly polar OH_{ad} with a much higher negative charge density on O atoms than that in the near-surface water, as indicated by the Bader charges (−0.52 |*e*| on O in OH_{ad} compared with around −0.2 |*e*| on O in near-surface water) (Fig. 2.8a). These analyses indicate that the OH_{ad} species function as strongly polarized H^+ acceptors for nearby water molecules and thus facilitate water dissociation. The peak area, which corresponds to the CN of O by H (Fig. 2.16c), is smaller than the case of bulk water, probably due to the blockage of hydrogen-bond sites by the steric hindrance of the Pt surface.

The water near the H in OH_{ad} (with OH_{ad} being a hydrogen-bond donor) has a similar peak height/area to that in bulk water (Fig. 2.16b), indicating a similar hydrogen-bond strength. The Bader charge analysis indicates that there is a less positive charge on H in OH_{ad} (0.04 |*e*| for H in OH_{ad} versus ~0.1 |*e*| on H in water), and the surface OH_{ad} is thus an electronically weaker hydrogen-bond donor. On the other hand, the longer tail in the O–H stretching region for water near H in OH_{ad} (Fig. 2.16a inset) indicates that OH_{ad} does function as a proton donor to weaken O–H in nearby water molecules, which is probably due to the synergistic geometric effect of the surface-bound OH_{ad} and near Pt-surface water dynamics.

Together, by combining systematic experimental and theoretical studies, we reveal that the cations play an indirect role in the alkaline HER on Pt. It is the enhanced surface coverage of OH_{ad} that is induced by the presence of smaller cations (Li^+), instead of the cation itself, that enhances the HER activity in alkaline media (Fig. 2.16d). The smaller cations lead to a higher OH_{ad} coverage on the Pt surface in the HER potential window, and the OH_{ad} can act as electronically favored proton acceptors and geometrically favored proton donors to promote water dissociation and the Volmer-

step kinetics in alkaline media. The higher OH_{ad} coverage in the case of Li^+ ions (followed by Na^+ and then K^+) leads to the higher HER activity.

We note in our findings that cations stabilizing their first hydration shell is in stark contrast to the common perception that the cations can directly activate the hydration sphere[55, 59], and hence we performed a sanity check using a finer micro-solvation model at a higher level of theory and evaluated the Mayer bond order of the O–H bonds based on DFT-optimized geometries (Fig. 2.16 e,f). Without explicit solvation, the Mayer bond order of O–H in the hydration shell of Li^+ (0.906) is lower than that of isolated water (0.949), which results from polarization by the electrostatics of the cation. Interestingly, the trend is reversed when the system is subject to explicit solvation. In a hydrogen-bond network, each water molecule is connected to four neighboring water molecules via hydrogen bonds, which causes a significant weakening of the O–H bond in water to result in a Mayer bond order of 0.808. However, each water molecule in the first hydration shell of Li^+ can only connect to two or three neighboring water molecules due to the blockage of hydrogen-bond sites by the steric effect of the cation. The Mayer bond order of the O–H in the hydration shell of the cation (0.827) is therefore weakened to a lesser extent since the effect of the water environment outcompetes the effect of the cations. In other words, the water in the hydration shell of the cation is stabilized compared with the water in bulk water. Hence, the argument that a cation activates its hydration sphere is probably the result of underestimating the role of the water environment. We recognize that the models adopted in this study have certain limitations from various aspects due to computation–cost limitations discussed below and we believe that this example highlights well the necessity of including sufficient explicit solvation to properly describe the reactivity of water in both the bulk solution and at an electrochemical interface:

(i) The water layer thickness adopted in this work, although is sufficient for studying solvation dynamics of the near-surface cations, is not thick enough for converging to bulk solution behavior which requires a water slab thickness of ~10-20 Å. This makes a rigorous free energy calculation difficult due to insufficient solvation of final states (cations or hydroxides solvated in bulk solution region).

(ii) The electrostatic interaction may not be sufficiently screened across neighboring images, especially after considering the size of the whole hydration shell. Hence, the adopted model should represent a condition of relatively high interfacial concentration of cations, and such concentration is assumed to be the same for all three studied cations. In addition, the relatively small size of the simulation cell in xy dimension can lead to spatial correlation between neighboring images. Such correlation, although has been shown in our benchmark to have very little impact on the hydration dynamics, may affect the prediction of diffusion property or vibrational spectra. To eliminate the two sources of artifact, a larger supercell is needed.

(iii) Due to the constant charge nature of the AIMD simulation, the workfunction may vary during the simulation and also among the different cation cases. This can lead to slight inconsistency in water orientation and error in adsorption strengths. To rigorously study the potential dependent interfacial dynamics, one would need a grand canonical treatment (constant potential DFT) which adjust the charge state of the system to align the workfunction with the energy level of an applied electrode potential.

(iv) The affordable timescale of the AIMD simulation with explicit solvation makes it difficult to equilibrate some properties, such as diffusion of solvated cations (especially the heavier ones with weaker AM-water interaction and larger mass). To achieve proper equilibration of such property and ergodicity, one would need a much longer simulation time, which is challenging for DFT but

may be tackled by well parametrized reactive force field or machine learning interatomic potentials.

2.4. Conclusions

In conclusion, we have combined a unique surface-adsorbate specific ETS approach with EIS experiments and DFT calculations to directly probe the on-surface and near-surface chemical environment, deciphering the elusive role of AM^+ on Pt-surface chemistry and the alkaline HER. Our integrated studies suggest that the cation is not directly bonded to the Pt surface or OH_{ad} but is separated by a water molecule in the first hydration shell of the cation, which is distinct from previous studies[7]. Moreover, smaller cations favor a higher OH_{ad} coverage on the Pt surface in the HER potential window, where the OH_{ad} in turn function as electronically favored proton acceptors or geometrically favored proton donors to promote water dissociation and Volmer-step kinetics on the Pt surface in alkaline media, leading to improved HER activity in the presence of smaller cations (Li^+). Our studies resolve the fundamental role of AM^+ in the HER kinetics, which has remained elusive in recent decades, and could offer valuable insights for the design of more efficient electrolysers for renewable energy conversion.

2.5. References

(1) Sheng, W.; Gasteiger, H. A.; Shao-Horn, Y. Hydrogen oxidation and evolution reaction kinetics on platinum: acid vs alkaline electrolytes. *Journal of The Electrochemical Society* **2010**, *157* (11), B1529.

(2) Li, L.; Wang, P.; Shao, Q.; Huang, X. Recent progress in advanced electrocatalyst design for acidic oxygen evolution reaction. *Advanced Materials* **2021**, *33* (50), 2004243.

(3) Gasteiger, H.; Yan, S. Dependence of PEM fuel cell performance on catalyst loading. *Journal of power sources* **2004**, *127* (1-2), 162-171.

(4) Nørskov, J. K.; Bligaard, T.; Logadottir, A.; Kitchin, J.; Chen, J. G.; Pandelov, S.; Stimming, U. Trends in the exchange current for hydrogen evolution. *Journal of The Electrochemical Society* **2005**, *152* (3), J23.

(5) Zhang, W.; Huang, B.; Wang, K.; Yang, W.; Lv, F.; Li, N.; Chao, Y.; Zhou, P.; Yang, Y.; Li, Y. WOx-surface decorated PtNi@ Pt dendritic nanowires as efficient pH-universal hydrogen evolution electrocatalysts. *Advanced Energy Materials* **2021**, *11* (3), 2003192.

(6) Sheng, W.; Myint, M.; Chen, J. G.; Yan, Y. Correlating the hydrogen evolution reaction activity in alkaline electrolytes with the hydrogen binding energy on monometallic surfaces. *Energy & Environmental Science* **2013**, *6* (5), 1509-1512.

(7) Chen, X.; McCrum, I. T.; Schwarz, K. A.; Janik, M. J.; Koper, M. T. Co-adsorption of cations as the cause of the apparent pH dependence of hydrogen adsorption on a stepped platinum single-crystal electrode. *Angewandte Chemie International Edition* **2017**, *56* (47), 15025-15029.

(8) McCrum, I. T.; Chen, X.; Schwarz, K. A.; Janik, M. J.; Koper, M. T. Effect of step density and orientation on the apparent pH dependence of hydrogen and hydroxide adsorption on stepped platinum surfaces. *The Journal of Physical Chemistry C* **2018**, *122* (29), 16756-16764.

(9) Ledezma-Yanez, I.; Wallace, W. D. Z.; Sebastián-Pascual, P.; Climent, V.; Feliu, J. M.; Koper, M. Interfacial water reorganization as a pH-dependent descriptor of the hydrogen evolution rate on platinum electrodes. *Nature Energy* **2017**, *2* (4), 1-7.

(10) Seto, K.; Iannelli, A.; Love, B.; Lipkowski, J. The influence of surface crystallography on the rate of hydrogen evolution at Pt electrodes. *Journal of electroanalytical chemistry and interfacial electrochemistry* **1987**, *226* (1-2), 351-360.

(11) Markovića, N. M.; Sarraf, S. T.; Gasteiger, H. A.; Ross, P. N. Hydrogen electrochemistry on platinum low-index single-crystal surfaces in alkaline solution. *Journal of the Chemical Society, Faraday Transactions* **1996**, *92* (20), 3719-3725.

(12) Marković, N.; Grgur, B.; Ross, P. N. Temperature-dependent hydrogen electrochemistry on platinum low-index single-crystal surfaces in acid solutions. *The Journal of Physical Chemistry B* **1997**, *101* (27), 5405-5413.

(13) Subbaraman, R.; Tripkovic, D.; Strmcnik, D.; Chang, K.-C.; Uchimura, M.; Paulikas, A. P.; Stamenkovic, V.; Markovic, N. M. Enhancing hydrogen evolution activity in water splitting by tailoring Li+-Ni (OH) 2-Pt interfaces. *Science* **2011**, *334* (6060), 1256-1260.

(14) Subbaraman, R.; Tripkovic, D.; Chang, K.-C.; Strmcnik, D.; Paulikas, A. P.; Hirunsit, P.; Chan, M.; Greeley, J.; Stamenkovic, V.; Markovic, N. M. Trends in activity for the water electrolyser reactions on 3 d M (Ni, Co, Fe, Mn) hydr (oxy) oxide catalysts. *Nature materials* **2012**, *11* (6), 550-557.

(15) Li, J.; Ghoshal, S.; Bates, M. K.; Miller, T. E.; Davies, V.; Stavitski, E.; Attenkofer, K.; Mukerjee, S.; Ma, Z. F.; Jia, Q. Experimental proof of the bifunctional mechanism for the hydrogen oxidation in alkaline media. *Angewandte Chemie International Edition* **2017**, *56* (49), 15594-15598.

(16) Liu, E.; Li, J.; Jiao, L.; Doan, H. T. T.; Liu, Z.; Zhao, Z.; Huang, Y.; Abraham, K.; Mukerjee, S.; Jia, Q. Unifying the hydrogen evolution and oxidation reactions kinetics in base by identifying the catalytic roles of hydroxyl-water-cation adducts. *Journal of the American Chemical Society* **2019**, *141* (7), 3232-3239.

(17) Cong, Y.; McCrum, I. T.; Gao, X.; Lv, Y.; Miao, S.; Shao, Z.; Yi, B.; Yu, H.; Janik, M. J.; Song, Y. Uniform Pd 0.33 Ir 0.67 nanoparticles supported on nitrogen-doped carbon with

remarkable activity toward the alkaline hydrogen oxidation reaction. *Journal of Materials Chemistry A* **2019**, *7* (7), 3161-3169.

(18) Qiu, Y.; Xin, L.; Li, Y.; McCrum, I. T.; Guo, F.; Ma, T.; Ren, Y.; Liu, Q.; Zhou, L.; Gu, S. BCC-phased PdCu alloy as a highly active electrocatalyst for hydrogen oxidation in alkaline electrolytes. *Journal of the American Chemical Society* **2018**, *140* (48), 16580-16588.

(19) McCrum, I. T.; Koper, M. T. The role of adsorbed hydroxide in hydrogen evolution reaction kinetics on modified platinum. *Nature Energy* **2020**, *5* (11), 891-899.

(20) Xue, S.; Garlyyev, B.; Watzele, S.; Liang, Y.; Fichtner, J.; Pohl, M. D.; Bandarenka, A. S. Influence of alkali metal cations on the hydrogen evolution reaction activity of Pt, Ir, Au, and Ag electrodes in alkaline electrolytes. *ChemElectroChem* **2018**, *5* (17), 2326-2329.

(21) Monteiro, M. C.; Goyal, A.; Moerland, P.; Koper, M. T. Understanding cation trends for hydrogen evolution on platinum and gold electrodes in alkaline media. *ACS catalysis* **2021**, *11* (23), 14328-14335.

(22) Weber, D.; Janssen, M.; Oezaslan, M. Effect of monovalent cations on the HOR/HER activity for Pt in alkaline environment. *Journal of The Electrochemical Society* **2019**, *166* (2), F66-F73.

(23) Li, M.; Zhao, Z.; Cheng, T.; Fortunelli, A.; Chen, C.-Y.; Yu, R.; Zhang, Q.; Gu, L.; Merinov, B. V.; Lin, Z. Ultrafine jagged platinum nanowires enable ultrahigh mass activity for the oxygen reduction reaction. *Science* **2016**, *354* (6318), 1414-1419.

(24) Ding, M.; He, Q.; Wang, G.; Cheng, H.-C.; Huang, Y.; Duan, X. An on-chip electrical transport spectroscopy approach for in situ monitoring electrochemical interfaces. *Nature Communications* **2015**, *6* (1), 7867.

(25) Adamo, C.; Barone, V. Toward reliable density functional methods without adjustable parameters: The PBE0 model. *The Journal of chemical physics* **1999**, *110* (13), 6158-6170.

(26) Kresse, G.; Joubert, D. From ultrasoft pseudopotentials to the projector augmented-wave method. *Physical review b* **1999**, *59* (3), 1758.

(27) Kresse, G.; Furthmüller, J. Efficiency of ab-initio total energy calculations for metals and semiconductors using a plane-wave basis set. *Computational materials science* **1996**, *6* (1), 15-50.

(28) Kresse, G.; Furthmüller, J. Efficient iterative schemes for ab initio total-energy calculations using a plane-wave basis set. *Physical review B* **1996**, *54* (16), 11169.

(29) Kresse, G.; Hafner, J. Ab initio molecular dynamics for liquid metals. *Physical review B* **1993**, *47* (1), 558.

(30) Kresse, G.; Hafner, J. Ab initio molecular-dynamics simulation of the liquid-metal–amorphous-semiconductor transition in germanium. *Physical Review B* **1994**, *49* (20), 14251.

(31) Grimme, S.; Antony, J.; Ehrlich, S.; Krieg, H. A consistent and accurate ab initio parametrization of density functional dispersion correction (DFT-D) for the 94 elements H-Pu. *The Journal of chemical physics* **2010**, *132* (15).

(32) Yu, M.; Trinkle, D. R. Accurate and efficient algorithm for Bader charge integration. *The Journal of chemical physics* **2011**, *134* (6).

(33) Steinmann, S. N.; Michel, C.; Schwiedernoch, R.; Sautet, P. Impacts of electrode potentials and solvents on the electroreduction of CO 2: a comparison of theoretical approaches. *Physical Chemistry Chemical Physics* **2015**, *17* (21), 13949-13963.

(34) Chalk, S. J. The IUPAC Gold Book Website. **2019**.

(35) Humphrey, W.; Dalke, A.; Schulten, K. VMD: visual molecular dynamics. *Journal of molecular graphics* **1996**, *14* (1), 33-38.

(36) Palascak, M. W.; Shields, G. C. Accurate Experimental Values for the Free Energies of Hydration of H+, OH-, and H3O+. *The Journal of Physical Chemistry A* **2004**, *108* (16), 3692-3694. DOI: 10.1021/jp049914o.

(37) Mahler, J.; Persson, I. A study of the hydration of the alkali metal ions in aqueous solution. *Inorganic chemistry* **2012**, *51* (1), 425-438.

(38) Lu, T. Beijing Kein Research Center for Natural Science. China: 2016.

(39) Becke, A. D. Becke's three parameter hybrid method using the LYP correlation functional. *J. Chem. Phys* **1993**, *98* (492), 5648-5652.

(40) Tirado-Rives, J.; Jorgensen, W. L. Performance of B3LYP density functional methods for a large set of organic molecules. *Journal of chemical theory and computation* **2008**, *4* (2), 297-306.

(41) Schäfer, A.; Huber, C.; Ahlrichs, R. Fully optimized contracted Gaussian basis sets of triple zeta valence quality for atoms Li to Kr. *The Journal of chemical physics* **1994**, *100* (8), 5829-5835.

(42) Frisch, M.; Trucks, G.; Schlegel, H. B.; Scuseria, G.; Robb, M.; Cheeseman, J.; Scalmani, G.; Barone, V.; Petersson, G.; Nakatsuji, H. Gaussian 16. Gaussian, Inc. Wallingford, CT: 2016.

(43) Grimme, S.; Ehrlich, S.; Goerigk, L. Effect of the damping function in dispersion corrected density functional theory. *Journal of computational chemistry* **2011**, *32* (7), 1456-1465.

(44) Lu, T.; Chen, F. Multiwfn: A multifunctional wavefunction analyzer. *Journal of computational chemistry* **2012**, *33* (5), 580-592.

(45) Van Der Niet, M. J.; Garcia-Araez, N.; Hernández, J.; Feliu, J. M.; Koper, M. T. Water dissociation on well-defined platinum surfaces: The electrochemical perspective. *Catalysis today* **2013**, *202*, 105-113.

(46) Huang, B.; Rao, R. R.; You, S.; Hpone Myint, K.; Song, Y.; Wang, Y.; Ding, W.; Giordano, L.; Zhang, Y.; Wang, T. Cation-and pH-dependent hydrogen evolution and oxidation reaction kinetics. *Jacs Au* **2021**, *1* (10), 1674-1687.

(47) Ding, M.; Zhong, G.; Zhao, Z.; Huang, Z.; Li, M.; Shiu, H.-Y.; Liu, Y.; Shakir, I.; Huang, Y.; Duan, X. On-Chip in Situ Monitoring of Competitive Interfacial Anionic Chemisorption as a Descriptor for Oxygen Reduction Kinetics. *ACS Central Science* **2018**, *4* (5), 590-599. DOI: 10.1021/acscentsci.8b00082.

(48) Yoo, H.-W.; Cho, S.-Y.; Jeon, H.-J.; Jung, H.-T. Well-Defined and High Resolution Pt Nanowire Arrays for a High Performance Hydrogen Sensor by a Surface Scattering Phenomenon. *Analytical Chemistry* **2015**, *87* (3), 1480-1484. DOI: 10.1021/ac504367w.

(49) Lan, J.; Rybkin, V. V.; Iannuzzi, M. Ionization of Water as an Effect of Quantum Delocalization at Aqueous Electrode Interfaces. *The Journal of Physical Chemistry Letters* **2020**, *11* (9), 3724-3730. DOI: 10.1021/acs.jpclett.0c01025.

(50) Kiyohara, K.; Minami, R. Hydration and dehydration of monovalent cations near an electrode surface. *The Journal of Chemical Physics* **2018**, *149* (1). DOI: 10.1063/1.5037679 (acccessed 3/6/2024).

(51) Rebollar, L.; Intikhab, S.; Oliveira, N. J.; Yan, Y.; Xu, B.; McCrum, I. T.; Snyder, J. D.; Tang, M. H. "Beyond Adsorption" Descriptors in Hydrogen Electrocatalysis. *ACS Catalysis* **2020**, *10* (24), 14747-14762. DOI: 10.1021/acscatal.0c03801.

(52) Mills, J. N.; McCrum, I. T.; Janik, M. J. Alkali cation specific adsorption onto fcc(111) transition metal electrodes. *Physical Chemistry Chemical Physics* **2014**, *16* (27), 13699-13707, 10.1039/C4CP00760C. DOI: 10.1039/C4CP00760C.

(53) Ringe, S.; Clark, E. L.; Resasco, J.; Walton, A.; Seger, B.; Bell, A. T.; Chan, K. Understanding cation effects in electrochemical CO2 reduction. *Energy & Environmental Science* **2019**, *12* (10), 3001-3014, 10.1039/C9EE01341E. DOI: 10.1039/C9EE01341E.

(54) Mähler, J.; Persson, I. A Study of the Hydration of the Alkali Metal Ions in Aqueous Solution. *Inorganic Chemistry* **2012**, *51* (1), 425-438. DOI: 10.1021/ic2018693.

(55) McCrum, I. T.; Janik, M. J. First Principles Simulations of Cyclic Voltammograms on Stepped Pt(553) and Pt(533) Electrode Surfaces. *ChemElectroChem* **2016**, *3* (10), 1609-1617. DOI: https://doi.org/10.1002/celc.201600293.

(56) McCrum, I. T.; Janik, M. J. pH and Alkali Cation Effects on the Pt Cyclic Voltammogram Explained Using Density Functional Theory. *The Journal of Physical Chemistry C* **2016**, *120* (1), 457-471. DOI: 10.1021/acs.jpcc.5b10979.

(57) Lust, E. Electrical Double Layers. Double Layers at Single-crystal and Polycrystalline Electrodes. In *Encyclopedia of Electrochemistry*.

(58) Garlyyev, B.; Xue, S.; Watzele, S.; Scieszka, D.; Bandarenka, A. S. Influence of the Nature of the Alkali Metal Cations on the Electrical Double-Layer Capacitance of Model Pt(111) and Au(111) Electrodes. *The Journal of Physical Chemistry Letters* **2018**, *9* (8), 1927-1930. DOI: 10.1021/acs.jpclett.8b00610.

(59) Goyal, A.; Koper, M. T. M. Understanding the role of mass transport in tuning the hydrogen evolution kinetics on gold in alkaline media. *The Journal of Chemical Physics* **2021**, *155* (13). DOI: 10.1063/5.0064330 (acccessed 3/6/2024).

CHAPTER 3

Specific adsorption of weakly hydrated alkali metal cations on platinum and the anomalous effect of Rb^+ on hydrogen evolution reaction

3.1. Introduction

The hydrogen evolution reaction (HER) is one of the most fundamental reactions for water electrolysis, an essential strategy for renewable energy conversion and storage. Platinum (Pt) represents the most common electrocatalyst for HER[1-3]. Considerable efforts have been invested in understanding this critical reaction[3-5]. The cathodic HER on Pt-based electrodes typically exhibits far more sluggish kinetics in alkaline electrolytes than that in acidic electrolytes, while the anodic oxygen evolution reaction (OER) is generally much more facile in alkaline media. Thus, to understand the underlying factors responsible for the sluggish HER kinetics in alkaline electrolytes is a topic of both fundamental interest and technological significance for alkaline electrolysers.

Alkaline media has a more complex electrolyte environment than acidic one with many more competing surface adsorbates (e.g., different alkali metal cations, hydroxyl anions) that may modify the interfacial molecular structures and reaction pathways, which has been a topic of considerable debate. In particular, alkali metal cations (AM^+) can be present in the immediate surroundings or behave as competitive adsorbates to protons and hydronium ions at the catalytic interface in the HER potential window to fundamentally modify the reaction kinetics. Thus, to fully understand the role of AM^+ in HER, it is essential to investigate their distribution in the electric double layer (EDL) and/or on the electrode surface in the reaction conditions.

A number of recent studies have attempted to resolve the role of AM^+ on the HER activity of the Pt surface, with various hypotheses suggested[5-11]. Bandarenka *et al.* studied the HER activity on the Pt surface in alkaline media with various choices of cations (Li^+, Na^+, K^+, Rb^+, and Cs^+), and concluded that the weakly hydrated larger cations (Rb^+ or Cs^+) are detrimental to the reaction activity, which was tentatively attributed to resulting increase in hydrogen binding energy (HBE)[10]. On the other hand, Koper *et al.* argued that the HBE derived from the hydrogen underpotential deposition (H_{upd}) can't serve as an unambiguous descriptor for HER activity on the Pt surface since the H_{upd} region in alkaline media involves complex changes in hydrogen-cation-hydroxyl behavior[3,8], and proposed that weakly hydrated cations in alkaline media could accumulate at the outer Helmholtz plane and inhibit HER[8]. Jia and coworkers proposed that smaller AM^+ stabilize the presence of OH_{ad}-$(H_2O)_x$-AM^+ in the double-layer region that facilitates the removal of OH_{ad} into the bulk and promotes HER[9]. Huang *et al.* suggested that the smaller cations (such as Li^+ ions) feature a water structure-making tendency that can induce higher HER activity[5], while the larger cations (e.g., Cs^+) have a structure-breaking tendency at the electrified interface, which leads to a higher static dielectric constant at the interface, greater reorganization energy and higher entropic barrier for water dissociation and hydrogen adsorption[5].

These distinct observations and interpretations suggest that the cations may intricately modify interfacial water structure, and fundamentally alter the HER activity. Although a consistent HER activity trend has been observed on Pt: 0.1 M LiOH > 0.1 M NaOH > 0.1 M KOH > 0.1 M CsOH in a number of studies[12-16], it is intriguing that RbOH electrolyte is rarely included in such studies, suggesting possible anomalies. To the best of our knowledge, to date, there are only two studies that included RbOH, which reported an activity trend following the size of the AM^+ series[5, 10]. However, our studies reveal an anomalous HER activity trend with the HER in 0.1 M RbOH

showing the lowest activity (i.e., 0.1 M KOH > 0.1 M RbOH < 0.1 M CsOH), which is at odds with these previous studies[5,10], but may explain the lack of RbOH data in most studies. Additionally, we note that one previous study on the Ir(111) electrode surface reported a similar anomalous effect of lowest HER activity in 0.1 RbOH, but without any explanation[10].

It has also been suggested that the AM^+ can specifically adsorb to metal electrode surfaces at lower (HER) potentials, and these specific interactions could fundamentally impact the rates of electrochemical reactions at the electrified interface[3,16,17]. Previous simulations suggested that larger AM^+ (e.g., Cs^+) show a greater tendency to accumulate at the electrochemical interface[5,8,12]. However, to date, there is no direct experimental evidence substantiating the specific (direct) adsorption of AM^+ on the Pt electrodes. Therefore, it remains unclear whether these effects occur due to specific cation adsorptions or longer-range interactions from nonspecific adsorptions in the EDL. The physical origin of cation-dependent HER kinetics thus remains a topic of vigorous debate.

The fundamental origin of such HER activity evolution is intriguing and could be attributed to the complex interactions of different AM^+ with water molecules and the Pt surface: (i) smaller AM^+ (Li^+, Na^+, and K^+) that do not specifically adsorb on the electrode surface, and are separated from the Pt surface by at least one water molecule layer in the first hydration shell of the AM^+ (ref.[18]), and (ii) the larger weakly hydrated AM^+ i.e. Rb^+ and Cs^+ ions that show quasi-specific and specific adsorption respectively. Our recent studies confirmed that the smaller cations (Li^+, Na^+ and K^+) play an indirect role in modifying surface hydroxyls that are critical for the water dissociation step in alkaline HER process[18].

Herein, we aim to resolve the role of the weakly hydrated AM^+ (i.e., Rb^+ and Cs^+) that could quasi-specifically and specifically adsorb onto the electrode surface. We employ the recently

developed electrical transport spectroscopy (ETS) approach to directly probe the Pt-surface adsorbates at variable potentials and use electrochemical impedance spectroscopy (EIS) to probe EDL and investigate the local environment near the electrode surface. Our ETS and EIS studies reveal that the Rb^+ cations quasi-specifically adsorb on the Pt surface and Cs^+ cations specifically adsorb on the Pt surface. Our computational results further confirm our hypothesis and show that Rb^+ both specifically adsorb on the Pt surface and accumulate in EDL, whereas Cs^+ tend to specifically adsorb on the surface. The anomalously lower HER activity in the presence of Rb^+ is attributed to its quasi-specific adsorption (partial de-solvation) and accumulation in the EDL that blocks water or hydroxyl anion transport and suppresses HER activity. Our combined experimental and computational studies for the first time experimentally confirm the quasi-specific adsorption of Rb^+ and specific adsorption of Cs^+ cations on the Pt surface and provide an unprecedented molecular-level understanding of the intricate role of electrolyte composition in modifying the electrochemical reaction kinetics.

3.2. Experimental details

3.2.1. Chemicals

Lithium hydroxide (LiOH; >98%), sodium hydroxide (NaOH; 98%), Potassium hydroxide (KOH, 87.4%), Rubidium hydroxide (RbOH, 99.9%) and Cesium hydroxide (CsOH, 99.9%) were all purchased from Thermo Fisher Scientific. All aqueous solutions were prepared using deionized (DI) water (18.2 MΩ·cm) obtained from an ultrapure purification system (Aqua Solutions).

3.2.2. Electrochemical Measurements

All of the electrochemical measurements were performed using typical three electrode setup. Platinum rotating disk was used as working electrode, Pt wire and Hg/HgO were used as the

counter and reference electrodes, respectively. All of the potentials reported are versus reversible hydrogen electrode (RHE), calibrated in the same electrolyte by measuring the potential of the HOR/HER currents at zero corresponding to 0 V versus RHE (V_{RHE}).

3.2.3. Impedance measurements

The impedance spectra were measured using frequencies from 10^5 to 1 Hz with an amplitude of 10 mV_{rms} at different applied voltages. Equivalent circuits were fitted to the data using AfterMath software version 1.6.10513.

3.2.4. Synthesis of Pt nanowires (PtNWs)

The PtNWs for the ETS measurements were synthesized following a previously reported protocol[19]. Briefly, $Pt(acac)_2$ (ac = acetylacetonate) (20 mg), $Ni(acac)_2$ (30 mg), $W(CO)_6$ (1.6 mg), glucose (135 mg) and 60 mg of polyvinylpyrrolidone (MW 40,000) were dissolved in 1-octadecene (2 ml) and oleylamine (3 ml). After sonicating for 15 min, the solution was sealed with argon. The mixture was then heated to 140 °C for 4 h. The product was centrifuged with ethanol for 15 min, followed by cyclohexane for 20 min. Finally, the product was centrifuged in a mixture of cyclohexane (5 ml) and ethanol (15 ml) for 20 min. The final product was dispersed in ethanol for device preparation.

3.2.5. Preparation of PtNW films

A free standing PtNW film was assembled on chip from as-prepared PtNW suspension by a co-solvent evaporation method[20]. Briefly, PtNW suspensions in ethanol (400 µl, 0.4 mg ml^{-1}) was added dropwise into a beaker (about 9 cm in diameter) filled with DI water. A thin film of PtNWs from top of water surface was then transferred onto the device.

3.2.6. Fabrication of the PtNW electrochemical device

The device fabrication was followed by the similar approach as previously reported by our group[20]. Typically, a PMMA (A8, MicroChem Corp.) film was prepared by spin coating on the substrate (p++ silicon wafer with 300 nm thermal oxide) surface with pre-patterned Au electrodes (Ti/Au, 10/50 nm). E-beam lithography was then used to open windows on PMMA, which created desired patterns on the substrate. After the removal of PMMA template, PtNWs was deposited on the device substrate with desired patterns. To rule out the influence of electrolyte and to avoid electrochemical reactions on the Au electrodes, another layer of PMMA (~500-nm thick, electrochemically inert) was then deposited on the PtNW device with spin coating. A smaller window that only exposes PtNWs was opened by e-beam lithography. The device was finally used for in-device electrochemistry and *in situ* electrical transport spectroscopy measurement.

3.2.7. In-device CV and in situ ETS

A two channel SMU (Agilent B2902a) was used for the measurement. The first SMU channel was used as a potentiostat to control the potential of source electrode as to the reference electrode (V_G), while collecting the current (I_G) through the counter electrode with a scan rate of 50 mV/sec. The SR830 Lock-In Amplifiers from Stanford research system was used to supply a small sinusoidal current (10 μA) between source and drain electrodes and collecting the corresponding voltage (V_{SD}). Source drain voltage (V_{SD}) was then used to measure the conductance.

The electrical conductivity of the metallic PtNWs is sensitive to surface environment, due to surface scattering of the conduction electrons, producing a resistance change[20]. It is important to note such surface scattering is exclusively sensitive to surface adsorbates, with little impact for the electrostatic or electrochemical potential. For example, previous studies have clearly shown a

constant conductance at different electrochemical potentials when there is a stable surface adsorbate layer (*e.g.*, CO or I^-) that does not change with potential[20, 21], clearly demonstrating the insensitivity of the metallic PtNWs to the varying electrochemical potentials. Thus, the ETS approach offers a unique signal transduction pathway to exclusively probe the surface adsorbates, with minimum interferences from the electrochemical potentials or the bulk electrolyte environment, which is difficult to achieve with other analytic approaches that are often convoluted with near surface (e.g., EDL) or bulk electrolyte background. The close comparison of the ETS measurement with the corresponding CV curve, when the potential is gradually changed from 1.10 – 0.05 V *vs.* RHE is previously reported by our group[18, 22].

3.3. Computational Methods

Constant-charge (+1 on cation) ab initio molecular dynamics (AIMD) simulations were performed using Vienna Ab-initio Simulation Package (VASP) version 5.4.4[23-26], PBE functional[27, 28], with projector-augmented-wave pseudopotentials[29], using a KE cutoff of 400 eV, Grimme's D3 dispersion correction[30], and convergence criteria of $10e^{-5}$ eV and 0.02 eV/$Å^{-1}$, with the Nose-Hoover thermostat in the NVT (canonical) ensemble, with a time step of 1fs on a 3-layer 5×5 Pt (100) surface with dimensions 13.859×13.859 Å. The bottom two layers were fixed to bulk positions. A total of 55 water molecules, number estimated from the density of a previous work[18] were randomly placed above the surface, along with K^+, Rb^+ or Cs^+ placed either close to the support, or within the water layer. A vacuum gap of 18 Å along the z axis was added to avoid interactions between the water and the bottom of the Pt support. A short (1500 fs) AIMD simulation was run to equilibrate the systems. The simulations resulted in both adsorbate-free surfaces, as well as ones with varying coverages of adsorbed H and OH; the simulations containing K^+ and Cs^+ resulted in far more adsorbates than Rb^+. Taking a simulation with no adsorbates, one

water molecule close to the support was then manually split, placing OH on the support, and putting the remaining proton in the water away from the surface. 3 trajectories were run for each cation type and location, each on for 30000 steps. The cation starting locations and adsorbed OH were the same for all trajectories with the cation on the surface or in the water layer. The first 500 steps of each simulation were discarded, and the remaining 75ps of simulation were used for analysis. RDF analysis was performed with vasppy (https://github.com/bjmorgan/vasppy).

3.4. Results and discussion

3.4.1. Cation-dependent HER activity

We have first compared the HER polarization curves obtained on polycrystalline Pt disc electrode in 0.1 M LiOH, NaOH, KOH, RbOH, and CsOH electrolytes (Fig. 3.1a). Our studies showed that the HER overpotential values (at -5 mA/cm^2) generally increase with increasing AM^+ size, although the electrolyte with Rb^+ shows the highest overpotential despite its intermediate size (Fig. 3.1b). The corresponding Tafel slope analysis also showed the largest Tafel slope for the electrolyte with Rb^+ (Fig. 3.1c), confirming the most sluggish HER kinetics in the presence of Rb^+ cations. Our previous studies revealed that the smaller AM^+ (Li^+, Na^+, and K^+) don't specifically adsorb on the Pt surface but favor a higher coverage of hydroxyl adsorbates that could facilitate the water dissociation step to promote HER[18]. Here we focus on the weakly hydrated AM^+ (i.e., Rb^+ and Cs^+, with K^+ also included as a reference) that may specifically adsorb on the Pt electrode surface and attempt to understand the anomalous role of Rb^+ in modifying HER kinetics.

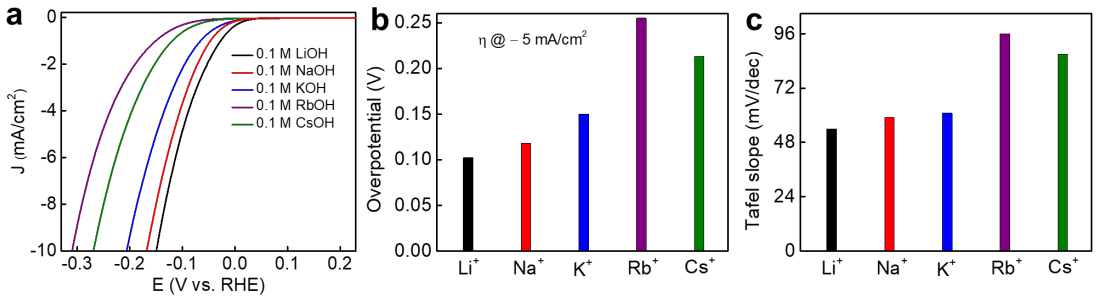

Figure 3.1: Voltammetric studies in electrolytes with different AM^+ cations. (a) The IR-corrected HER polarization curves collected at room temperature on polycrystalline Pt disc electrode in N_2-saturated 0.1 M MOH electrolytes with different AM^+ (Li^+, Na^+, K^+, Rb^+ and Cs^+) at a scan rate of 5 mV/sec and a rotation speed of 1600 rpm. (b) Comparison of the overpotential values at a current density of –5 mA/cm^2 for different AM^+. (c) Comparison of the Tafel slopes in 0.1 M MOH with different AM^+ (Li^+, Na^+, K^+, Rb^+, and Cs^+).

3.4.2. Cation-dependent surface adsorbates

To assess the effects of cations on electrocatalytic reactions, it is essential to understand their distributions on the electrode surface and in the electric double layer. We first employed the recently developed electrical transport spectroscopy (ETS) to directly probe the surface adsorbates during HER. The working principle of the ETS approach was detailed in our previous reports[18, 20-22]. Briefly, the ETS involves a concurrent measurement of conductance change of Pt nanowires (PtNWs) (used as a model catalyst) during electrochemical studies at different electrochemical potentials (Fig. 3.2a). The electrical conductivity of the ultrafine metallic PtNWs is highly sensitive to the surface adsorbates due to surface adsorbate induced scattering of the conduction electrons, producing a resistance change following Equation 3-1 (ref.[17]):

$$\rho = \rho_0 \left(\left(\frac{1-p}{1+p} \right) \times \frac{\lambda}{d} \right) \quad (d \ll \lambda) \qquad (3\text{-}1)$$

Here ρ and ρ_0 are the resistivity of the one-dimensional PtNWs and bulk metal respectively, λ is the electron mean free path, d is the diameter of the PtNWs, and p is a specularity parameter with a value between 0 (for highly diffusive scattering) to 1 (for completely specular scattering)[31].

Additionally, due to the metallic nature of the PtNWs, the electrostatic or electrochemical potential has little impact on the resistance (or conductance). Thus, the PtNW conductance is exclusively sensitive to surface adsorbates but not to the near-surface species. Indeed, previous studies have shown a constant conductance at different electrochemical potentials when there is a stable surface adsorbate layer (e.g., CO or I^-), clearly demonstrating the insensitivity of the PtNWs to the varying electrochemical potentials[20, 21].

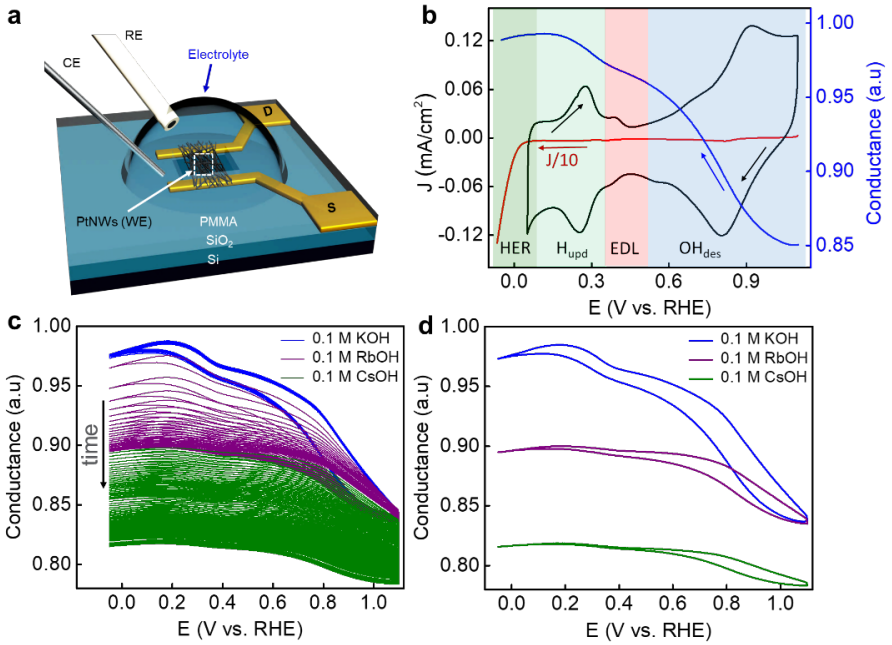

Figure 3.2: Schematic illustration and ETS measurements on Pt electrode in electrolytes with different AM^+ (K^+, Rb^+ and Cs^+). (a) On-chip PtNW device for ETS measurements [RE, CE and PtNWs (WE) are reference, counter and Pt nanowires working electrodes, respectively, S and D represents source and drain, respectively]. Adapted from ref.[21]; (b) Typical cyclic voltammogram (black), negative sweeping branch to the HER region (red) and ETS spectrum (blue). The red curve is divided by 10 due to the much larger HER current in the HER potential window. The hydroxyl desorption (OH_{des}), EDL, H_{upd} and HER regions are highlighted with different background colors (adapted from ref.[18]), (c) Normalized ETS conductance signal versus potential of PtNWs device in 0.1 M MOH electrolytes with different AM^+ at scan rate of 50 mV/sec (K^+ ions show stable conductance curve due to little specific adsorption, while Rb^+ and Cs^+ ions show decreasing conductance over time due to increasing specific adsorption until reaching a stabilized state; and (d) Stabilized conductance curves.

A close comparison of the ETS curve with the cyclic voltammetric curve shows that there are four distinct regions in the potential range from 1.10 V to – 0.05 V *vs.* reversible hydrogen

electrode (RHE) (Fig. 3.2b): (i) surface oxidation and OH adsorption (Ox/OH_{ad}) region (1.10 – 0.60 V vs. RHE); (ii) electrical double layer region (OH_{ad} replaced by H_2O) (0.60 – 0.40 V vs. RHE); (iii) hydrogen underpotential deposition region (H_{upd}) regime (0.40 – 0.08 V vs. RHE); and (iv) HER regime (0.08 - –0.05 V vs. RHE). The lowest conductance observed in the high potential regime is attributed to the larger scattering effect from the strongly bonded OH_{ad} on the Pt surface, which substantially reduces the conductance of the PtNWs. Scanning the potential towards a negative potential regime leads to a notable increase in conductance due to the gradual replacement of the OH_{ad} by H_2O in the OH_{ad} desorption region and then by H_{ad} adsorption in the H_{upd}/HER region.

Our ETS results reveal a notable difference among the three different AM^+. The ETS in 0.1 M KOH show rather stable behavior with overlapping conductance curves during the repeated cycles, while the ETS conductance curves obtained in 0.1 M RbOH and CsOH show a gradual decreasing conductance with increasing scanning cycles (Fig. 3.2c) until they reach a stabilized state (Fig. 3.2d). Comparing the stabilized ETS curves observed in 0.1 M RbOH and CsOH with that in 0.1 M KOH, the ETS from the same device show lower conductance and less conductance modulation over the entire potential range. The more flattened ETS characteristics in the Cs^+ are similar to previous studies in electrolytes with a more stable surface adsorbate layer (e.g., CO or I^-)[20,21], suggesting that Cs^+ specifically adsorbs on PtNW surface and partly blocks the electrochemically active sites from the electrochemical transformation (i.e., surface oxidation, OH adsorption, and H-adsorption).

The conductance curve in the case of Rb^+ is less flat than that of Cs^+, indicating a smaller degree of specific adsorption (i.e., quasi-specific adsorption) of Rb^+ (than Cs^+) on the Pt electrode surface, which is not surprising considering the smaller size of Rb^+ with a slightly stronger

hydration shell than Cs^+. The specific adsorption of large cations causes a more severe scattering effect on the conduction electrons and thus lowers the overall conductance[21]. The quasi-specific adsorption of Rb^+ and specific adsorption of Cs^+ is also consistent with the lower overall ETS conductance compared with that of K^+, which does not show specific adsorption.

It is also noted that in the case of Rb^+, the ETS conductance at high potential (e.g., > 1V vs. RHE) is the same as that of K^+, indicating surface adsorbates in this potential regime are essentially the same as those of electrolyte with K^+ and dominated by surface hydroxyls with little direct impact (specific adsorption) of Rb^+ in this potential regime. On the other hand, in the case of Cs^+, the ETS conductance is considerably lower than that in K^+ or Rb^+ throughout the entire potential regime, indicating that specific adsorption of Cs^+ persists throughout the entire potential window, which is consistent with its higher specific adsorption trend due to its larger size and weaker hydration sphere. Such a specific adsorption of Rb^+ and Cs^+ cations on Pt surfaces has been proposed previously[5,8,12,32], although there is no direct experimental evidence to date, to the best of our knowledge. Thus, our study, for the first time, provides direct evidence supporting the quasi-specific and specific adsorption of large AM^+.

3.4.3. Cation-dependent electrical double layer

We note that ETS only provides information on on-surface (specific) adsorbates and is not sensitive to near-surface species. To further investigate the distribution and concentration of cations in the electrical double layer (EDL), we have performed electrochemical impedance spectroscopy (EIS). The EIS studies reveal that the electrolyte with Rb^+ shows substantially larger C_{dl}, followed by Cs^+ and K^+ (Fig. 3.3a).

At the macroscopic level, the double layer capacitance (C_{dl}) can be expressed as:[33]

$$C_{\mathrm{dl}} = \frac{\varepsilon \varepsilon_o A}{d} \qquad (3\text{-}2)$$

Where ε is the relative permittivity of the solvent, ε_o is dielectric permittivity of vacuum, A is the electrode area, and d is the double layer thickness, which is inversely proportional to the square root of the electrolyte concentration (C) as shown in Equation 2-3 (ref.[18]).

$$\mathrm{d} \propto \frac{1}{\sqrt{C}} \qquad (2\text{-}3)$$

The larger C_{dl} in the case of Rb^+ suggests a smaller double layer thickness and a greater local concentration (C) of Rb^+ in the EDL compared to Cs^+ or K^+ (Fig. 3.3a).

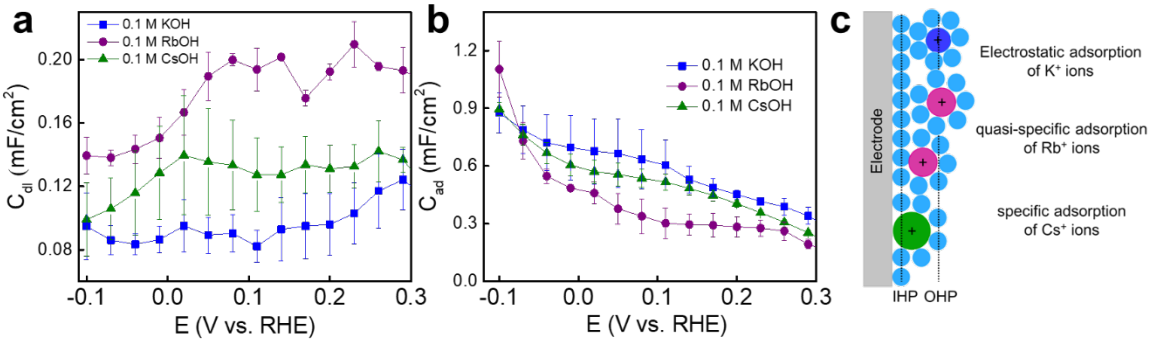

Figure 3.3: EIS studies of the Pt electrode in electrolytes with different AM^+ (K^+, Rb^+ and Cs^+). (a) Double layer capacitance (C_{dl}), (b) pseudocapacitance (C_{ad}) obtained from Pt disc electrode 0.1 M KOH, 0.1 M RbOH and 0.1 M CsOH. (c) Schematic view of electrostatic adsorption of K^+ ions (dark blue circle) and Rb^+ ions (purple circle) residing at the outer Helmholtz plane (OHP) separated by hydration sphere and water molecules (blue circles); quasi-specific adsorption of Rb^+ ions describe the partial de-solvation and separation of the cation adsorption by water molecules on the surface. These cations do not directly interact with the electrode. Specifically adsorbed Cs^+ cations (green circle) residing at the inner Helmholtz plane (IHP), which are chemically bonded to the surface and partially or completely discharged.

Considering the hydration energy of AM^+ ions and the size of hydrated cations that follows the order of $K^+ > Rb^+ > Cs^+$, it is natural to expect the double layer capacitance to follow the order of $K^+ < Rb^+ < Cs^+$ (ref.[34,35]) since the smaller hydrated cations tend to accumulate more on the interface. However, in the HER potential regime in alkaline media, the electrode potential is far below the potential of zero free charge (pzfc)[36], the surface is highly polarized (negatively charged), and thus the weakly hydrated cations (Rb^+ and Cs^+) could partly or completely de-solvate

and specifically adsorb on the inner Helmholtz plane (IHP) (Fig. 3.3c), which could substantially modify the C_{dl}.

Our ETS studies above indicate that K^+ shows no de-solvation, while Rb^+ and Cs^+ show an increasing trend of de-solvation and specific adsorption (Fig. 3.2b). A partial de-solvation of Rb^+ reduces effective cation size and results in an accumulation of Rb^+ in EDL and thus an increase in the double layer capacitance C_{dl}. The accumulation of Rb^+ in EDL results in a more compact cation layer at the interface, which could retard water or hydroxyl anion transport and suppress the HER activity, to be further discussed later. The immediate effect of Rb^+ accumulation can be seen in the observed pseudocapacitance (C_{ad}) resulting from H-adsorption that is the lowest in the presence of Rb^+ compared to K^+ and Cs^+ (Fig. 3.3b). This finding implies that the process of water dissociation and subsequent formation of H_{ad} is more favorable in the presence of K^+ ions within the electrolyte, followed by Cs^+ and Rb^+ ions. Notably, this trend aligns well with the observed HER activity. Sweeping the electrode potential towards a more negative regime further partially de-solvates Rb^+, leading to an increasing accumulation of the Rb^+ in EDL and a continued increase in C_{dl} with decreasing potential (Fig. 3.3a). On the other hand, a complete de-solvation in case of Cs^+ leads to specific adsorption (chemisorption) on the Pt surface with full or partial charge transfer between the electrode and adsorbed Cs^+, i.e., the ionic charge is reduced in the process of specific adsorption, as shown in Equation 3-4 (ref.[37]).

$$Cs(H_2O)_m^{z+} + n\,{}^*(H_2O) + \delta e^- \leftrightarrow Cs(H_2O)_{m-x}^{(z-\delta)+} + (n+x)\,(H_2O) \qquad (3\text{-}4)$$

where $Cs(H_2O)_z^{m+}$ and $^*H_2O$ represent the hydrated Cs^+ cation and surface adsorbed water, respectively; δe^- represents the partial electron transfer from the electrode to the cation. Moreover, as the Cs^+ prefers to specifically adsorb on the surface, it doesn't accumulate in EDL (as confirmed by C_{dl} measurement) that could block water or hydroxyl anion transport and thus retains a

relatively larger pseudocapacitance (hydrogen adsorption). The hydrogen adsorption and charge transfer from the electrode to Cs^+ result in the charge dissipation of the Pt electrode and thus the lowest C_{dl} in the case of Cs^+.

3.4.4. AIMD simulations reveal cation-dependent adsorption behavior and water structuring at the Pt-water interface

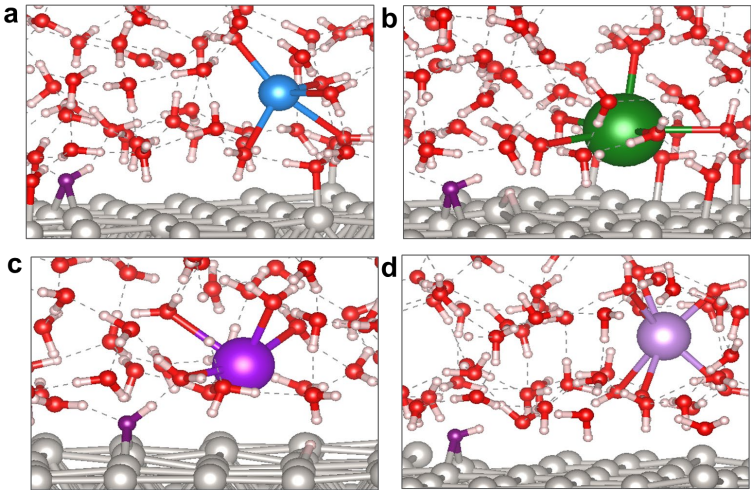

Figure 3.4. AIMD simulations reveal cation behavior on the Pt(100)-water interface. Snapshots of the simulations for (a) K^+_w (b) Cs^+_s (c) Rb^+_s and (d) Rb^+_w, with OH_{ad} on the surface, are shown in purple.

In general, the weakly hydrated cations could suppress the HER activity by: (i) reducing the availability of free surface sites (due to specific adsorption on electrode surface); or (ii) limiting the access of water to the reaction interface (forming dense cation layer in EDL). Here, we further employ AIMD studies to probe these effects at the molecular level. First, we investigated where cations preferentially aggregate relative to the surface and how they affect the structure of near-surface water. AIMD simulations show that K^+ preferentially reside in the EDL, with at least one water layer separating them from the Pt surface (Fig. 3.4a), while Cs^+ tend to be located directly on the Pt surface with no water molecules in-between (i.e., specific adsorption) (Fig. 3.4b). In contrast, Rb^+ ions can reside both on the Pt surface (denoted Rb^+_s) (Fig. 3.4c) and within the EDL

(denoted Rb^{+}_{w}) (Fig. 3.4d). Clearly, as cation size increases, the solvation shell is looser,[38] leading to a partial de-solvation at the electrified interface, with Cs^+ being the easiest to de-solvate and specifically adsorb on the Pt surface, K^+ being the more difficult one, and Rb^+ being the intermediate one. These results agree well with the ETS studies that reveal an increasing tendency for specific adsorption on the Pt surface with increased cation size. On the other hand, although the lowered HER activity for Cs^+ compared to K^+ can be attributed to blocking of the Pt surface sites by specifically adsorbed Cs^+, which limits reactant access[5], this trend alone does not explain the anomalously lower HER activity observed in electrolyte with Rb^+ than that with Cs^+.

Since Cs^+ blocks sites on Pt, we can attribute the lower HER activity in the case of Cs^+ to the surface blockage. From the EIS experiment, we note that the EDL is far denser in the case of Rb^+. We cannot access the full EDL in the simulations due to the limited simulation cell size. However, our AIMD clearly reveals two competing placements of Rb^+ near the Pt surface, which could lead to a greater dynamism and interconversion between these two placements, and result in an effective accumulation of Rb^+ in the EDL. The accumulation process results in a more compact cation layer, as revealed by our EIS studies. This compact layer hinders the transport of water/hydroxyl ions to and from the electrode surface, consequently suppressing the HER activity, as observed in our voltammetric studies. Our Simulations also show that the cations differentially structure the water layer at the interface.

3.4.5. Cation dependent water structuring around adsorbed hydroxyl (OHad) on the Pt surface.

We analyze the structuring of water around adsorbed hydroxyl (OH_{ad}) on the Pt surface as a function of the cation type and preferred location (Fig. 3.5). In the absence of a cation, there is a distinct O_{ad}—H peak centered at ~ 1.6 Å, and two O_{ad}—O peaks at ~2.55 Å and ~ 3.6 Å, indicating

that the OH_{ad} is solvated with the hydrogen bonds to water protons, and a well-defined second solvation shell. The presence of AM^+ disrupt this solvation structure at varying degrees, leading to a striking difference in the O_{ad}—O and O_{ad}—H radial distribution functions (RDFs). In particular, K^+ causes significant OH_{ad} desolvation, shifting the first O_{ad}—O RDF peak to ~ 3.2 Å and fully destroying the second solvation shell. This effect would facilitate HER by reducing water re-organization energy necessary for HER process. Specifically, during the alkaline HER reaction without AM^+, the solvent dipoles need to substantially rearrange from the optimal solvation of the reactant (water) to the optimal solvation of forming product (OH_{ad}) (Supplementary Figure 1, black line). This reorganization costs the system a reorganization energy penalty. In contrast, the presence of K^+ prevents the formation of the optimal solvation structure around OH_{ad}, presumably by tightly binding its solvation shells and organizing the solvent around K^+ itself (Fig.3.5, blue line). In other words, K^+ holds onto the solvent, and hinders its reorganization dynamics from solvating the water reactant, toward then solvating the polar product. This must reduce the entropic part of the free energy barrier of HER in the presence of K^+ compared to the system without AM^+.

Next consider the solvent structure in the presence of the cations located near the surface, Rb^+_s and Cs^+. Strikingly, Rb^+_s shows a nearly identical solvation profile for OH_{ad} to that in pure water (compare black and pink RDF plots in Fig. 3.5). This means that the solvent would fully reorganize during HER, pay the full reorganization entropic penalty, and the barrier will be similar to that in the absence of AM^+, and higher than in the presence of K^+. On the other hand, the specifically adsorbed Cs^+ slightly reduces the number of water molecules in the first solvation shell of OH_{ad} (green line), and slightly increases the number of waters in the second solvation shell. Thus, the solvation structure is disrupted compared to that in pure water only modestly, far from the effect

of K^+, suggesting that Cs^+ will feature worse intrinsic kinetics for HER than K^+, but better than Rb^+_s. Note that this effect is additional to simple site-blocking that Cs^+ and Rb^+_s share.

Furthermore, Rb^+_w located in EDL (purple line) behaves differently than Rb^+_s, and shows a greater reduction of the first OH_{ad} solvation peak in RDF than Cs^+ and Rb^+_s. Thus, this form of the cation in the proximity of the surface would reduce the free energy barrier for HER, though not to the same extent as does K^+. Overall, if local solvent reorganization is taken as a descriptor of the intrinsic HER activity of a site on Pt, the activity should follow the non-trivial trend: $Rb^+_s < Cs^+ < Rb^+_w < K^+$. Thus, the worst HER kinetics for Rb^+ is attributable to the closer-to-the-surface, Rb^+_s sub-population. Since Cs^+ and Rb^+_s also blocks sites on Pt, we can further argue for the $Rb^+_s < Cs^+ << Rb^+_w < K^+$ qualitative trend. Finally, form the experiment, we saw that the EDL is denser for Rb^+. We cannot access the full EDL in the simulations due to limited simulation cell size. However, because we see two competing placements of Rb^+ near the Pt surface, a greater dynamism and interconversion between these two placements can be proposed, leading to the observed effective EDL thickening, and worse transport to and from the electrode surface, further hindering the HER activity in the presence of Rb^+. Details of the mechanistic implications of water structuring will be subject of future investigations.

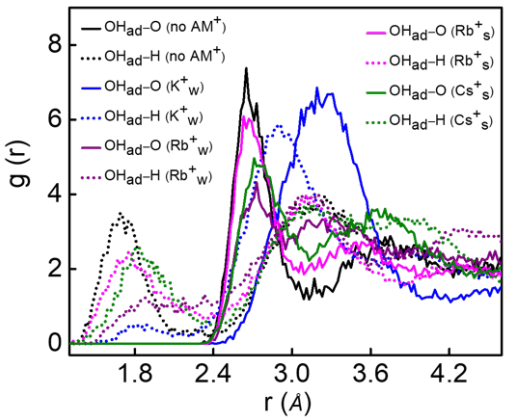

Figure 3.5: AIMD simulations reveal cation behavior at Pt(100)-water interface. Radial distribution functions (RDFs) for OH_{ad}, with different cations, as well as the absence of any cations, with the OH_{ad}-cation distances shown.

This can provide a secondary influence on the mass transport to and from the interface, electronic structure of the adsorbates, and reaction kinetics, through both enthalpic and entropic effects. Thus, on the basis of our combined experimental and theoretical results, we propose that the anomalous HER activity trend of the order $K^+ > Cs^+ > Rb^+$ can be explained by two effects: (1) the specific adsorption of weakly hydrated cations (Cs^+ and sub-populations of Rb^+ cations) on the Pt surface that partially blocks the surface active sites for HER; and (2) the formation of a denser EDL in the case of Rb^+, which hinders the transport of water to and hydroxyls away from the electrode surface and further suppresses HER.

3.5. Conclusions

In summary, by using an integrated study to probe both the on-surface (ETS) and near-surface (EIS) signals, we experimentally proved that Cs^+ specifically adsorbs on the Pt electrode surface to such an extent that they can lower the availability of free surface sites and hence decrease the HER activity, whereas Rb^+ quasi-specifically adsorbs on the Pt surface and accumulates in the electrical double layer to form a denser cation layer, likely facilitated by its unique dynamism near the surface, which hinders the water transport and suppresses the HER activity. To the best of our knowledge, this study provides, for the first time, experimental evidence confirming quasi-specific and specific adsorption of Rb^+ and Cs^+ on the Pt electrode surface, which allows us to rationalize the trend in HER kinetics following $K^+ > Cs^+ > Rb^+$ as resulting from a dual mode of deactivation: blocking the active site (found in Cs^+) and blocking the transport through EDL (found in Rb^+). Our study provides a molecular-level understanding of the fundamental role of weakly hydrated AM^+

in HER kinetics that has remained elusive for decades and is expected to offer valuable insights for the design of more efficient alkaline electrolyzers.

3.6. References

(1) Gasteiger, H. A.; Panels, J. E.; Yan, S. G. Dependence of PEM fuel cell performance on catalyst loading. *Journal of Power Sources* **2004**, *127* (1), 162-171. DOI: https://doi.org/10.1016/j.jpowsour.2003.09.013.

(2) Nørskov, J. K.; Bligaard, T.; Logadottir, A.; Kitchin, J.; Chen, J. G.; Pandelov, S.; Stimming, U. Trends in the exchange current for hydrogen evolution. *Journal of The Electrochemical Society* **2005**, *152* (3), J23.

(3) Chen, X.; McCrum, I. T.; Schwarz, K. A.; Janik, M. J.; Koper, M. T. M. Co-adsorption of Cations as the Cause of the Apparent pH Dependence of Hydrogen Adsorption on a Stepped Platinum Single-Crystal Electrode. *Angewandte Chemie International Edition* **2017**, *56* (47), 15025-15029. DOI: https://doi.org/10.1002/anie.201709455.

(4) Seh, Z. W.; Kibsgaard, J.; Dickens, C. F.; Chorkendorff, I.; Nørskov, J. K.; Jaramillo, T. F. Combining theory and experiment in electrocatalysis: Insights into materials design. *Science* **2017**, *355* (6321), eaad4998. DOI: doi:10.1126/science.aad4998.

(5) Huang, B.; Rao, R. R.; You, S.; Hpone Myint, K.; Song, Y.; Wang, Y.; Ding, W.; Giordano, L.; Zhang, Y.; Wang, T.; et al. Cation- and pH-Dependent Hydrogen Evolution and Oxidation Reaction Kinetics. *JACS Au* **2021**, *1* (10), 1674-1687. DOI: 10.1021/jacsau.1c00281.

(6) Intikhab, S.; Snyder, J. D.; Tang, M. H. Adsorbed Hydroxide Does Not Participate in the Volmer Step of Alkaline Hydrogen Electrocatalysis. *ACS Catalysis* **2017**, *7* (12), 8314-8319. DOI: 10.1021/acscatal.7b02787.

(7) Subbaraman, R.; Tripkovic, D.; Strmcnik, D.; Chang, K.-C.; Uchimura, M.; Paulikas, A. P.; Stamenkovic, V.; Markovic, N. M. Enhancing Hydrogen Evolution Activity in Water Splitting by Tailoring Li^+-$Ni(OH)_2$-Pt Interfaces. *Science* **2011**, *334* (6060), 1256-1260. DOI: doi:10.1126/science.1211934.

(8) Monteiro, M. C. O.; Goyal, A.; Moerland, P.; Koper, M. T. M. Understanding Cation Trends for Hydrogen Evolution on Platinum and Gold Electrodes in Alkaline Media. *ACS Catalysis* **2021**, *11* (23), 14328-14335. DOI: 10.1021/acscatal.1c04268.

(9) Liu, E.; Li, J.; Jiao, L.; Doan, H. T. T.; Liu, Z.; Zhao, Z.; Huang, Y.; Abraham, K.; Mukerjee, S.; Jia, Q. Unifying the hydrogen evolution and oxidation reactions kinetics in base by identifying the catalytic roles of hydroxyl-water-cation adducts. *Journal of the American Chemical Society* **2019**, *141* (7), 3232-3239.

(10) Xue, S.; Garlyyev, B.; Watzele, S.; Liang, Y.; Fichtner, J.; Pohl, M. D.; Bandarenka, A. S. Influence of alkali metal cations on the hydrogen evolution reaction activity of Pt, Ir, Au, and Ag electrodes in alkaline electrolytes. *ChemElectroChem* **2018**, *5* (17), 2326-2329.

(11) Weber, D.; Janssen, M.; Oezaslan, M. Effect of monovalent cations on the HOR/HER activity for Pt in alkaline environment. *Journal of The Electrochemical Society* **2019**, *166* (2), F66.

(12) Bender, J. T.; Petersen, A. S.; Østergaard, F. C.; Wood, M. A.; Heffernan, S. M. J.; Milliron, D. J.; Rossmeisl, J.; Resasco, J. Understanding Cation Effects on the Hydrogen Evolution Reaction. *ACS Energy Letters* **2023**, *8* (1), 657-665. DOI: 10.1021/acsenergylett.2c02500.

(13) McCrum, I. T.; Chen, X.; Schwarz, K. A.; Janik, M. J.; Koper, M. T. M. Effect of Step Density and Orientation on the Apparent pH Dependence of Hydrogen and Hydroxide Adsorption on Stepped Platinum Surfaces. *The Journal of Physical Chemistry C* **2018**, *122* (29), 16756-16764. DOI: 10.1021/acs.jpcc.8b03660.

(14) Ovalle, V. J.; Hsu, Y.-S.; Agrawal, N.; Janik, M. J.; Waegele, M. M. Correlating hydration free energy and specific adsorption of alkali metal cations during CO2 electroreduction on Au. *Nature Catalysis* **2022**, *5* (7), 624-632. DOI: 10.1038/s41929-022-00816-0.

(15) Miller, D. J.; Lisy, J. M. Hydrated Alkali-Metal Cations: Infrared Spectroscopy and ab Initio Calculations of M+(H2O)x=2−5Ar cluster ions for M = Li, Na, K, and Cs. *Journal of the American Chemical Society* **2008**, *130* (46), 15381-15392. DOI: 10.1021/ja803665q.

(16) Mills, J. N.; McCrum, I. T.; Janik, M. J. Alkali cation specific adsorption onto fcc(111) transition metal electrodes. *Physical Chemistry Chemical Physics* **2014**, *16* (27), 13699-13707, 10.1039/C4CP00760C. DOI: 10.1039/C4CP00760C.

(17) Matanovic, I.; Atanassov, P.; Garzon, F.; Henson, N. J. Density functional theory study of the alkali metal cation adsorption on Pt (111), Pt (100), and Pt (110) surfaces. *ECS Transactions* **2014**, *61* (13), 47.

(18) Shah, A. H.; Zhang, Z.; Huang, Z.; Wang, S.; Zhong, G.; Wan, C.; Alexandrova, A. N.; Huang, Y.; Duan, X. The role of alkali metal cations and platinum-surface hydroxyl in the alkaline hydrogen evolution reaction. *Nature Catalysis* **2022**, *5* (10), 923-933. DOI: 10.1038/s41929-022-00851-x.

(19) Li, M.; Zhao, Z.; Cheng, T.; Fortunelli, A.; Chen, C.-Y.; Yu, R.; Zhang, Q.; Gu, L.; Merinov, B. V.; Lin, Z. Ultrafine jagged platinum nanowires enable ultrahigh mass activity for the oxygen reduction reaction. *Science* **2016**, *354* (6318), 1414-1419.

(20) Ding, M.; He, Q.; Wang, G.; Cheng, H.-C.; Huang, Y.; Duan, X. An on-chip electrical transport spectroscopy approach for in situ monitoring electrochemical interfaces. *Nature Communications* **2015**, *6* (1), 7867.

(21) Ding, M.; Zhong, G.; Zhao, Z.; Huang, Z.; Li, M.; Shiu, H.-Y.; Liu, Y.; Shakir, I.; Huang, Y.; Duan, X. On-Chip in Situ Monitoring of Competitive Interfacial Anionic Chemisorption as a Descriptor for Oxygen Reduction Kinetics. *ACS Central Science* **2018**, *4* (5), 590-599. DOI: 10.1021/acscentsci.8b00082.

(22) Zhong, G.; Cheng, T.; Shah, A. H.; Wan, C.; Huang, Z.; Wang, S.; Leng, T.; Huang, Y.; Goddard, W. A.; Duan, X. Determining the hydronium pKα at platinum surfaces and the effect on pH-dependent hydrogen evolution reaction kinetics. *Proceedings of the National Academy of Sciences* **2022**, *119* (39), e2208187119. DOI: 10.1073/pnas.2208187119 (acccessed 2022/09/21).

(23) Kresse, G.; Furthmüller, J. Efficiency of ab-initio total energy calculations for metals and semiconductors using a plane-wave basis set. *Computational Materials Science* **1996**, *6* (1), 15-50. DOI: https://doi.org/10.1016/0927-0256(96)00008-0.

(24) Kresse, G.; Furthmüller, J. Efficient iterative schemes for ab initio total-energy calculations using a plane-wave basis set. *Physical Review B* **1996**, *54* (16), 11169-11186. DOI: 10.1103/PhysRevB.54.11169.

(25) Kresse, G.; Hafner, J. Ab initio molecular dynamics for liquid metals. *Physical Review B* **1993**, *47* (1), 558-561. DOI: 10.1103/PhysRevB.47.558.

(26) Kresse, G.; Hafner, J. Ab initio molecular-dynamics simulation of the liquid-metal--amorphous-semiconductor transition in germanium. *Physical Review B* **1994**, *49* (20), 14251-14269. DOI: 10.1103/PhysRevB.49.14251.

(27) Perdew, J. P.; Burke, K.; Ernzerhof, M. Generalized Gradient Approximation Made Simple. *Physical Review Letters* **1996**, *77* (18), 3865-3868. DOI: 10.1103/PhysRevLett.77.3865.

(28) Adamo, C.; Barone, V. Toward reliable density functional methods without adjustable parameters: The PBE0 model. *The Journal of chemical physics* **1999**, *110* (13), 6158-6170.

(29) Kresse, G.; Joubert, D. From ultrasoft pseudopotentials to the projector augmented-wave method. *Physical Review B* **1999**, *59* (3), 1758-1775. DOI: 10.1103/PhysRevB.59.1758.

(30) Grimme, S.; Antony, J.; Ehrlich, S.; Krieg, H. A consistent and accurate ab initio parametrization of density functional dispersion correction (DFT-D) for the 94 elements H-Pu. *The Journal of chemical physics* **2010**, *132* (15), 154104.

(31) Yoo, H.-W.; Cho, S.-Y.; Jeon, H.-J.; Jung, H.-T. Well-Defined and High Resolution Pt Nanowire Arrays for a High Performance Hydrogen Sensor by a Surface Scattering Phenomenon. *Analytical Chemistry* **2015**, *87* (3), 1480-1484. DOI: 10.1021/ac504367w.

(32) Strmcnik, D.; Kodama, K.; van der Vliet, D.; Greeley, J.; Stamenkovic, V. R.; Marković, N. M. The role of non-covalent interactions in electrocatalytic fuel-cell reactions on platinum. *Nature Chemistry* **2009**, *1* (6), 466-472. DOI: 10.1038/nchem.330.

(33) Shin, S.-J.; Kim, D. H.; Bae, G.; Ringe, S.; Choi, H.; Lim, H.-K.; Choi, C. H.; Kim, H. On the importance of the electric double layer structure in aqueous electrocatalysis. *Nature Communications* **2022**, *13* (1), 174. DOI: 10.1038/s41467-021-27909-x.

(34) Garlyyev, B.; Xue, S.; Watzele, S.; Scieszka, D.; Bandarenka, A. S. Influence of the Nature of the Alkali Metal Cations on the Electrical Double-Layer Capacitance of Model Pt(111) and Au(111) Electrodes. *The Journal of Physical Chemistry Letters* **2018**, *9* (8), 1927-1930. DOI: 10.1021/acs.jpclett.8b00610.

(35) Xue, S.; Garlyyev, B.; Auer, A.; Kunze-Liebhäuser, J.; Bandarenka, A. S. How the Nature of the Alkali Metal Cations Influences the Double-Layer Capacitance of Cu, Au, and Pt Single-Crystal Electrodes. *The Journal of Physical Chemistry C* **2020**, *124* (23), 12442-12447. DOI: 10.1021/acs.jpcc.0c01715.

(36) Ledezma-Yanez, I.; Wallace, W. D. Z.; Sebastián-Pascual, P.; Climent, V.; Feliu, J. M.; Koper, M. T. M. Interfacial water reorganization as a pH-dependent descriptor of the hydrogen evolution rate on platinum electrodes. *Nature Energy* **2017**, *2* (4), 17031. DOI: 10.1038/nenergy.2017.31.

(37) Waegele, M. M.; Gunathunge, C. M.; Li, J.; Li, X. How cations affect the electric double layer and the rates and selectivity of electrocatalytic processes. *The Journal of Chemical Physics* **2019**, *151* (16). DOI: 10.1063/1.5124878 (acccessed 9/7/2023).

(38) Schmickler, W.; Belletti, G.; Quaino, P. The approach of alkali ions towards an electrode surface – A molecular dynamics study. *Chemical Physics Letters* **2022**, *795*, 139518. DOI: https://doi.org/10.1016/j.cplett.2022.139518.

CHAPTER 4

The platinum-surface water orientation dictates hydrogen evolution reaction kinetics in alkaline media

4.1. Introduction and background

The hydrogen evolution reaction (HER) represents a critical step in water electrolysis, a process used to produce hydrogen gas (H_2) from water. This reaction is fundamental to the production of green hydrogen, which is considered a clean and sustainable energy carrier, especially when coupled with renewable energy sources[1,2]. In general, the HER involves three elementary steps depending on the electrolyte conditions. The first step is one electron reduction of a proton on the Pt electrode to form Pt–H_{ad} (the Volmer step, Equation 4-1, 4-2):

$$H_3O^+ + e^- + Pt \leftrightarrow Pt—H_{ad} + H_2O \qquad \text{(acidic)} \qquad (4\text{-}1)$$

$$H_2O + e^- + Pt \leftrightarrow Pt—H_{ad} + OH^- \qquad \text{(alkaline)} \qquad (4\text{-}2)$$

In the second step, molecular hydrogen (H_2) can form either via recombination of two adsorbed hydrogens (Pt—H_{ad}) (Tafel step, Equation 4-3):

$$2\ Pt—H_{ad} \leftrightarrow H_2 + 2\ Pt \qquad (4\text{-}3)$$

or by a simultaneous proton reduction on electrode surface and its reaction with the surface bound H (Pt—H_{ad}) to form molecular hydrogen (Heyrovsky step, Equation 4-4, 4-5):

$$Pt—H_{ad} + H_3O^+ + e^- \leftrightarrow H_2 + Pt + H_2O \qquad \text{(acidic)} \qquad (4\text{-}4)$$

$$Pt—H_{ad} + H_2O + e^- \leftrightarrow H_2 + Pt + OH^- \qquad \text{(alkaline)} \qquad (4\text{-}5)$$

The HER kinetics on platinum (Pt) surface typically displays a distinct dependence on electrolyte pH, with the HER kinetics in alkaline conditions are considerably slower than in acidic media[3-5], which has been attributed to a switch of proton donor from H_3O^+ in acidic conditions to H_2O in alkaline conditions[6-8]. However, the precise switching point and the underlying molecular mechanism has been elusive and a topic of considerable interest. Our recent studies in acidic and neutral electrolytes revealed that the switch of proton source occurred at a pH around 4 instead of acid/base boundary, which is attributed to a change of Pt surface-H_2O protonation status and associated with Pt surface hydronium pKa (4.3)[7]. However, the change of proton source from H_3O^+ to H_2O cannot explain HER activity difference in alkaline media.

The hydrogen binding energy (HBE), widely accepted as a thermodynamic descriptor of the HER activity, has been frequently used to interpret the pH-dependent HER kinetics[1,9-14]. For example, Sheng *et al.*[1] and Durst *et al.*[15] independently suggested that HBE derived from the pH-dependent hydrogen underpotential deposition (H_{upd}) peak may serve as an effective descriptor for interpreting pH dependent HER kinetics. However, it has been argued by Koper and coworkers that the H_{upd} peak is not solely associated with the hydrogen adsorption but also convoluted with the hydroxide desorption on step sites[16]. Thus, the pH dependent H_{upd} peak potential is not an unambiguous indicator of the HBE.

To this end, Koper *et al.* introduced potential of zero free charge (pzfc) theory to explain the different HER kinetics in acid and alkaline media[3]. They argued that in acidic media, the pzfc is closer to the HER region and reorganization energy of interfacial water associated with transporting a proton through electrical double layer is smaller and hence the HER kinetics is more facile[3]. Whereas, in alkaline media the pzfc is far from the HER region (i.e., closer the OH_{ad} region), leading to a stronger electric field in HER region and a larger interfacial water

reorganization energy, which impedes OH^- transfers through double layer[3]. However, the pzfc theory cannot explain the higher HER kinetics at pH 13 compared to pH 7 as the reorganization energy at pH 13 is expected to be considerably larger than that at pH 7[17]. Besides the aforementioned theories, it has also been suggested that the other factors including water dynamics[18,19], transport of related intermediates (H_2O*/OH*) at the electrode/electrolyte interface [20,21] and interfacial hydrogen bond networks[22] in alkaline media may also play a critical role in HER kinetics.

Despite extensive aforementioned efforts in comparing the acidic and alkaline media, the HER kinetics within the alkaline (pH > 7) media was often considered pH independent on Pt (111) surface[6,23] and much less explored[17,24-26]. Koper *et al.* recently investigated the pH-dependent HER kinetics on Au electrode in alkaline media, found higher HER activity at higher pH, and attributed it to the increased local cations concentration at higher pH that stabilizes the transition state of the rate-determining Volmer step via a favorable interaction with the dissociating water molecule ($*H–OH^{\delta-}–cation^+$)[17]. Likewise, Qiao *et al.* attributed the higher activity in high-pH electrolytes to the locally generated H_3O^+ intermediates that create a unique acid-like local reaction environment on nanostructured catalytic surfaces and reduce the energy barrier for the overall reaction[24]. Recently, Surendranath *et al.* also observed a decrease of HER overpotential on Au and Pt electrodes with increasing pH above 10, although the underlying reason was not substantially discussed[25]. Despite these interesting studies and suggestions, a molecular level understanding of the HER on Pt electrode in alkaline media has not been developed due to the lack of robust experimental techniques that can reveal molecular level insights across the Pt-electrolyte interface.

Herein, we address this issue by systematically studying the HER kinetics in non-buffered alkaline media (pH 7 – 13) on polycrystalline Pt electrode surface. Our systematic studies reveal

a sharp switch of Tafel slope (from ~110 mV/decade below pH 10 to ~53 mV/decade above pH 10) and exchange current density (from ~ 0.002 mA/cm^2 below pH 10 to > 0.5 mA/cm^2 above pH 10), signifying a switch of the HER kinetics. We further employed electrical transport spectroscopy (ETS) to reveal the molecular level insights on interfacial water structure on Pt surface. The ETS conductance signal reveals nearly constant conductance below pH 10, and a notable increase above pH 10, suggesting a change in surface speciation in these two distinct pH regimes. Static and dynamic fixed-potential (FP) density functional theory (DFT) calculations show that the interfacial water molecules adopt the O-down configuration below pH=11 and flip to the H-down configuration above pH=11, correlating well with the experimentally observed switch of HER kinetics and ETS signals. The switching of the interfacial water molecule orientation to H-down configuration changes the partial charge distribution and weakens the O–H bond in the interfacial water molecule, which accelerates alkaline Volmer kinetics. This excellent correlation of the experimentally observed switch in Tafel slope, exchange current density and the ETS conductance signal, with the theory-predicted water orientation change, for the first time, provides a robust molecular-level interpretation of the pH-dependent HER kinetics on Pt surface in alkaline media. Such molecular level understanding will be instrumental in guiding further fundamental understanding and eventually the rational design of optimized electrode-electrolyte conditions for alkaline electrolysis.

4.2. Experimental details

4.2.1. Chemicals

Potassium hydroxide (KOH, 87.4%), potassium perchlorate ($KClO_4$, 99%) and perchloric acid ($HClO_4$, 70%, PPT grade) were all purchased from Thermo Fisher Scientific. Potassium

hexachloroplatinate(IV) (K_2PtCl_6), Ethylene glycol and Dimethylformamide were purchased from Sigma Aldrich. All aqueous solutions were prepared using deionized (DI) water (18.2 MΩ·cm) obtained from an ultrapure purification system (Aqua Solutions).

4.2.2. Electrochemical and ETS measurements

All of the electrochemical measurements were performed using typical three electrode setup. Platinum rotating disk was used as working electrode, Pt wire and Ag/AgCl were used as the counter and reference electrodes, respectively. The electrolyte solution of 0.1 M ionic strength was used in all measurements. A mixture of KOH and $KClO_4$ was used for adjusting the pH of electrolyte.

4.2.3. Synthesis of Pt nanowires (PtNWs)

PtNWs were synthesized as reported previously[27]. Briefly, a mixture of KOH (0.6 g) and ethylene glycol (4 ml) was dissolved in DMF (6 ml). Aqueous solution of K_2PtCl_6 (8 wt%, 0.1 ml) was then added into the mixture. After stirring for 20 min, the reaction mixture was transferred into a Teflon-lined autoclave, which was maintained at 150 °C for 15 h and then cooled to room temperature. The black powders were collected after the reaction and washed with ethanol and deionized (DI) water repeatedly for several times before use. The transmission electron microscopy (TEM) studies revealed ultrafine nanowires structure of Pt (Fig. 4.1a). The powder X-ray diffraction study showed the resulting PtNWs exhibit face centered cubic (fcc) structure of platinum (Fig. 4.1b).

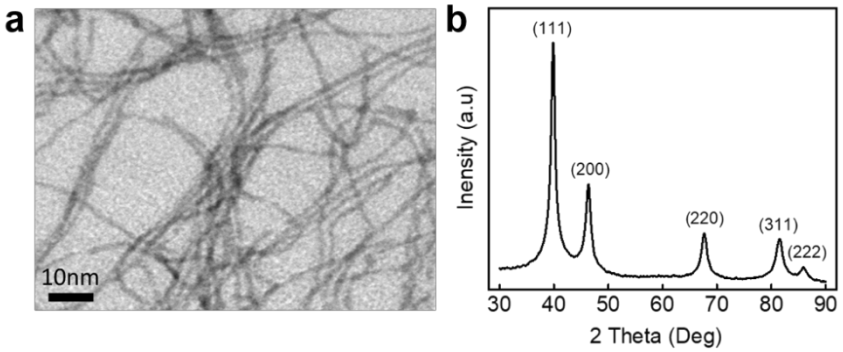

Figure 4.1: Structural characterizations of the PtNWs. (a) TEM image of the as-prepared PtNWs. (b) XRD patterns of PtNWs. Pt peaks are labeled and can be ascribed to an underlying Pt fcc structure (JCPDS database #04-0802).

4.2.4. Material characterization

SEM image was taken using a JEOL JSM-6610 SEM and TEM image was taken with an FEI T12 TEM operated at 120 kV. X-ray powder diffraction pattern was collected with a Panalytical X'Pert Pro X-ray powder diffractometer using Cu Kα radiation as an incident beam.

4.2.5. Preparation of PtNWs films

A free standing PtNWs film was assembled on chip from as-prepared PtNWs suspension by a co-solvent evaporation method[27]. Briefly, PtNWs suspensions in ethanol (400 µl, 0.4 mg ml^{-1}) was added dropwise into a beaker (about 9 cm in diameter) filled with DI water. A thin film of PtNWs from top of water surface was then transferred onto the device.

4.2.6. Fabrication of the PtNWs electrochemical device

The device fabrication was followed by the similar approach as previously reported by our group[27]. Typically, a PMMA (A8, MicroChem Corp.) film was prepared by spin coating on the substrate (p++ silicon wafer with 300 nm thermal oxide) surface with pre-patterned Au electrodes (Ti/Au, 10/50 nm). E-beam lithography was then used to open windows on PMMA, which created desired patterns on the substrate. After the removal of PMMA template, PtNWs was deposited on the

device substrate with desired patterns. To rule out the influence of electrolyte and to avoid electrochemical reactions on the Au electrodes, another layer of PMMA (~500-nm thick, electrochemically inert) was then deposited on the PtNW device with spin coating (Fig. 4.2a). A smaller window that only exposes PtNWs was opened by e-beam lithography (Fig. 4.2b). The device was finally used for in-device electrochemistry and *in situ* electrical transport spectroscopy measurement. The scanning electron microscopy (SEM) image of the ETS device shows the PtNWs network connecting Au electrodes (Fig. 4.2c)

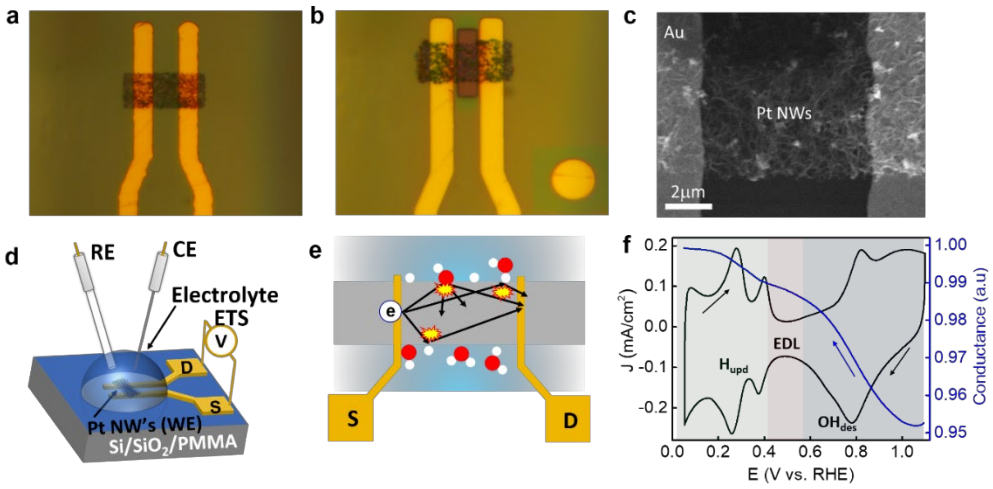

Figure 4.2: Structural characterizations of the electrical transport spectroscopy (ETS) device and schematic illustration of experimental setup and working principle of the ETS measurement. (a) Microscopic image of ETS device covered with PMMA. (b) Microscopic image of the micro-fabricated on-chip ETS device with PtNWs network exposed in the opened PMMA window. (c) Scanning electron microscopy image of the ETS device. (d) on-chip PtNWs device for ETS measurements. (e) electrons scattering mechanism of various adsorbate molecules on Pt NWs. (f) Typical ETS spectra and cyclic voltammogram with representation of various regions 0.1 M KOH solution (Panels d and e adapted from ref.[29] with permission. Copyright 2022 The Author(s), under exclusive license to Springer Nature Limited).

4.2.7. In-device CV and in situ ETS

A two channel SMU (Agilent B2902a) was used for the measurement. The first SMU channel was used as a potentiostat to control the potential of source electrode as to the reference electrode (V_G), while collecting the current (I_G) through the counter electrode with a scan rate of 50 mV/sec. The

second channel was used to supply a small voltage of (10 mV) between source and drain electrodes and collecting the corresponding current (I_{SD}) (Fig. 4.2d).

The electrical conductivity of the metallic PtNWs is sensitive to surface environment, due to surface scattering of the conduction electrons, producing a resistance change following equation[27].

$$\rho = \rho_0 \left(\left(\frac{1-p}{1+p} \right) \times \frac{\lambda}{d} \right) \quad (d \ll \lambda) \qquad (4\text{-}6)$$

Here ρ and ρ_0 are the resistivity of the one dimensional PtNWs and bulk metal respectively, λ is the mean free path of electron, d is the nanowire diameter, and p is a specularity parameter with a value ranging from 0 (for highly diffusive scattering) to 1 (completely specular scattering) (Fig. 4.2e)[36]. When the diameter (d) of the PtNWs is smaller than the electron mean free path ($\lambda \sim$ 5 nm)[36], their resistance is highly dependent on the exact surface adsorbate that modifies the value of specularity (p). It is important to note such surface scattering is exclusively sensitive to surface adsorbates, with little impact for the electrostatic or electrochemical potential. For example, previous studies have clearly shown a constant conductance at different electrochemical potentials when there is a stable surface adsorbate layer (*e.g.*, CO or I^-) that does not change with potential[27,28], clearly demonstrating the insensitivity of the metallic PtNWs to the varying electrochemical potentials. Thus, the ETS approach offers a unique signal transduction pathway to exclusively probe the surface adsorbates, with minimum interferences from the electrochemical potentials or the bulk electrolyte environment, which is difficult to achieve with other analytic approaches that are often convoluted with near surface (e.g., EDL) or bulk electrolyte background.

We have first closely compared the ETS measurement with the corresponding CV curve at pH 13 when the potential is gradually changed from 1.10 – 0.05 V *vs.* RHE (Fig. 4.2f), which consistently shows three distinct regions: (i) $O/OH_{ad/des}$ region (1.10-0.60 V vs. RHE); (ii) electrical double

layer region (OH_{ad} replaced by H_2O) (0.60-0.40 V vs. RHE); and (iii) H_{upd} and HER regime (0.40-0.05 V vs. RHE). The lowest conductance observed in the high potential regime is attributed to the larger scattering from the strongly bonded OH_{ad} on the Pt surface, which significantly reduces the conductance of the PtNWs. Scanning the potential toward lower potential regime results in a monotonic increase in conductance due to the gradual replacement of the OH_{ad} by H_2O. The conductance increase slowed in the double layer regime where Pt surface are nearly completely reduced and most of the OH_{ad} are replaced by H_2O. Further sweeping the potential to the more negative regime results in H_{upd} on electrode surface (replacement of surface adsorbed H_2O and residue OH_{ad} by H_{upd}), which further reduces scattering and increases conductance. The conductance eventually saturates at a nearly stable value below 0.15 V *vs.* RHE (beyond the H_{upd} peak in CV) due to the formation of a complete hydrogen monolayer adsorption.

4.2.8. Reliability of ETS method

The reliability/validity of our experiments was confirmed by repeating sets of experiments. For example, Fig. 4.3 shows three different devices in different pH media showing the same trend. Although the exact conductance value varies, the overall trend and pH-dependent switching point are highly reproducible.

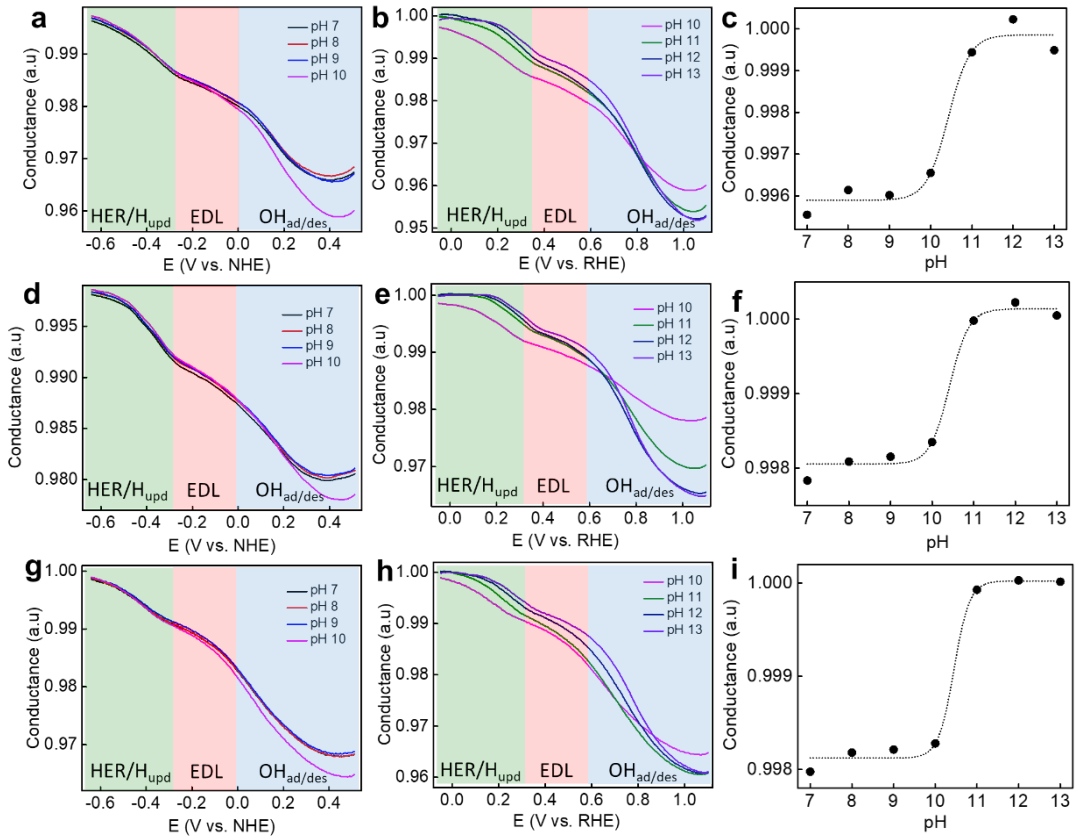

Figure 4.3: Electrical transport spectroscopy (ETS) measurements on three different ETS devices. (a,d,g) ETS spectra in pH 7-10 versus NHE scale, (b,e,h) pH 10-13 versus RHE scale in 0.1 M electrolyte (ionic strength and pH was maintained by KOH and $KClO_4$) and (c,f,i) Plot of conductance versus electrolyte pH at -0.59 V versus NHE (from pH 7-10) and 0 V versus RHE (from pH 10-13) (the dotted line is guide to eye).

We have also calculated the noise level of the ETS by normalizing the total conductance changes at 0 V versus RHE between 0 to 1 (Fig. 4.4). The maximum standard deviation of three different measurements was considered as a noise and the difference in conductance at pH 10 and 11 was considered as signal. In this case, the minimum signal to noise ratio (to identify the switching point) was calculated as ~9.2.

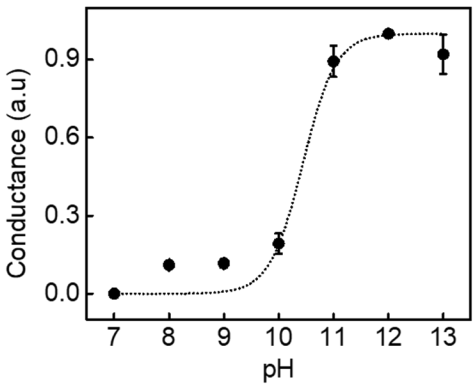

Figure 4.4: Average of normalized conductance from three devices. Plot of normalized conductance versus electrolyte pH at -0.59 V versus NHE (from pH 7-10) and 0 V versus RHE (from pH 10-13) (the dotted line is guide to eye).

4.3. Computational Details

4.3.1. Model Set-up

In the static calculations, the Pt/water electrochemical interface is modelled by an orthogonalized 4-layer 4×4 supercell of Pt(111) termination with one water molecule adsorbed atop. The bottom two layers of the Pt slab are constrained as bulk region, and everything else is allowed to relax as the interface region. A vacuum slab of the 15 Å thickness is added in Z direction to avoid spurious interactions between periodic images.

In the molecular dynamics simulations, 36 explicit water molecules (water slab is c.a. 10 Å thick) are placed above the Pt(111) surface for more realistic description of the interfacial solvation structures. The water configurations are pre-equilibrated using TIP4P force field[37]. Hydroxide is introduced by removing one H from a surface-adsorbed water.

4.3.2. Electronic Structure Methods

The periodic electronic structure calculations are performed with density functional theory, using PBE functional[38] and PAW pseudopotentials[39] implemented in the VASP program (version

5.4.1)[40-43]. D3 correction is used to better account for the dispersion interactions[44]. The convergence criterion for SCF electronic minimization is set to 10^{-5} eV. Due to the relatively large system and sampling size, only the Γ *k*-point is sampled in the reciprocal space of the Brillouin zone throughout, and the cutoff energy for the kinetic energy of the plane-waves was 400 eV.

The solvation effect and electrolyte distribution beyond the slab regions are described implicitly by a polarizable continuum with linearized Poisson-Boltzmann model as implemented in VASPsol code[45]. The dielectric constant is taken as 78.4 (water), and the Debye length is taken as 3 Å.

All periodic electronic structure analyses are performed based on converged charge density or wavefunction. The Bader charges are calculated using Bader Charge Analysis program[46]. The COHP analysis is performed using LOBSTER program with the pbeVaspFit2015 basis set[47].

The molecular fragment calculations are performed with ωB97X-D functional[48] and def2-TZVP basis sets[49] using the Gaussian 16 program[50] (Revision C.01). Molecular orbital visualization and Mayer bond order analysis are performed using the Multiwfn program[51] on the converged wavefunctions from DFT calculation.

4.3.3. Fixed-potential Treatments

Under a constant electrode potential, the electrode surface is effectively a grand canonical ensemble of electrons where the system can exchange electrons with the electrode (electron reservoir) until the work function of the system aligns with the electrode potential. This treatment has been demonstrated to be necessary in investigating the potential-dependent geometric changes and energetics at an electrochemical interface[32,52].

Here we use the fixed-potential method as implemented in the EChO Python package (https://github.com/zishengz/echo). To be specific, the number of electrons is being optimized in

an outer iteration after SCF convergence of each ionic step (geometry optimization step or MD step) to adjust the work function of the system to align with the given electrode potential. This treatment does not depend on the constant capacity approximation or interpolation and hence can exactly capture the potential-dependent geometric changes and the resulted shift in potential of zero charge and effective capacity.

Due to difficulty in continuously adjusting the number of hydroxide ions in the explicit solvation model within the pH range of interest, the pH effect at a constant potential in RHE scale is modeled by shifting the potential in SHE according to the Nernst equation:

$$U_{RHE} = U_{SHE} + \ln 10 \, k_B T \, pH \qquad (4\text{-}7)$$

4.3.4. Fixed-potential ab initio Molecular Dynamics Simulations

The ab initio molecular dynamics simulations are performed on the pre-equilibrated structures and with the same DFT settings as in the geometry optimization. The nuclear motions are treated under the Born-Oppenheimer approximation. The simulation is performed within the NVT ensemble at 300 K using the Langevin thermostat (with a friction coefficient of 0.1) which has been demonstrated to cause the least inconsistency of local temperature in solid/liquid interfacial models[53]. To study the interfacial dynamics at different pH at the same potential in RHE scale (corresponding to different potential in NHE scale), the fix-potential treatment is introduced by performing a potentiostating step (adjusting the number of electrons in the system by time a factor of 0.5 e/V to the difference from the target potential) after each nuclear motion[54]. The analysis of pair radial distribution function and coordination numbers are performed using the VMD software[55].

The free energy profile of water dissociation under the fixed-potential condition are obtained by sampling along the reaction coordinate ξ for an interfacial water molecule. The configurational samplings are performed using the slow-growth technique where ξ is varied sufficiently slow (0.001 Å *per* MD step) to equilibrate all degrees of freedom other than the reaction coordinate, which in the end yields a well-sampled blue moon ensemble. Thermodynamic integration is performed within the blue moon ensemble to obtain the free energy gradient along the reaction coordinate, which is then integrated to recover the free energy profile.

4.3.4.1. Details of the free energy calculation based on fixed-potential MD

To calculate the free energetic of water dissociation, a rare event, we employed the slow-grow approach to sample uniformly along the reaction coordinate ξ as defined in Fig. 4.5a. To be specific, the reaction coordinate is constrained by the SHAKE algorithm[56] and then varied at a constant rate $\frac{d\xi}{dt}$ of 0.001 Å/fs which is sufficiently slow for all degrees of freedom other than the reaction coordinate to fully equilibrate. The resulted samples constitute a blue moon ensemble where the free energy gradient $\left(\frac{\partial F}{\partial \xi}\right)_{\xi^*}$ at any ξ^* can be calculated based on the mass metric tensor and the Lagrange multiplier associated with the ξ in the SHAKE algorithm[57]. The free energy difference between any two states, ξ_1 and ξ_2, can be calculated by integrating the free energy gradient:

$$\Delta F_{1\to 2} = \int_{\xi_1}^{\xi_2} \left(\frac{\partial F}{\partial \xi}\right)_{\xi^*} \left(\frac{d\xi}{dt}\right) dt$$

By performing integration from the initial state up to any state along the reaction coordinate, we can obtain the free energy profile as exemplified in Fig. 4.5b.

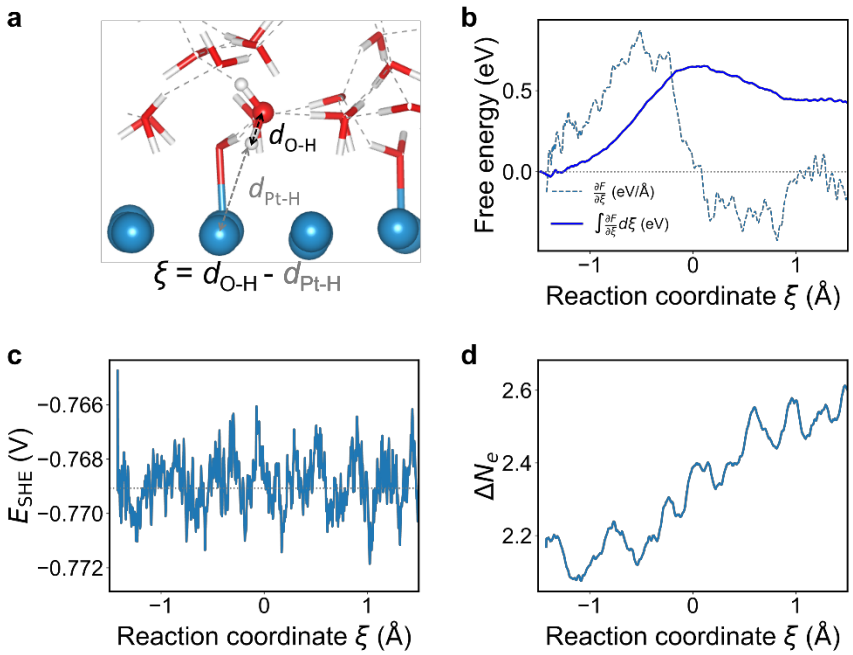

Figure 4.5: Details of the fixed-potential free energy calculation of water dissociation at pH=14. (a) The definition of reaction coordinate ξ for the water dissociation reaction, with negative values and positive values representing intact and dissociated states of the interfacial water, respectively. (b) The free energy gradient and integrated free energy along the reaction coordinate. (c) Fluctuation of potential (SHE scale) of the system along the reaction coordinate, with grey dotted line marking the target potential (E_{RHE}=0 V, pH=14). (d) Fluctuation in the net number of electrons in the system along the reaction coordination, which indicates the charge transfer between the surface and the electrode (electron reservoir) during the reaction.

Note that the whole configurational sampling is performed under a fixed-potential condition by a theoretical potentiostat which stabilizes the potential of the system around the target potential with minimal fluctuations (Fig. 4.5c). The fluctuation of net number of electrons in the system associated with the reaction can also be tracked along the reaction coordinate, and the charge transfer accompanying the water dissociation is evaluated to be ca. 0.5 |e| (Fig. 4.5d).

4.3.4.2. Limitations and justifications of our fixed-potential MD simulations

In this work, we study the pH effect at the same electrode potential (RHE scale) by aligning the workfunction of the system to different absolute potentials (SHE scale) according to the Nernst equation. Such practice corresponds to adjusting the surface charge in response to pH changes,

and we assume the charge transfer between the electrode and the catalyst surface to be much faster than the solvation dynamics at the interface, so that the charge state and the workfunction can fully equilibrate after every local optimization or MD step.

We do not include any explicitly solvated hydroxides in this work to model pH effect because: (i) Given the affordable system size, it is not possible to continuously tune the hydroxide concentration in the pH range of interest (7 to 14). (ii) Within the grand canonical DFT + hybrid solvation scheme, presence of explicit charged solutes can cause artifacts where the counter charge density leaks into the solvation shell and compete with the actual solvent molecules in solvating the charged solute[58-60]. Such artifacts would cause unphysical dynamics of the solvents and the interfacial charge distribution; hence we do not include any explicit solvated hydroxide or cations in the simulation box. (iii) The concentration of solvated hydroxide in the contact layer of the cathode is expected to be negligible. Even if present, they would not disrupt the solvation structure like the larger cations[29] and hence should not alter the overall statistics of interfacial water orientation qualitatively.

The effect of surface adsorbates are probed by additional simulations with surface coverage of *H or *OH, at low or high pH (Fig. 4.6 a,b). The pH response of interfacial water orientation remains qualitatively the same as the case of bare Pt surface. We do not consider a very high coverage case, since the metal surface can undergo more complex H-induced restructurings[61-63], which would require more sophisticated configuration sampling and is beyond the scope of this study. In addition, herein we are particularly interested in the organization of water over the bare Pt sites where water dissociation can take place, instead of the adsorbate occupied sites.

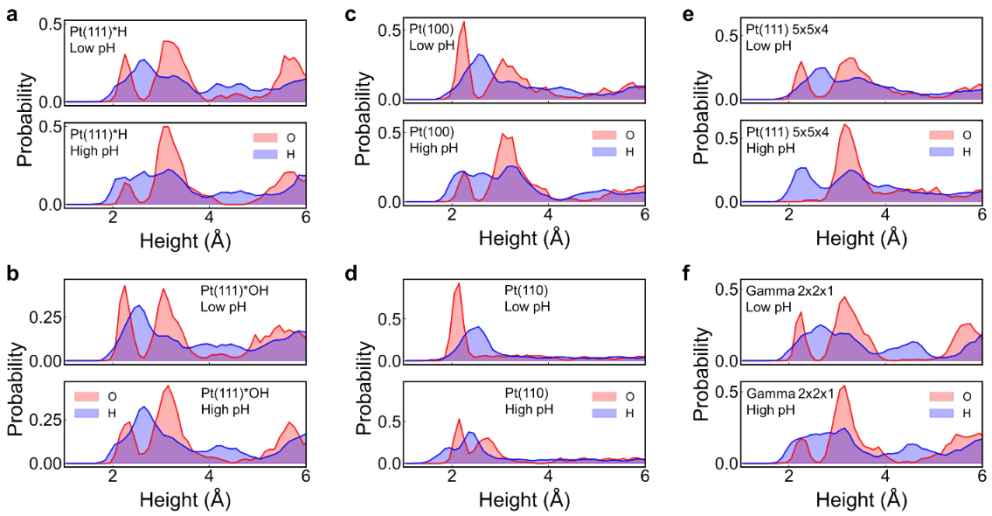

Figure 4.6: Additional simulations with multiple factors considered. The spatial distribution of O and H in the water layer from fixed-potential MD simulations (each of ca. 10 ps duration) at low and high pH values for (a) Pt(111) with *H adsorbate of 1/16 ML coverage, (b) Pt(111) with *OH adsorbate of 1/16 ML coverage, (c) Pt(100), (d) Pt(110), (e) a larger 5×5×4 slab of Pt(111), (f) with a higher K-points of 2×2×1 Gamma points for reciprocal space sampling.

Since the sample is a polycrystalline Pt nanowire, we have also performed additional simulations at low or high pH on Pt(110) and Pt(100) surfaces which have different surface Pt coordination states and different adsorption energetics from those pt Pt(111). The results of these simulations, as shown in Fig. 4.6 c,d, indicate that while the shape of the spatial distribution of O and H may be slightly different from those of Pt(111), the reorientation of interfacial water from O-down to H-down when pH goes from low to high is qualitatively consistent with the case of Pt(111). This suggests that the pH-dependent surface charge, rather than the surface structure, is the dominant factor driving the observed water reorientation.

We have also performed simulations with a larger slab size of 5×5×4 Pt(111), which is approximately 156% of the surface area of the original slab, and with a higher k-point of 2×2×1 Gamma point to sample the reciprocal space, at low or high pH values. Both sets of simulations (Fig. 4.6 e,f) yield pH-response of the interfacial water orientation consistent with Fig. 3c and the main conclusions of this study. While larger unit cells would be preferable, computational

limitations and simulation time to equilibration make this challenging for ab initio molecular dynamics simulations. Our previous works and those of others using similar methods[29, 64-66] have shown that our cell size is sufficient to avoid spatial correlation issues from periodic boundary conditions and yield correct spatial of interfacial water. Moreover, the orientational switch of interfacial waters has an electronic origin (pH-dependent surface charge) that is not strongly dependent on the surface area or the thickness of the water slab.

While we acknowledge that many realistic factors (independent or interdependent) may influence the solvation structure of the interfacial waters, our additional tests in Fig. 4.6 demonstrate that the pH trend remains qualitatively consistent regardless of these additional complexities probed herein. It is possible that the presence of other complexity may "shift" the distribution of water orientation and account for the ~1 pH unit discrepancy compared to the experimental "critical pH" of the orientational switch, but the probed complexities should not be the major factor in driving this pH-dependent and phase transition-like reorganization of interfacial water.

4.4. Results and discussion

4.4.1. pH dependent voltammetric characteristics and HER activity

The pH dependence of the HER kinetics is an intriguing topic. If we assume protons (hydroniums) as the reactant ($H_3O^+ + e^- + * \rightarrow H_{ad} + H_2O$), the thermodynamic onset potential for HER is expected to be constant on the reversible hydrogen electrode (RHE) scale but negatively shifts 59 mV for each pH increase in the normal hydrogen electrode (NHE) scale ($E_{RHE}=E_{NHE} + 0.059$ pH), according the Nernst equation ($E = E^0 - 0.059$ pH). On the other hand, the situation could be different in the neutral or alkaline condition, in which the Volmer step ($H_2O + e^- + * \rightarrow H_{ad} + OH^-$) is believed to be the rate limiting. In this case, the onset potential is expected to be

independent of the electrolyte pH (thus constant on the NHE scale) because no proton or hydroxide is involved on the reactant side. It has been previously suggested that HER in alkaline media does not involve protons, and one should not expect a pH dependence[6, 23]. Thus, a plot on the NHE scale has been frequently used for alkaline media[6, 23]. We investigated the voltammetric response of HER on a Pt surface using cyclic voltammetry (CV) in alkaline media of different pH between 7-13. Our CV studies reveal that the H_{upd} peak potential from pH 7 to pH 9 is largely independent of pH value, showing a nearly constant peak position or onset potential in the NHE scale (Fig. 4.7a), while the H_{upd} peaks in pH 11-13 show clear pH dependence and thus were compared on the pH dependent RHE scale (Fig. 4.7b). The CV of pH 10 is showing a transition from pH independent to pH dependent H_{upd} peaks and hence presented both on the NHE and RHE scale as a reference point. Overall, the H_{upd} peak intensity increases with increasing pH and is significantly larger above pH 10. Likewise, the HER polarization curves in pH 7-9 is largely pH independent (Fig. 4.7c) and show similar HER onset potential on the NHE scale, whereas show a clear pH dependence in pH 11-13 with a comparable onset potential on the RHE scale but an apparently increase HER activity with increasing pH (Fig. 4.7d). Previous studies of nanostructured Pt[24] or Au[17] electrodes have also shown a similar increase of HER activity with increasing pH in alkaline media[25,26]. We note that there is a study reporting a decrease of HER activity on Pt(111) electrode with increasing pH from 11 to 13[3], which is intriguing but not confirmed by other studies yet, to the best of our knowledge.

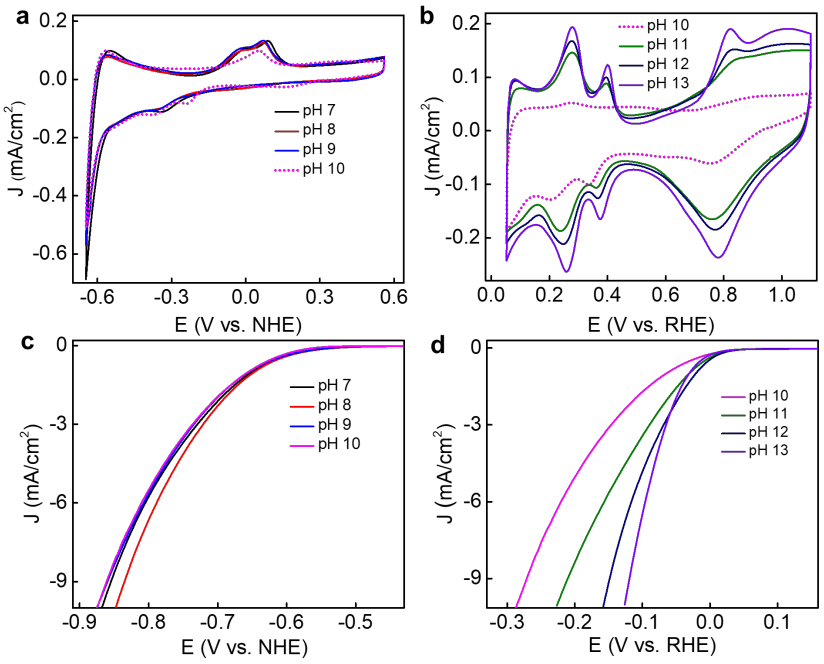

Figure 4.7: Voltammetric studies in 0.1 M electrolyte solution with different pH. (a) CV on stationary Pt disc electrode in N_2-saturated electrolyte of pH 7, 8, 9 and 10 versus pH independent NHE scale and (b) pH 10, 11, 12 and 13 versus pH dependent RHE scale at scan rate of 100 mV/sec (pH was adjusted by KOH and $KClO_4$) (c) IR-corrected HER polarization curves collected in N_2-saturated electrolyte solution of pH 7, 8 and 9 versus pH independent NHE scale and (d) pH 10,11,12 and 13 versus pH dependent RHE scale at scan rate of 5 mV/sec with rotation rate of 1600 rpm (electrolyte concentration was maintained 0.1 M in all cases and the pH was adjusted by KOH and $KClO_4$).

Considering the potential ambiguity of the NHE to RHE conversion, the Tafel slope and exchange current density give a more reliable evaluation of the reaction kinetics (Fig. 4.8 a,b). Importantly, the Tafel slopes and exchange current densities show an apparent transition at pH 10 (Fig. 4.8b). In particular, the Tafel slopes display a notable switch from a value of ~110 mV/decade below the pH 10 to ~53 mV/decade above pH 10 (Fig. 4.8b), suggesting a switch of rate determining step at around pH 10 and a more favorable HER kinetics at higher pH alkaline media. Likewise, the exchange current density versus pH plot also showed two distinct regimes: a much lower value of ~ 0.002 mA/cm^2 in the electrolyte of pH 7 to 9 indicating slower kinetics in the neutral pH regime. At pH 10, the intrinsic HER/HOR activity starts to increase with the exchange current density value of ~0.1 mA/cm^2, which reaches beyond ~ 0.5 mA/cm^2 at pH 11-13. This

trend is largely similar to the Tafel slope. The slightly lower exchange current density and larger Tafel slope in case of pH 13 compared to pH 11 and 12 is attributed to the higher local cation concentration at the interface (due to higher pzfc and larger interfacial electrical field) that negatively impacts the HER/HOR kinetics.[3]

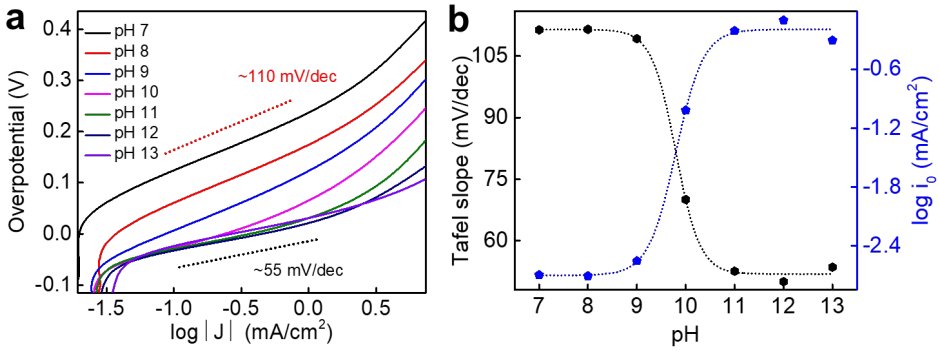

Figure 4.8: Tafel slope and exchange current density in 0.1 M electrolyte solution at different pH. (a) Tafel plots in different pH electrolyte collected on Pt disc electrode with rotation rate of 1600 rpm at a scan rate of 5 mV/sec in N_2-saturated 0.1 M ionic strength electrolyte solution (pH was adjusted by KOH and $KClO_4$) and (b) Plot of Tafel slope values and exchange current density versus electrolyte pH (the dotted lines are guide to eyes).

4.4.2. On chip in-situ monitoring of the pH dependent Pt-surface adsorbates

To understand the molecular level origin of the non-trivial pH dependence of HER kinetics in alkaline media, we employed electrical transport spectroscopic (ETS) studies to directly probe the Pt surface adsorbates at different pH. Using ultrafine Pt nanowires (PtNWs) as a model catalyst[7,27,28], the ETS approach involves a concurrent measurement of the PtNWs conductance during electrochemical studies in a micro-fabricated on-chip device at different electrochemical potentials (see Fig. 4.2 and ref.[27] for detailed working principle of the technique). In general, the conductance of the ultrafine metallic PtNWs measured in ETS studies is highly sensitive to the exact surface adsorbates due to surface scattering of the conduction electrons, but insensitive to the electrostatic or electrochemical potential. The ETS approach thus offers a unique signal transduction pathway to exclusively probe the surface adsorbates, with minimum interferences

from the electrochemical potentials or the bulk electrolyte environment, which is difficult to achieve with other analytic approaches that are often convoluted with or dictated by the near surface (e.g., electrical double layer) and bulk electrolyte background.

Prior to ETS measurements, the PtNW surface was sufficiently cleaned though repeated cycles in 0.1 M $HClO_4$ between 1.1 and 0.05 V vs. RHE in flow cell until reaching a stable conductance signal. The chamber and device were then thoroughly washed with deionized water to ensure a complete removal of any unintentional surface adsorbents. Finally, the device was used in different pH media to obtain the ETS measurements. The ETS studies show the PtNWs generally exhibit a lower conductance in the hydroxide adsorption/desorption potential regime, which is attributed to the more pronounced scattering of the conduction electrons by the strongly bonded OH_{ad}/O_{ad} on the Pt surface in this potential regime[29]. Sweeping the electrochemical potential to the negative direction results in a gradual change of surface adsorbates and thus the corresponding conductance behavior: (i) in the EDL region, the OH_{ad}/O_{ad} are replaced by interfacial H_2O molecules, which reduces the electron scattering and results in an increase in conductance; and (ii) further sweeping of the electrode potential to negative direction, the interfacial H_2O is largely replaced by H_{ad} that further reduces the scattering and increases the conductance.

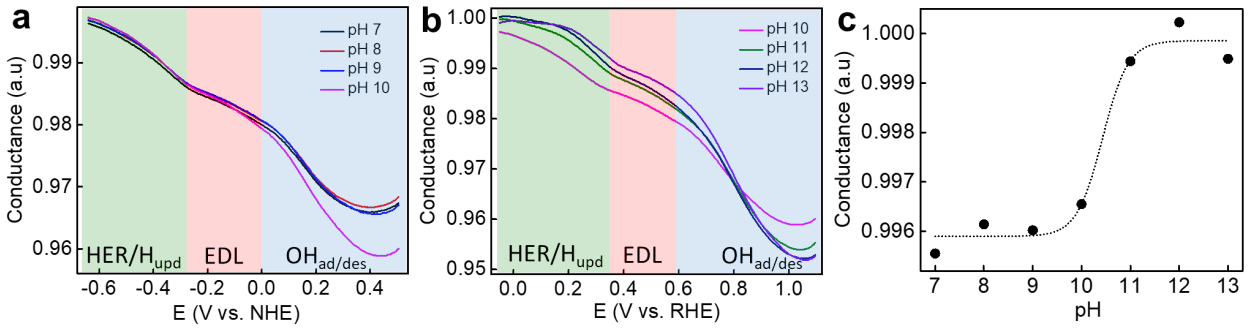

Figure 4.9: Electrical transport spectroscopy (ETS) measurements. (a) ETS spectra in pH 7-10 versus NHE scale, (b) pH 10-13 versus RHE scale in 0.1 M electrolyte (ionic strength and pH was maintained by KOH and $KClO_4$) and (c) Plot of conductance versus electrolyte pH at -0.59 V versus NHE (from pH 7-10) and 0 V versus RHE (from pH 10-13) (the dotted line is guide to eye).

The ETS studies in electrolytes with different pH reveal that the conductance is nearly constant in the electrical double layer regime (EDL) and HER/H_{upd} potential regime in the electrolyte of pH 7-9 indicating little change in surface speciation on Pt surface within this pH range (Fig. 4.9a). The shape of the ETS signal at and above pH 10 display notably different characteristics (Fig. 4.9b). In particular, the conductance showed an increase above pH 10 in the EDL and HER/H_{upd} potential regime (Fig. 4.9b). A plot of the conductance in the HER regime versus pH shows a nearly constant conductance from pH 7-9 and a steep rise of the conductance with increasing pH above 10 (Fig. 4.9c). Considering the surface adsorbates in the EDL region is dominated by H_2O_{ad}[30], such an increase of the conductance suggests a change in H_2O_{ad} configuration, likely from a more scattering (lower conductance) O-down configuration at lower pH to a less scattering (higher conductance) H-down configuration at higher pH. Such change of water orientation is also in line with previous experimental reports[31]. Interestingly, this switch in the ETS conductance signal at around pH 10 is largely consistent with the evolution of the pH-dependent HER Tafel slopes. The transition point in ETS results indicate that there is an abrupt change in surface speciation at pH 10, which leads to a switch in HER kinetics (Tafel slope) from a Volmer-step dictated kinetics (with the Tafel slope of ~110 mV/dec) below pH 10 to a Heyrovsky-step-dictated kinetics (Tafel slope ~ 53 mV/dec) above pH 10.

4.4.3. Theoretical insight into the role of pH on surface adsorbates

We performed theoretical calculations to further understand the change in surface speciation and explore the molecular level origin of the switch in HER kinetics. To probe the nature of the interfacial structural transition that underlies the switching behavior, we used the fixed-potential density functional theory (FP-DFT) technique to locate the most stable adsorption configuration of water on Pt(111) at 0 V_{RHE} in the pH range of 7 to 14 (Fig. 4.10)[32].

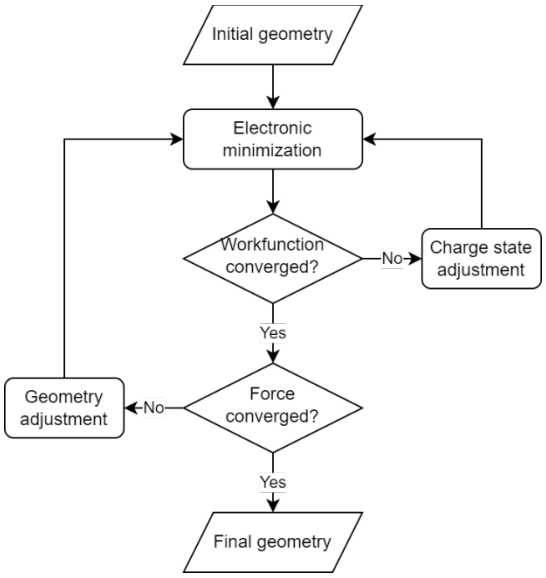

Figure 4.10: Algorithmic flowchart of the fixed-potential geometry optimization.

Our calculations show that the adsorbed water adopts an O-down configuration below pH=11 but switches to the H-down configuration above pH=11 (Fig. 4.11a). As a result of the configurational change, the Pt—O distance increases from ca. 2.4 Å to 3.3 Å, and the angle between the H_2O orientation (defined by the vector from O to the midpoint of H's) and the Pt surface normal increases from ca. 60° to 170° (Fig. 4.11b).

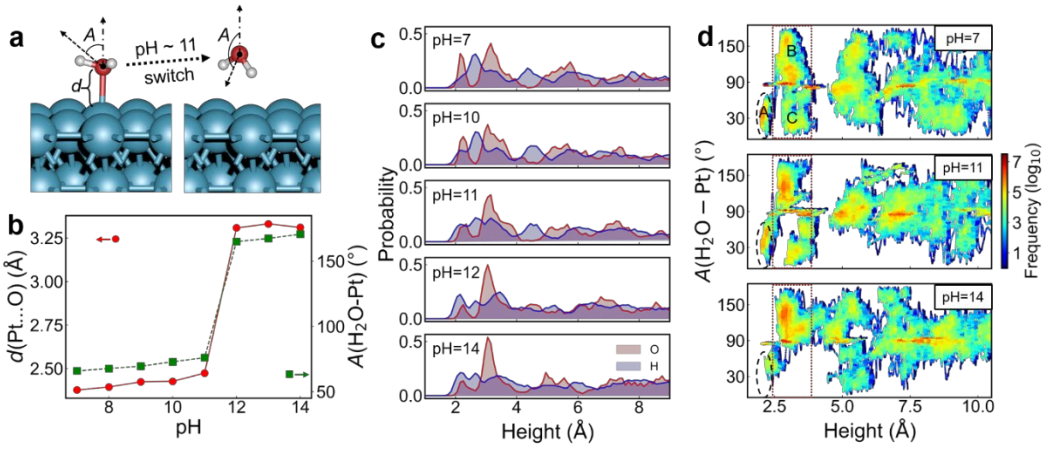

Figure 4.11: Static and dynamic fixed-potential DFT calculations of interfacial structure of Pt(111)/water. (a) Structural models of low-pH and high-pH water configurations on Pt(111), with key geometric parameters marked. (b) The Pt—O distance and the water orientation angle in pH range of 7 to 14. (c) Spatial probability distribution of O and H in water with respect to relative height to Pt surface from fixed-potential ab initio MD simulations at selected pH levels. (d) Statistics of water orientation angle with respect

to relative height to Pt surface at selected pH levels. The regions corresponding to adsorbed water (region A) and the contact water layer (region B and C for H-down and O-down waters) are marked by black dashed circle and red dotted box, respectively.

To better describe the realistic solvation and dynamics at room temperature[33], we further performed ab initio molecular dynamics (AIMD) with an explicit water slab of ca. 10 Å thickness and fixed-potential (FP) treatment (Fig. 4.12 and 4.13), and compared the spatial distribution of O and H atoms (relative to the Pt surface) at selected pH (Fig. 4.11c). As pH increase from 7 to 10, the first O peak at ca. 2.2 Å stays sharp and high, suggesting a large population of directly O-adsorbed water. The H peak at 2.6 Å is significantly higher than the one at 2.1 Å, suggesting the O-down orientation in the contact layer to be dominant. As the pH increases from 10 to 11, the intensity of the first O peak is significantly reduced, suggesting a weakening of the water adsorption via Pt—O. Moreover, the intensity of the H peak at ca. 2.1 Å (corresponding to H-down water) builds up to a comparable level to that of the O-down at pH 11 and becomes dominant beyond pH=12, suggesting a flip of the majority of water molecules in the contact layer. Such a flip is better visualized by the distribution map of water orientation angles (Fig. 4.11d): the adsorbed O-down water (marked by region A) is depleted as the pH increases, and the majority of the interfacial waters shifts from a O-down orientation (Region B) to a H-down orientation (Region C). The flipping from O-down confuguration to H-down configuration upon increasing pH is consistent with a swtich from low conductance state at lower pH to a higher conductance state at higher pH observed in the ETS studies, in which the O-down configuration shows stronger electron scattering and thus lower conductance than the H-down configuration.

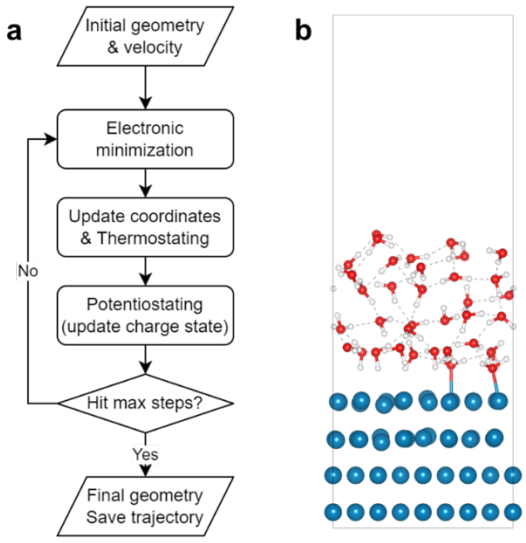

Figure 4.12: Algorithmic flowchart of the fixed-potential (FP) simulation (a) ab initio molecular dynamics (AIMD) simulation and (b) A side view of the simulation box used for FP-AIMD.

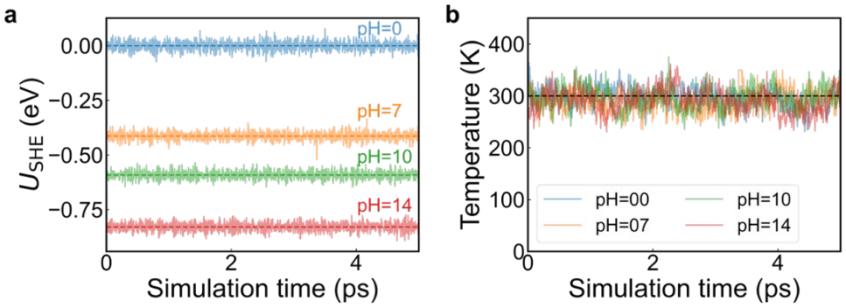

Figure 4.13: Validation of the proper potentiostating and thermosetting of the FP-AIMD scheme. The evolution of (a) the work function and (b) the temperature of the systems during 5-ps simulation at different pH levels.

The sharp crossover behavior at ~ pH 11 (Fig. 4.11) closely resembles the experimental pH dependence of HER Tafel slope, exchange density (Fig. 4.8b), which inspires us to quantify the influence of water configurational change on the HER activity. To this end, we performed Crystal Orbital Hamilton Population (COHP) analysis on selected atomic pairs in the pH range of 7 to 14. The obtained COHP is integrated up to Fermi level to yield negative integrated COHP ($-\mathrm{ICOHP}_{E_F}$), which acts at a descriptor of the strength of covalent or noncovalent interactions (Fig. 4.14a). It was observed that the Pt—O gradually weakens as the pH increases from 7 to 11, and sharply reduces to 0.02 eV at pH=11 and stays nearly constant thereafter. The Pt—H, however, is

strengthened from 0 to 0.08 eV after the orientational change from O-down to H-down, suggesting a stronger interaction between H in water and the Pt surface at higher pH.

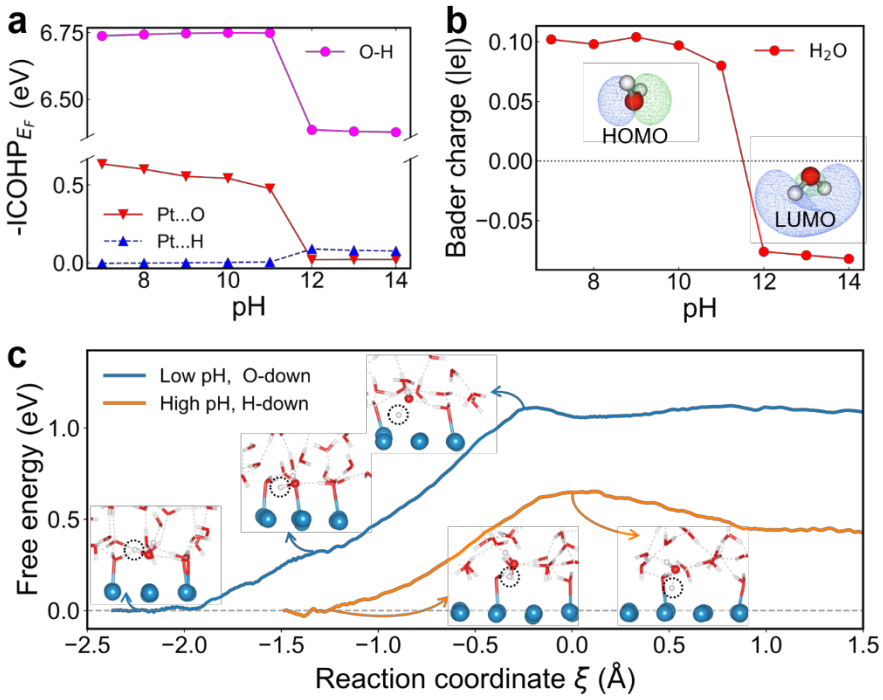

Figure 4.14: Influence of interfacial water orientation on water dissociation reactivity. (a) The bond strength descriptor, -ICOHP (negative integrated Crystal Orbital Hamilton Population) up to Fermi level, for Pt—O, Pt—H, and O-H in pH range of 7 to 14. (b) Net Bader charge on H_2O at the Pt surface in the pH range of 7 to 14, with HOMO and LUMO of water shown as insets. (c) The free energy profile of water dissociation for H-down water at high pH and O-down water at low pH. The transferred H is marked by dotted black circles. Notable configurations along the reaction coordinate are shown as insets.

Moreover, the O-H bond in interfacial water is significantly weakened by ca. 0.50 eV in terms of $-\text{ICOHP}_{E_F}$upon the orientational change (Fig. 4.14a). The change in effective pK_a of H-down water is estimated, by the fitted correlation between experimental pK_a and calculated $-\text{ICOHP}_{E_F}$ (Fig. 4.15), to be 8 units lower than the neutral O-down case, which agrees reasonably well with acidic-like kinetics suggested in previous experimental reports[34, 35]. In addition, the H-down water could act as a relay for protons in the outer water layers to cascade to the Pt surface via a hydronium-like intermediate, which is also in line with recent reports of higher local

concentration of hydronium species near the Pt surface in high pH conditions.[24] Therefore, more facile Volmer kinetics is expected beyond pH=11 due to the orientational change, which results in the switch of Tafel slope to a smaller value (Fig. 4.8b).

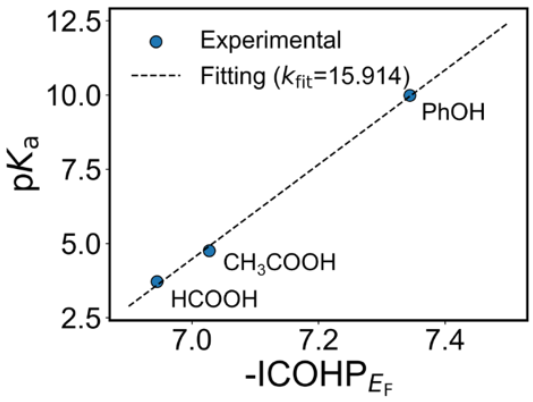

Figure 4.15: Correlating pK_a with calculated -ICOHP up to Fermi level on an experimental data set of organic acids. The R-square of the fitting is 0.998.

The molecular origin of the O—H weakening is further analyzed by Bader charge analysis (Fig. 4.14b) and molecular fragment analysis (Fig. 4.16). The net charge of water is ca. +0.10 |e| in the O-down and −0.06 |e| in the H-down configurations. The partial charging of interfacial water at higher pH can be attributed to the charge redistribution caused by shift of the work function of the surface. Due to the non-bonding nature of the HOMO (O 2*p* lone pair), partial removal of electron from it has little influence on the O—H bond strength. On the other hand, the LUMO in water has O—H σ^* characteristics (Fig. 4.14b inset), and the filling of this orbital would directly lead to a weakening of O—H bond, as is evidenced by a decrease in Mayer bond order from 0.9 to 0.24 per electron. The diffuse nature of the H-side lobe of the HOMO also promotes the interaction between H in water and the Pt surface.

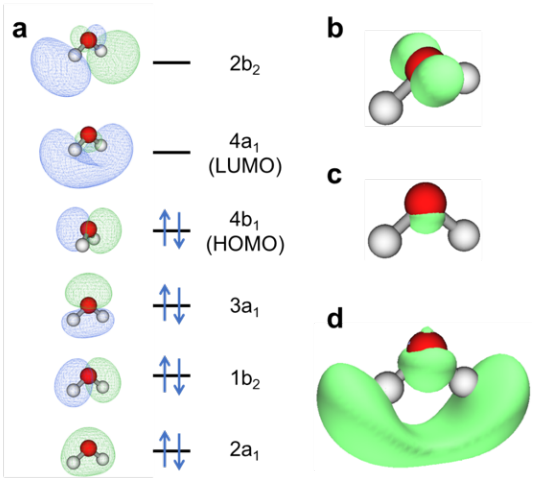

Figure 4.16: Molecular fragment analysis of charged H_2O. (a) Molecular orbital diagram of H_2O. The isosurface of (b) positive charge on $[H_2O]^+$ at isovalue of 0.02, (c) negative charge on $[H_2O]^+$ at isovalue of 0.02 and (d) at 0.005.

To quantify the influence of interfacial water configuration on the kinetics of water dissociation, we performed free energy calculations by slow-growth constrained MD sampling and thermodynamic integration within the FP-AIMD scheme. Our calculations show that the O-down water at low pH needs to rotate to a flat configuration before it can break the O—H bond and transfer the H to the Pt surface, with a rather high free energy barrier of 1.10 eV (Fig. 4.14c). In contrast, the H-down water at high pH do not need to go through this extra step and can directly dissociate with a much lower free energy barrier of 0.55 eV. In other words, the interfacial polarization and reorientation of interfacial water molecules to the H-down configuration at high pH not only electronically weakens the O—H in water, but also modifies the water dissociation reaction pathway by skipping an intermediate flat configuration, thus greatly reducing the kinetic barrier and leading to considerably improved HER activity.

Additionally, we note that near-surface hydroxide may also play a role in modifying the reaction kinetics, although for technical reasons it is infeasible to explicitly include solvated hydroxide in the FP-AIMD. To explore this effect, we can derive the difference in thermodynamics

of hydroxide binding on the surface from the trajectory averages with and without *OH, assuming the initial state of hydroxide (solvated in the bulk electrolyte) to be pH-independent, so that we can cancel out the energy of the solvated state. In this case, our calculations reveal that the hydroxide binding with Pt at higher pH (where the majority of interfacial waters are H-down) is stronger than that at lower pH (where the majority of interfacial water are O-down) by 0.25 eV. This indicates the role of interfacial water orientation in stabilizing more surface hydroxide (via water deprotonation or other means) at higher pH values. Such surface hydroxide could also function as electronically favored proton acceptors and geometrically favored proton donors for interfacial H-down water to promote water dissociation[29].

4.5. Conclusions

In summary, we have performed surface-sensitive electrical transport spectroscopy measurements as well as static and dynamic fixed-potential DFT calculations to understand the molecular level origin of the pH-dependent HER activity on Pt surface in alkaline media. The intriguing switching behavior in the pH dependence of interfacial conductance and Tafel slope at ca. pH=10 suggest a reorganization of interfacial water molecule structure and a change in HER mechanism. Static and dynamic calculations reveal a sharp orientation transition of interfacial water from the O-down to H-down configuration, which, as further shown by chemical bonding analysis, leads to weakened O—H bond and enhanced HER kinetics. Our theoretical results show that the hydroxide binding with Pt at high pH (where the majority of interfacial water are H-down) is stronger than the case at low pH (where the majority of interfacial water are O-down) by 0.25 eV. Such surface hydroxide could function as electronically favored proton acceptors and geometrically favored proton donors for interfacial H-down water to promote water dissociation. The excellent correlation among experiment and theory provides, for the first time, a robust

interpretation of the pH-dependent HER kinetics on Pt surface in alkaline media. These studies provide a pathway toward a more complete understanding of pH effects on the electrode/water interfacial structure and their critical role in the relevant electrochemical reactions and renewable energy conversion.

4.6. References

(1) Sheng, W.; Zhuang, Z.; Gao, M.; Zheng, J.; Chen, J. G.; Yan, Y. Correlating hydrogen oxidation and evolution activity on platinum at different pH with measured hydrogen binding energy. *Nature communications* **2015**, *6* (1), 1-6.

(2) Nørskov, J. K.; Bligaard, T.; Logadottir, A.; Kitchin, J.; Chen, J. G.; Pandelov, S.; Stimming, U. Trends in the exchange current for hydrogen evolution. *Journal of The Electrochemical Society* **2005**, *152* (3), J23.

(3) Ledezma-Yanez, I.; Wallace, W. D. Z.; Sebastián-Pascual, P.; Climent, V.; Feliu, J. M.; Koper, M. T. M. Interfacial water reorganization as a pH-dependent descriptor of the hydrogen evolution rate on platinum electrodes. *Nature Energy* **2017**, *2* (4), 17031. DOI: 10.1038/nenergy.2017.31.

(4) Bockris, J. M.; Potter, E. The mechanism of the cathodic hydrogen evolution reaction. *Journal of The Electrochemical Society* **1952**, *99* (4), 169.

(5) Schouten, K.; Van Der Niet, M.; Koper, M. Impedance spectroscopy of H and OH adsorption on stepped single-crystal platinum electrodes in alkaline and acidic media. *Physical Chemistry Chemical Physics* **2010**, *12* (46), 15217-15224.

(6) Strmcnik, D.; Uchimura, M.; Wang, C.; Subbaraman, R.; Danilovic, N.; Van Der Vliet, D.; Paulikas, A. P.; Stamenkovic, V. R.; Markovic, N. M. Improving the hydrogen oxidation reaction rate by promotion of hydroxyl adsorption. *Nature chemistry* **2013**, *5* (4), 300-306.

(7) Zhong, G.; Cheng, T.; Shah, A. H.; Wan, C.; Huang, Z.; Wang, S.; Leng, T.; Huang, Y.; Goddard, W. A.; Duan, X. Determining the hydronium pKα at platinum surfaces and the effect on pH-dependent hydrogen evolution reaction kinetics. *Proceedings of the National Academy of Sciences* **2022**, *119* (39), e2208187119. DOI: 10.1073/pnas.2208187119 (acccessed 2022/09/21).

(8) Govindarajan, N.; Xu, A.; Chan, K. How pH affects electrochemical processes. *Science* **2022**, *375* (6579), 379-380. DOI: doi:10.1126/science.abj2421.

(9) Greeley, J.; Jaramillo, T. F.; Bonde, J.; Chorkendorff, I.; Nørskov, J. K. Computational high-throughput screening of electrocatalytic materials for hydrogen evolution. *Nature materials* **2006**, *5* (11), 909-913.

(10) Laursen, A. B.; Varela, A. S.; Dionigi, F.; Fanchiu, H.; Miller, C.; Trinhammer, O. L.; Rossmeisl, J.; Dahl, S. Electrochemical hydrogen evolution: Sabatier's principle and the volcano plot. *Journal of Chemical Education* **2012**, *89* (12), 1595-1599.

(11) Skúlason, E.; Tripkovic, V.; Björketun, M. E.; Gudmundsdóttir, S.; Karlberg, G.; Rossmeisl, J.; Bligaard, T.; Jónsson, H.; Nørskov, J. K. Modeling the electrochemical hydrogen oxidation and evolution reactions on the basis of density functional theory calculations. *The Journal of Physical Chemistry C* **2010**, *114* (42), 18182-18197.

(12) Zhu, S.; Qin, X.; Yao, Y.; Shao, M. pH-Dependent Hydrogen and Water Binding Energies on Platinum Surfaces as Directly Probed through Surface-Enhanced Infrared Absorption Spectroscopy. *Journal of the American Chemical Society* **2020**, *142* (19), 8748-8754. DOI: 10.1021/jacs.0c01104.

(13) Sheng, W.; Gasteiger, H. A.; Shao-Horn, Y. Hydrogen oxidation and evolution reaction kinetics on platinum: acid vs alkaline electrolytes. *Journal of The Electrochemical Society* **2010**, *157* (11), B1529.

(14) Subbaraman, R.; Tripkovic, D.; Chang, K.-C.; Strmcnik, D.; Paulikas, A. P.; Hirunsit, P.; Chan, M.; Greeley, J.; Stamenkovic, V.; Markovic, N. M. Trends in activity for the water electrolyser reactions on 3d M (Ni, Co, Fe, Mn) hydr (oxy) oxide catalysts. *Nature materials* **2012**, *11* (6), 550-557.

(15) Durst, J.; Siebel, A.; Simon, C.; Hasché, F.; Herranz, J.; Gasteiger, H. A. New insights into the electrochemical hydrogen oxidation and evolution reaction mechanism. *Energy & Environmental Science* **2014**, *7* (7), 2255-2260, 10.1039/C4EE00440J. DOI: 10.1039/C4EE00440J.

(16) van der Niet, M. J. T. C.; Garcia-Araez, N.; Hernández, J.; Feliu, J. M.; Koper, M. T. M. Water dissociation on well-defined platinum surfaces: The electrochemical perspective. *Catalysis Today* **2013**, *202*, 105-113. DOI: https://doi.org/10.1016/j.cattod.2012.04.059.

(17) Goyal, A.; Koper, M. T. M. The Interrelated Effect of Cations and Electrolyte pH on the Hydrogen Evolution Reaction on Gold Electrodes in Alkaline Media. *Angewandte Chemie International Edition* **2021**, *60* (24), 13452-13462. DOI: https://doi.org/10.1002/anie.202102803.

(18) Shen, L.-f.; Lu, B.-a.; Li, Y.-y.; Liu, J.; Huang-fu, Z.-c.; Peng, H.; Ye, J.-y.; Qu, X.-m.; Zhang, J.-m.; Li, G.; et al. Interfacial Structure of Water as a New Descriptor of the Hydrogen Evolution Reaction. *Angewandte Chemie International Edition* **2020**, *59* (50), 22397-22402. DOI: https://doi.org/10.1002/anie.202007567.

(19) Cheng, T.; Wang, L.; Merinov, B. V.; Goddard, W. A., III. Explanation of Dramatic pH-Dependence of Hydrogen Binding on Noble Metal Electrode: Greatly Weakened Water Adsorption at High pH. *Journal of the American Chemical Society* **2018**, *140* (25), 7787-7790. DOI: 10.1021/jacs.8b04006.

(20) Chen, M.; Zheng, L.; Santra, B.; Ko, H.-Y.; DiStasio Jr, R. A.; Klein, M. L.; Car, R.; Wu, X. Hydroxide diffuses slower than hydronium in water because its solvated structure inhibits correlated proton transfer. *Nature Chemistry* **2018**, *10* (4), 413-419. DOI: 10.1038/s41557-018-0010-2.

(21) Koper, M. A basic solution. *Nature chemistry* **2013**, *5* (4), 255-256.

(22) Li, P.; Jiang, Y.; Hu, Y.; Men, Y.; Liu, Y.; Cai, W.; Chen, S. Hydrogen bond network connectivity in the electric double layer dominates the kinetic pH effect in hydrogen electrocatalysis on Pt. *Nature Catalysis* **2022**. DOI: 10.1038/s41929-022-00846-8.

(23) Lamoureux, P. S.; Singh, A. R.; Chan, K. pH Effects on Hydrogen Evolution and Oxidation over Pt(111): Insights from First-Principles. *ACS Catalysis* **2019**, *9* (7), 6194-6201. DOI: 10.1021/acscatal.9b00268.

(24) Wang, X.; Xu, C.; Jaroniec, M.; Zheng, Y.; Qiao, S.-Z. Anomalous hydrogen evolution behavior in high-pH environment induced by locally generated hydronium ions. *Nature Communications* **2019**, *10* (1), 4876. DOI: 10.1038/s41467-019-12773-7.

(25) Jung, O.; Jackson, M. N.; Bisbey, R. P.; Kogan, N. E.; Surendranath, Y. Innocent buffers reveal the intrinsic pH- and coverage-dependent kinetics of the hydrogen evolution reaction on noble metals. *Joule* **2022**, *6* (2), 476-493. DOI: https://doi.org/10.1016/j.joule.2022.01.007.

(26) Sun, K.; Wu, X.; Zhuang, Z.; Liu, L.; Fang, J.; Zeng, L.; Ma, J.; Liu, S.; Li, J.; Dai, R.; et al. Interfacial water engineering boosts neutral water reduction. *Nature Communications* **2022**, *13* (1), 6260. DOI: 10.1038/s41467-022-33984-5.

(27) Ding, M.; He, Q.; Wang, G.; Cheng, H.-C.; Huang, Y.; Duan, X. An on-chip electrical transport spectroscopy approach for in situ monitoring electrochemical interfaces. *Nature Communications* **2015**, *6* (1), 7867. DOI: 10.1038/ncomms8867.

(28) Ding, M.; Zhong, G.; Zhao, Z.; Huang, Z.; Li, M.; Shiu, H.-Y.; Liu, Y.; Shakir, I.; Huang, Y.; Duan, X. On-chip in situ monitoring of competitive interfacial anionic chemisorption as a descriptor for oxygen reduction kinetics. *ACS central science* **2018**, *4* (5), 590-599.

(29) Shah, A. H.; Zhang, Z.; Huang, Z.; Wang, S.; Zhong, G.; Wan, C.; Alexandrova, A. N.; Huang, Y.; Duan, X. The role of alkali metal cations and platinum-surface hydroxyl in the alkaline hydrogen evolution reaction. *Nature Catalysis* **2022**. DOI: 10.1038/s41929-022-00851-x.

(30) Giles, S. A.; Wilson, J. C.; Nash, J.; Xu, B.; Vlachos, D. G.; Yan, Y. Recent advances in understanding the pH dependence of the hydrogen oxidation and evolution reactions. *Journal of Catalysis* **2018**, *367*, 328-331. DOI: https://doi.org/10.1016/j.jcat.2018.09.030.

(31) Li, C.-Y.; Le, J.-B.; Wang, Y.-H.; Chen, S.; Yang, Z.-L.; Li, J.-F.; Cheng, J.; Tian, Z.-Q. In situ probing electrified interfacial water structures at atomically flat surfaces. *Nature materials* **2019**, *18* (7), 697-701. DOI: 10.1038/s41563-019-0356-x.

(32) Duan, Z.; Henkelman, G. Atomic-Scale Mechanisms of Electrochemical Pt Dissolution. *ACS Catalysis* **2021**, *11* (23), 14439-14447.

(33) Chen, J.-W.; Zhang, Z.; Yan, H.-M.; Xia, G.-J.; Cao, H.; Wang, Y.-G. Pseudo-adsorption and long-range redox coupling during oxygen reduction reaction on single atom electrocatalyst. *Nature Communications* **2022**, *13* (1), 1734. DOI: 10.1038/s41467-022-29357-7.

(34) Martínez-Hincapié, R.; Sebastián-Pascual, P.; Climent, V.; Feliu, J. M. Exploring the interfacial neutral pH region of Pt(111) electrodes. *Electrochemistry Communications* **2015**, *58*, 62-64. DOI: https://doi.org/10.1016/j.elecom.2015.06.005.

(35) Rizo, R.; Sitta, E.; Herrero, E.; Climent, V.; Feliu, J. M. Towards the understanding of the interfacial pH scale at Pt(111) electrodes. *Electrochimica Acta* **2015**, *162*, 138-145. DOI: https://doi.org/10.1016/j.electacta.2015.01.069.

(36) Yoo, H.-W.; Cho, S.-Y.; Jeon, H.-J.; Jung, H.-T. Well-Defined and High Resolution Pt Nanowire Arrays for a High Performance Hydrogen Sensor by a Surface Scattering Phenomenon. *Analytical Chemistry* **2015**, *87* (3), 1480-1484. DOI: 10.1021/ac504367w.

(37) Jorgensen, W. L.; Chandrasekhar, J.; Madura, J. D.; Impey, R. W.; Klein, M. L. Comparison of simple potential functions for simulating liquid water. *The Journal of chemical physics* **1983**, *79* (2), 926-935.

(38) Adamo, C.; Barone, V. Toward reliable density functional methods without adjustable parameters: The PBE0 model. *The Journal of chemical physics* **1999**, *110* (13), 6158-6170.

(39) Kresse, G.; Joubert, D. From ultrasoft pseudopotentials to the projector augmented-wave method. *Physical review b* **1999**, *59* (3), 1758.

(40) Kresse, G.; Furthmüller, J. Efficiency of ab-initio total energy calculations for metals and semiconductors using a plane-wave basis set. *Computational materials science* **1996**, *6* (1), 15-50.

(41) Kresse, G.; Furthmüller, J. Efficient iterative schemes for ab initio total-energy calculations using a plane-wave basis set. *Physical review B* **1996**, *54* (16), 11169.

(42) Kresse, G.; Hafner, J. Ab initio molecular dynamics for liquid metals. *Physical review B* **1993**, *47* (1), 558.

(43) Kresse, G.; Hafner, J. Ab initio molecular-dynamics simulation of the liquid-metal–amorphous-semiconductor transition in germanium. *Physical Review B* **1994**, *49* (20), 14251.

(44) Grimme, S.; Antony, J.; Ehrlich, S.; Krieg, H. A consistent and accurate ab initio parametrization of density functional dispersion correction (DFT-D) for the 94 elements H-Pu. *The Journal of chemical physics* **2010**, *132* (15), 154104.

(45) Mathew, K.; Kolluru, V. C.; Mula, S.; Steinmann, S. N.; Hennig, R. G. Implicit self-consistent electrolyte model in plane-wave density-functional theory. *The Journal of Chemical Physics* **2019**, *151* (23), 234101.

(46) Yu, M.; Trinkle, D. R. Accurate and efficient algorithm for Bader charge integration. *The Journal of chemical physics* **2011**, *134* (6), 064111.

(47) Nelson, R.; Ertural, C.; George, J.; Deringer, V. L.; Hautier, G.; Dronskowski, R. LOBSTER: Local orbital projections, atomic charges, and chemical-bonding analysis from projector-augmented-wave-based density-functional theory. *Journal of Computational Chemistry* **2020**, *41* (21), 1931-1940.

(48) Chai, J.-D.; Head-Gordon, M. Long-range corrected hybrid density functionals with damped atom–atom dispersion corrections. *Physical Chemistry Chemical Physics* **2008**, *10* (44), 6615-6620.

(49) Schäfer, A.; Huber, C.; Ahlrichs, R. Fully optimized contracted Gaussian basis sets of triple zeta valence quality for atoms Li to Kr. *The Journal of chemical physics* **1994**, *100* (8), 5829-5835.

(50) Frisch, M.; Trucks, G.; Schlegel, H.; Scuseria, G. et mult. al., Gaussian 16 Revision C. 01, Gaussian. *Inc., Wallingford CT* **2016**.

(51) Lu, T.; Chen, F. Multiwfn: A multifunctional wavefunction analyzer. *Journal of computational chemistry* **2012**, *33* (5), 580-592.

(52) Steinmann, S. N.; Michel, C.; Schwiedernoch, R.; Sautet, P. Impacts of electrode potentials and solvents on the electroreduction of CO 2: a comparison of theoretical approaches. *Physical Chemistry Chemical Physics* **2015**, *17* (21), 13949-13963.

(53) Korpelin, V.; Kiljunen, T.; Melander, M. M.; Caro, M. A.; Kristoffersen, H. H.; Mammen, N.; Apaja, V.; Honkala, K. Addressing dynamics at catalytic heterogeneous interfaces with DFT-

MD: Anomalous temperature distributions from commonly used thermostats. *The journal of physical chemistry letters* **2022**, *13* (11), 2644-2652.

(54) Bonnet, N.; Morishita, T.; Sugino, O.; Otani, M. First-Principles Molecular Dynamics at a Constant Electrode Potential. *Physical Review Letters* **2012**, *109* (26), 266101. DOI: 10.1103/PhysRevLett.109.266101.

(55) Humphrey, W.; Dalke, A.; Schulten, K. VMD: visual molecular dynamics. *Journal of molecular graphics* **1996**, *14* (1), 33-38.

(56) Ryckaert, J.-P.; Ciccotti, G.; Berendsen, H. J. C. Numerical integration of the cartesian equations of motion of a system with constraints: molecular dynamics of n-alkanes. *Journal of Computational Physics* **1977**, *23* (3), 327-341. DOI: https://doi.org/10.1016/0021-9991(77)90098-5.

(57) Fleurat-Lessard, P.; Ziegler, T. Tracing the minimum-energy path on the free-energy surface. *The Journal of Chemical Physics* **2005**, *123* (8). DOI: 10.1063/1.1948367 (acccessed 8/23/2023).

(58) Sundararaman, R.; Schwarz, K. Evaluating continuum solvation models for the electrode-electrolyte interface: Challenges and strategies for improvement. *The Journal of Chemical Physics* **2017**, *146* (8). DOI: 10.1063/1.4976971 (acccessed 8/23/2023).

(59) Gauthier, J. A.; Ringe, S.; Dickens, C. F.; Garza, A. J.; Bell, A. T.; Head-Gordon, M.; Nørskov, J. K.; Chan, K. Challenges in Modeling Electrochemical Reaction Energetics with Polarizable Continuum Models. *ACS Catalysis* **2019**, *9* (2), 920-931. DOI: 10.1021/acscatal.8b02793.

(60) Le, D. An Explicit-Implicit Hybrid Solvent Model for Grand Canonical Simulations of the Electrochemical Environment. **2023**. DOI: https://doi.org/10.26434/chemrxiv-2023-z2n4n.

(61) Zhang, Z.; Wei, Z.; Sautet, P.; Alexandrova, A. N. Hydrogen-Induced Restructuring of a Cu(100) Electrode in Electroreduction Conditions. *Journal of the American Chemical Society* **2022**, *144* (42), 19284-19293. DOI: 10.1021/jacs.2c06188.

(62) Hanselman, S.; Calle-Vallejo, F.; Koper, M. Computational description of surface hydride phases on Pt (111) electrodes. *The Journal of Chemical Physics* **2023**, *158* (1).

(63) Cheng, D.; Wei, Z.; Zhang, Z.; Broekmann, P.; Alexandrova, A. N.; Sautet, P. Restructuring and Activation of Cu(111) under Electrocatalytic Reduction Conditions. *Angewandte Chemie International Edition* **2023**, *62* (20), e202218575. DOI: https://doi.org/10.1002/anie.202218575.

(64) Cheng, T.; Xiao, H.; Goddard, W. A. Full atomistic reaction mechanism with kinetics for CO reduction on Cu(100) from ab initio molecular dynamics free-energy calculations at 298 K. *Proceedings of the National Academy of Sciences* **2017**, *114* (8), 1795-1800. DOI: doi:10.1073/pnas.1612106114.

(65) Zhao, X.; Levell, Z. H.; Yu, S.; Liu, Y. Atomistic Understanding of Two-dimensional Electrocatalysts from First Principles. *Chemical Reviews* **2022**, *122* (12), 10675-10709. DOI: 10.1021/acs.chemrev.1c00981.

(66) Qian, S.-J.; Cao, H.; Chen, J.-W.; Chen, J.-C.; Wang, Y.-G.; Li, J. Critical Role of Explicit Inclusion of Solvent and Electrode Potential in the Electrochemical Description of Nitrogen Reduction. *ACS Catalysis* **2022**, *12* (18), 11530-11540. DOI: 10.1021/acscatal.2c03186.

CHAPTER 5

Conclusion

In conclusion, a number of mechanistic understandings have been suggested to interpret the pH-dependent or electrolyte-dependent HER kinetics. The progress to date is largely guided by oversimplified approaches with a single macroscopic descriptor. On the other hand, the exact nature of the electrode–electrolyte environment and molecular reaction pathway in different electrolytes could be substantially different, depending on the surface water protonation status, water orientation, as well as other unavoidable cations, anions, and buffer molecules that may fundamentally alter the local chemical environment at the electrode–electrolyte interface. In particular, the HER in acid, neutral, and alkaline media follows different reaction pathways with different rate-determining steps. Thus, a single descriptor can hardly give a fully satisfactory interpretation of the evolution of the HER kinetics in different pH environments. In alkaline media (pH > 10), the Heyrovsky step becomes the rate-determining step, and hence the HER activity increases at higher pH since a higher OH– concentration may lead to more OH_{ad} on Pt surface, which acts as proton donors and acceptors to near surface water and promotes water dissociation. Furthermore, it is also noted that even within the alkaline range, the HER can have multiple descriptors. Thus, the attempt to use a single macroscopic descriptor to explain the electrocatalytic reaction in these very different situations can be misleading. In general, the explanation of different HER activity on the Pt surface in acid, neutral, and alkaline media is still a topic of considerable debate. To resolve the apparent inconsistencies among different interpretations, we developed a molecular level picture of the exact reaction pathways so that we can properly evaluate the relevance and importance of different descriptors and understand the fundamental origin of

different HER kinetics in different electrolytes. For fundamental investigations, it is beneficial to keep the electrode–electrolyte interface as simple as possible. For example, at higher pH beyond 7, the neutral water molecules remain the proton source throughout the pH range 7–14, while the HER activities show notable enhancement with increasing pH. We have combined a unique surface-adsorbate specific ETS approach with EIS experiments and DFT calculations to directly probe the on-surface and near-surface chemical environment, deciphering the elusive role of alkali metal cations (AM^+) on Pt-surface chemistry and the alkaline HER. Our integrated studies suggest that the cation is not directly bonded to the Pt surface or OH_{ad} but is separated by a water molecule in the first hydration shell of the cation, which is distinct from previous studies. Moreover, smaller cations favor a higher OH_{ad} coverage on the Pt surface in the HER potential window, where the OH_{ad} in turn function as electronically favored proton acceptors or geometrically favored proton donors to promote water dissociation and Volmer-step kinetics on the Pt surface in alkaline media, leading to improved HER activity in the presence of smaller cations (Li^+). Our studies resolve the fundamental role of AM^+ in the HER kinetics, which has remained elusive in recent decades, and could offer valuable insights for the design of more efficient electrolysers for renewable energy conversion. In another project, by using an integrated study to probe both the on-surface (ETS) and near-surface (EIS) signals, we experimentally proved that Cs^+ specifically adsorbs on the Pt electrode surface to such an extent that they can lower the availability of free surface sites and hence decrease the HER activity, whereas Rb^+ quasi-specifically adsorbs on the Pt surface and accumulates in the electrical double layer to form a denser cation layer, likely facilitated by its unique dynamism near the surface, which hinders the water transport and suppresses the HER activity. To the best of our knowledge, this study provides, for the first time, experimental evidence confirming quasi-specific and specific adsorption of Rb^+ and Cs^+ on the Pt electrode surface, which

allows us to rationalize the trend in HER kinetics following $K^+ > Cs^+ > Rb^+$ as resulting from a dual mode of deactivation: blocking the active site (found in Cs^+) and blocking the transport through EDL (found in Rb^+). Our study provides a molecular-level understanding of the fundamental role of weakly hydrated AM^+ in HER kinetics that has remained elusive for decades and is expected to offer valuable insights for the design of more efficient alkaline electrolysers. Finally, we have performed surface-sensitive ETS measurements as well as static and dynamic fixed-potential DFT calculations to understand the molecular level origin of the pH-dependent HER activity on Pt surface in alkaline media. The intriguing switching behavior in the pH dependence of interfacial conductance and Tafel slope at ca. pH=10 suggest a reorganization of interfacial water molecule structure and a change in HER mechanism. Static and dynamic calculations reveal a sharp orientation transition of interfacial water from the O-down to H-down configuration, which, as further shown by chemical bonding analysis, leads to weakened O—H bond and enhanced HER kinetics. Our theoretical results show that the hydroxide binding with Pt at high pH (where the majority of interfacial water are H-down) is stronger than the case at low pH (where the majority of interfacial water are O-down) by 0.25 eV. Such surface hydroxide could function as electronically favored proton acceptors and geometrically favored proton donors for interfacial H-down water to promote water dissociation. The excellent correlation among experiment and theory provides, for the first time, a robust interpretation of the pH-dependent HER kinetics on Pt surface in alkaline media. These studies provide a pathway toward a more complete understanding of pH effects on the electrode/water interfacial structure and their critical role in the relevant electrochemical reactions and renewable energy conversion.